NUMERICAL ANALYSIS OF THE REACTING FLOW IN A SPHERICAL JET STIRRED REACTOR

Zur Erlangung des akademischen Grades einer
DOKTORIN DER INGENIEURWISSENSCHAFTEN (Dr.-Ing)

von der KIT-Fakultät für Maschinenbau des
Karlsruher Instituts für Technologie (KIT)
angenommene

DISSERTATION
von

M. SC. GHAZALEH ESMAEELZADE

Tag der mündlichen Prüfung:	17.09.2024
Hauptreferent:	Prof. Dr. rer. nat. habil. Ulrich Maas
Korreferent:	Prof. Dr. rer. nat. Ravi Xavier Fernandes

ABSTRACT

Modeling the reacting flow inside chemical reactors improves our understanding of complex chemical reactions, especially those involving large numbers of chemicals. Chemical processes typically take place under turbulent conditions in lab-scale chemical reactors. High turbulent Reynolds number flow improves mixing efficiency; however, the complexity of the system increases, especially when taking into account the chemistry. Experimental data from the Jet Stirred Reactor (JSR) setup provide valuable information on chemical species conversions, although the details of the turbulent flow field characteristics are overlooked due to the limited optical accessibility of the apparatus setup. The main goal of the present study is to perform a numerical study to fill the information gap on the underlying mixing processes and to develop a theoretical model to capture the inhomogeneity inside the spherical JSR.

The present study is divided into two parts. The first part focuses on the Computational Fluid Dynamic (CFD) analysis of a non-reacting mixture by means of unsteady three-dimensional large eddy simulations. More specifically, the evolution of a tracer gas decay within a standard design of a spherical JSR with four turbulent nozzles is investigated. In order to numerically predict the temporal evolution of the tracer concentration, the large scale turbulent motions are resolved by the governing equations and the small scales are modeled by the Large Eddy Simulation (LES)-Smagorinsky turbulence modeling. In this study, the mixing quality inside the reactor is first investigated by analyzing the characteristics of the flow field, such as studying the turbulent kinetic energy, the residence time distribution, and the standard deviation of the tracer. Later, the mixing performance of the JSR is studied considering different sizes of nozzle diameter and spherical vessel diameter under different operating thermodynamic parameters. The results show that the standard design of the JSR (vessel diameter of 40 mm and nozzle diameter of 1 mm) at high pressures could improve mixing. However, a perfectly mixed composition and a homogeneous distribution of the tracer mass fraction are not achieved for any of the simulated spherical JSRs.

The second part aims to develop a zero-dimensional mathematical model for analyzing the chemical kinetics of a reacting mixture within the JSRs. Indeed, based on the results obtained in the first part, it is necessary to capture the inhomogeneous conditions inside the non-ideal JSRs through the development of a theoretical multi-zone model. According to this model, the JSR volume is divided into a number of representative homogeneous zones, in which all scalar fields in each zone are considered uniform. However, thermodynamic variables (except pressure) and mixture composition may differ from zone to zone. In order to include the mass and heat exchange between the zones, a mixing model is developed as a function of the turbulent frequency taken from the CFD results. In this study, the effects of the nonuniform distribution of the initial mole fraction of the reactants, the total volume, the wall temperature, and the heat transfer coefficient are studied for the oxidation processes of dimethyl ether (DME). The results highlight the importance of the non-uniform distribution of the heat transfer coefficient across the representative zones in effectively capturing the non-ideal behavior of an imperfectly mixed JSR compared to other cases. In fact, the regions inside the reactor that are farther from the walls transfer less heat from the surrounding compared to the areas closer to the walls. Therefore, inhomogeneity inside the JSR can be presented by assuming different values of heat transfer coefficients over the zones.

The results of the first part (CFD simulations) indicate a non-uniform distribution of the tracer mass fraction, predicting the presence of dead spaces and short circulations within the spherical JSR. Although an attempt is made to capture the inhomogeneity inside the JSR by a theoretical model, as described in the second part (multi-zone model), it is still important to improve the design of the spherical JSRs with four inclined nozzles in order to obtain a homogeneous mixture. Thus, an alternative six-nozzle reactor is proposed in which two nozzles pointing directly towards the center of the vessel. The efficient mixing inside the six-nozzle JSR is compared with a common setup of the JSR by analyzing the flow field characteristics and the turbulent kinetic energy.

KURZFASSUNG

Die Modellierung der Reaktionsströmung in chemischen Reaktoren verbessert unser Verständnis komplexer chemischer Reaktionen, insbesondere solcher, an denen eine große Anzahl von Chemikalien beteiligt ist. Chemische Prozesse finden in der Regel unter turbulenten Bedingungen in chemischen Reaktoren im Labormaßstab statt. Eine Strömung mit hoher turbulenter Reynoldszahl verbessert die Mischeffizienz; allerdings nimmt die Komplexität des Systems zu, insbesondere wenn man die Chemie berücksichtigt. Experimentelle Daten aus dem JSR-Aufbau liefern wertvolle Informationen über die Umwandlung chemischer Spezies, obwohl die Details der Eigenschaften des turbulenten Strömungsfeldes aufgrund der begrenzten optischen Zugänglichkeit des Geräteaufbaus übersehen werden. Das Hauptziel der vorliegenden Studie ist die Durchführung einer numerischen Studie, um die Informationslücke über die zugrundeliegenden Mischungsprozesse zu schließen und ein theoretisches Modell zur Erfassung der Inhomogenität innerhalb des sphärischen JSR zu entwickeln.

Die vorliegende Studie ist in zwei Teile gegliedert. Der erste Teil konzentriert sich auf die CFD-Analyse eines nicht reagierenden Gemischs mit Hilfe von instationären dreidimensionalen LES. Genauer gesagt, wird die Entwicklung der Abnahme eines Tracergases innerhalb eines Standarddesigns eines sphärischen JSR mit vier turbulenten Düsen untersucht. Um die zeitliche Entwicklung der Tracerkonzentration numerisch vorhersagen zu können, werden die großskaligen turbulenten Bewegungen durch die herrschenden Gleichungen aufgelöst und die kleinen Skalen durch die Turbulenzmodellierung der LES modelliert. In dieser Studie wird zunächst die Durchmischungsqualität im Reaktor untersucht, indem die Eigenschaften des Strömungsfeldes analysiert werden, wie zum Beispiel die turbulente kinetische Energie, die Verteilung der Verweilzeit und die Standardabweichung des Tracers. Danach wird die Mischeffizienz des JSR unter Berücksichtigung verschiedener Größen von Düsendurchmesser und Kugelbehälterdurchmesser unter verschiedenen thermodynamischen Betriebsparametern untersucht. Die Ergebnisse zeigen, dass das Standarddesign des JSR (Gefäßdurchmesser von 40 mm und Düsendurchmesser von 1 mm) bei hohen Drücken die

Durchmischung verbessern könnte. Eine perfekt gemischte Zusammensetzung und eine homogene Verteilung des Tracer-Massenanteils werden jedoch bei keinem der simulierten sphärischen JSR erreicht.

Der zweite Teil zielt auf die Entwicklung eines nulldimensionalen mathematischen Modells zur Analyse der chemischen Kinetik eines reagierenden Gemischs innerhalb des JSR. Nach diesem Modell wird das Volumen des JSR in eine Reihe repräsentativer homogener Zonen unterteilt, in denen alle Skalarfelder in jeder Zone als einheitlich betrachtet werden. Die thermodynamischen Variablen (mit Ausnahme des Drucks) und die Zusammensetzung des Gemischs können sich jedoch von Zone zu Zone unterscheiden. Um den Massen- und Wärmetransport zwischen den Zonen zu berücksichtigen, wird ein Vermischungsmodell als Funktion der Turbulenzfrequenz entwickelt, die aus den CFD-Ergebnissen entnommen wird. Anschließend werden die Auswirkungen der ungleichmäßigen Verteilung des anfänglichen Molanteils der Reaktanten, des Gesamtvolumens, der Wandtemperatur und des Wärmeübergangs-koeffizienten für die Oxidationsprozesse von Dimethylether untersucht. Die Ergebnisse zeigen, wie wichtig die ungleichmäßige Verteilung des Wärmeübergangskoeffizienten über die repräsentativen Zonen ist, um das nichtideale Verhalten eines unvollkommen gemischten JSR im Vergleich zu anderen Fällen effektiv zu erfassen. Tatsächlich übertragen die weiter von den Wänden entfernten Bereiche im Inneren des Reaktors weniger Wärme aus der Umgebung als die näher an den Wänden liegenden Bereiche. Daher kann die Inhomogenität innerhalb des JSR durch die Annahme unterschiedlicher Werte der Wärmeübergangskoeffizienten in den Zonen dargestellt werden.

Die Ergebnisse des ersten Teils (CFD-Simulationen) deuten auf eine ungleichmäßige Verteilung des Tracer-Massenanteils hin, die das Vorhandensein von Toträumen und kurzen Zirkulationen innerhalb des sphärischen JSR vorhersagt. Obwohl versucht wird, die Inhomogenität im Inneren des JSR durch ein theoretisches Modell zu erfassen, wie es im zweiten Teil (Mehrzonenmodell) beschrieben wird, ist es immer noch wichtig, das Design des kugelförmigen JSR mit vier geneigten Düsen zu verbessern, um eine homogene Mischung zu erhalten.

ACKNOWLEDGMENTS

This research was carried out at the Department of Explosion Protection in Energy Technology at the Physikalisch-Technische Bundesanstalt (PTB) in Braunschweig, Germany. I would like to express my deepest gratitude to Dr. Detlev Markus, and Prof. Dr. Ravi Fernandes, and Prof. Uwe Klausmeyer, the fantastic heads of the department, for providing the funding for this project. Special thanks are due to my advisors Dr. Holger Grosshans and Dr. Kai Moshammer for their guidance and continuous support during my research.

I would also like to deeply thank my supervisor Prof. Ulrich Maas for his invaluable discussions, unwavering support, and encouragement throughout my research. His insights into combustion, modeling, and numerical simulation have kept me on track and enriched my work immeasurably.

I would like to express my sincere gratitude to all my colleagues in Divisions 3.5 and 3.3 for the memorable moments and discussions we shared during my research period.

I am indebted to my family for their boundless love, encouragement, and understanding during this challenging yet rewarding endeavor. My sincerest gratitude goes to my parents, Manizheh and Zakaria, and my sisters, Bahar and Banafshe for their years of patience and encouragement throughout my life.

I owe my deepest gratitude to my husband, Nima Habashi, who gave me peace and love during the difficult times.

This work was partly supported by the INNO INDIGO BiofCFD program, for which I am grateful.

Ghazaleh Esmaeelzade
Braunschweig, April 2024

CONTENTS

LIST OF TABLES

ACRONYMS

CFD	Computational Fluid Dynamic
CI	Compression Ignition
CMC	Conditional Moment Closure
CRN	Chemical Reactor Network
CSTR	Continuously Stirred Tank Reactor
DME	dimethyl ether
DNS	Direct Numerical Simulation
EMST	Euclidean Minimum Spanning Tree
FFT	Fast Fourier Transform
GCI	Grid Convergence Method
HCCI	Homogeneous Charge Compression Ignition
HOMREA	HOMogeneous REAction
IEM	Exchange with the Mean
JSFR	Jet Stirred Flow Reactor
JSR	Jet Stirred Reactor
LES	Large Eddy Simulation
LIC	Line Integral Convolution
MC	Modified Curl
OpenFOAM	Open Source Field Operation and Manipulation
PaSR	Partially Stirred Reactor
PBR	Packed Bed Reactor
PDF	Probability Density Function
PFR	Plug Flow Reactor
PIMPLE	Pressure IMplicit with splitting of operator for Pressure Linked Equations
PISO	Pressure-Implicit Splitting of Operators
PIV	Particle Image Velocimetry
RANS	Reynolds-Averaged Navier-Stokes

RCM	Rapid Compression Machine
RHS	right-hand side
RMS	Root Mean Square
PSR	Perfectly Stirred Reactor
RTD	Residence Time Distribution
SGS	sub-grid scale
SIMPLE	Semi-Implicit Method for Pressure-Link Equations
STL	STereoLithography
TKE	Turbulent Kinetic Energy
WALE	Wall-Adapting Local Eddy-viscosity

LIST OF NOTATIONS

Roman Symbols

a_1	constants of specific heat capacity
A	surface between zones and wall
A_k	name of the chemical species
A_p	parameter related to flow physical properties
A_r	pre-exponential constant
A_s	surface of nozzle
c	speed of sound
C	concentration
C_0	initial concentration
C_p	heat capacity
C_ϕ	mixing rate constant
C_ϵ	model constant
C_s	Smagorinsky constant
C_λ	resistance coefficient

d	diameter of the jet
D	diameter of the reactor vessel
D_m	mass diffusivity
e	energy density
e_a	error in Richardson-extrapolation
E	residence time distribution function
E_a	activation energy
$\boldsymbol{f}$	frequency
$\boldsymbol{f}_{\text{mix}}$	mixing frequency
g	gravitational acceleration
G	decaying filter function
GCI	fine grid convergence index
G_r^0	free entalphy
$\mathcal{G}$	solution on the mesh set
h	specific enthalpy
$\mathcal{H}$	grid size
h	specific enthalpy
h_t	heat transfer coefficient
k	rate coefficient
K	turbulent kinetic energy
k_c	equilibrium constant
KE	kinetic energy
l	pipe length
L	length scale
M_i	molar weight of species i (kg/mol)
m	mass
$\dot{m}$	mass flow rate
M	molar weight (kg/mol)
n	normal direction to the face
n_R	total number of reactions
n_s	total number of species
n_z	total number of zones
p	pressure

$\mathcal{P}$	apparent order
Pe	Peclet number
PE	potential energy
Pr	Prandtl number
Q	volumetric flow rate
$\mathcal{Q}$	$\boldsymbol{\mathcal{Q}}$-criterion
Q_s	volumetric flow rate through the section of jet's cone
$\dot{Q}_h$	rate of heat transfer
r	grid refinement factor
r_n	radial position from the axe of the jet
R	radius of the spherical chamber of the reactor
R_0	gas constant
Re	Reynolds number
Re_N	Reynolds number based on nozzle conditions
$\boldsymbol{S}$	Strain rate tensor
s	integration variable in decaying filter function
Sc	Schmidt number
s_m	function in Richardson-extrapolation
t	time
T	temperature
T_s	Sutherland constant
u	flow velocity
u_exit	flow velocity at the outlet of the nozzle
U	specific internal energy
V	volume
w_l	volume of each cell
w	mass fraction
$\bar{w}$	the spatially averaged value of the mass fraction
W_m	function in Richardson-extrapolation
$\dot{W}_h$	rate of work
x	spatial coordinate
X	mole fraction
y	spatial coordinate

z	spatial coordinate

Greek Symbols

α	thermal diffusivity
β	temperature exponent
γ	specific weight of flow
Γ	transport coefficient
Δ_m	filter width
ϵ	dissipation rate
$\boldsymbol{\zeta}$	mass ratio
κ	wavelength
λ	gas thermal conductivity
μ	dynamic viscosity
ν	kinematic viscosity
ν_{rk}	stoichiometric coefficient
η	Kolmogorov length scale
ρ	density
$\boldsymbol{\sigma}$	viscous stress tensor
$\sigma_{i,j}$	Reynolds stress tensor
σ_{w_k}	species flux
σ_h	enthalpy flux
σ_m	normalized weighted standard deviation of the tracer mass fraction
τ	residence time
ϕ	scalar intensive property
ω_ϕ	source term
$\dot{\omega}$	molar rate for the formation of species
$\boldsymbol{\Omega}$	rotation tensor
$\dot{\boldsymbol{\Omega}}_m$	mass exchange rate

Superscripts

f	forward reaction
b	backward reaction

Subscripts

atm	conditions at atmospheric pressure
e	educts
ext	exact
in	value of a quantity at co-flow inlet boundary
init	initial
i	zone's number
k	chemical species
l	grid
0	largest scale size of turbulent structures
out	value of a quantity at outlet boundary
p	products
r	value of a quantity in a chemical reaction
res	residual value
sgs	subgrid scale
tot	total value
w	wall
η	Kolmogorov scale
ϕ	scalar variable

Symbols

$\Delta(\phi)$	change of ϕ
$(\phi)^T$	transpose of a matrix
$\langle\phi\rangle$	time average of ϕ
$\overline{\phi}$	Reynolds time-average of ϕ
ϕ'	root mean square of ϕ
$\tilde{\phi}$	density-weighted mean (Favre averaging) of ϕ
ϕ''	Favre fluctuations of ϕ

Part I

FUNDAMENTALS

1 INTRODUCTION

In recent decades, the demand for efficient, clean, and sustainable energy is rising (Herbinet and Dayma 2013). In order to meet this demand, existing conventional fuels are being replaced by novel and alternative fuels, namely biofuels, gas fuels, low sulphur fuels, hydrogen, etc., (Kolwzan and Narewski 2012, Moka *et al.* 2014). For example, dimethyl ether (DME) has recently emerged as an alternative for diesel fuel in Compression Ignition (CI) engines due to its ability to provide low emissions of hydrocarbons, carbon monoxide and NO_x, a high cetane number, and a low boiling point (Moshammer *et al.* 2015, Arcoumanis *et al.* 2008). Therefore, to understand the properties of fuels and their chemical kinetics, such as the reaction mechanism of chemical processes and the reaction rate, different heterogeneous and homogeneous experimental chemical reactors are used (Brown *et al.* 2002). The reaction rates in these chemical reactors are calculated differently depending on the operating thermodynamic conditions together with the physical state, surface areas, concentration, and dispersion of the reactants (Davis and Davis 2012).

In order to study homogeneous chemical kinetics under different thermodynamic conditions, various experimental facilities are used, such as the flow reactor (Vermeersch *et al.* 1991, Mueller *et al.* 1999, Dryer *et al.* 2014), static reactor (Denise *et al.* 1982, Wilk *et al.* 1989), shock tube (Curran *et al.* 1992, Tranter *et al.* 2001, Davidson *et al.* 2011, Burke *et al.* 2015a), Rapid Compression Machine (RCM) (Mittal and Sung 2006, Drost *et al.* 2019, Donovan *et al.* 2004), and Jet Stirred Reactor (JSR) (Dagaut *et al.* 1986, Herbinet and Dayma 2013, Moshammer *et al.* 2015, Tang *et al.* 2022). Among them, shock tube and RCM are employed to validate chemical kinetics mechanisms for the temperature range of 800 - 2500 K/pressure range of 2 - 80 bar and temperature of 400 - 1200 K/pressure of 5 - 80 bar, respectively (Goldsborough *et al.* 2017). On the other hand, both reactors only provide valuable information on global reactivity and product formation, and their potential to provide numerous products is limited (Herbinet and Battin-Leclerc 2014). Because experimental uncertainties arising from temperature gradients occur in

the higher operating temperature range in both reactors (Herbinet and Battin-Leclerc 2014). Such uncertainties are smaller in the JSRs compared to other facilities due to lower operating temperatures and also sufficient preheating of the gases, which reduce temperature gradients (Azay and Côme 1979).

More specifically, the JSR is a type of Continuously Stirred Tank Reactor (CSTR) in which fresh reactants are continuously entered into a constant-volume reactor and products withdrawn (Lignola and Reverchon 1988). The JSRs are typically used to investigate the thermal decomposition and oxidation processes of the gas phase composition (Herbinet and Dayma 2013) at temperatures and pressures up to 1300 K and 30 bar, respectively (Goldsborough *et al.* 2017). Furthermore, the ideal JSRs should provide a fully mixed composition with a turbulent mixing time scale much smaller than the chemical reaction time scale. Hence, the mean values of thermochemical variables can be used to express mean chemical reaction rates (Chen 1997). In addition, a homogeneous distribution of temperature and concentration is captured within a well-stirred reactor (Davani and Ronney 2017). On the contrary, imperfect mixing inside the JSR significantly influences the combustion properties since the fluid dynamics is strongly perturbed and an inhomogeneous temperature distribution with multiple peaks is created (Lignola and Reverchon 1986). Therefore, as much as the performance of the real JSR is closer to the ideal one, the mixing quality is better. Some of the other advantages of the JSR setup compared to the other mentioned facilities are noted as follows.

- The possibility of easily coupling the JSRs to various analytical devices for measuring the composition of the mixture at the outlet (Herbinet and Dayma 2013, Moshammer *et al.* 2015).
- The possibility of connecting the JSR to a pressure chamber and an oven to perform reactions at low to intermediate temperatures and pressures ranging from atmospheric up to 30 bar (Dagaut *et al.* 1986).
- The JSR can be operated in steady state (Dagaut *et al.* 1986, 2005).
- Constructing the spherical JSRs with quartz material leads to minimizing the surface reaction (Herbinet and Dayma 2013).
- Performing the JSR under very dilute conditions results in minimizing unsteady thermodynamic conditions and heat release

over the length of the reaction zone (Fischer *et al.* 2000, Rotavera *et al.* 2011).

These benefits can only be achieved if sufficient mixing is provided by the nozzles installed inside the JSR. It is noted that the coupling of turbulence and chemistry in chemical reactors is of great importance (Celis and da Silva 2015); i.e., increasing turbulence affects the chemical source terms, leading to the generation of additional heat, and increasing temperature also affects turbulence. Accordingly, a fundamental understanding of the macro- and micro-mixing processes within a spherical JSR and the effect of high-intensity turbulent mixing on the reactor characteristics are the focus of the present study.

Besides the advantages mentioned earlier, there are some difficulties associated with the experimental measurements on the JSR setup (Dagaut *et al.* 1986, Herbinet and Dayma 2013). Such as surrounding the JSRs with an oven and a pressure chamber to control the operating temperature and pressure, limits the optical accessibility of the flow interactions during the reaction (Herbinet and Dayma 2013). Furthermore, the experimental measurement tools collect samples through a vessel that is connected to the outlet of the JSR; therefore, an average concentration of the products is obtained from the experimental data (Moshammer *et al.* 2015). Hence, the experimental facilities cannot capture the details of the flow field characterization during the reaction process and the complex interaction of multiple jets originating from the nozzles. The aim to fill the gap of experimental data motivates the use of numerical approaches to gain more insight into the physics of turbulent flow within the JSRs. The numerical modeling of the turbulent reacting flow in a stirred reactor has been performed using Direct Numerical Simulation (DNS) (Sbrizzai *et al.* 2006, Verzicco *et al.* 2004), and Reynolds-Averaged Navier-Stokes (RANS) (Davani and Ronney 2017, Gil and Mocek 2012, De Oliveria *et al.* 2013), and Large Eddy Simulation (LES) turbulence models (Revstedt *et al.* 1998, Zhao *et al.* 2021).

The application of the DNS provides fully resolved data for the prediction of the turbulent flow field; however, the computational time is very expensive. In addition, the RANS approach solves the governing equations based on the time-averaged values and models all scales of eddies. This turbulence model requires less computational time and is the most practical approach for turbulence simulations (Pope 2000). The turbulent flow transport processes through a spherical JSR are predicted using the RANS turbulence modeling

in the literature (Davani and Ronney 2017, Gil and Mocek 2012, De Oliveria *et al.* 2013). Above all, applying a filtering method to the computational grid in the LES modeling filters the length scales of the turbulent structures in such a way that the largest eddies will be resolved by the governing equations, and only the smallest scales are modeled. Due to the importance of the turbulence-chemistry interaction inside the JSR, the Computational Fluid Dynamic (CFD) analysis using the highly-resolved LES modeling can represent the mixing quality through the reactor. It should be noted that the simulation of the spherical JSR with four inclined nozzles using the LES approach has not been studied so far.

In the present study, the following key questions are addressed:

- How are the characteristics of the flow field inside a JSR with a spherical-shaped vessel and four inclined nozzles using the LES turbulence modeling?
- What is the level of homogeneity and uniformity of the flow inside a JSR?
- How would be the performance of the spherical JSR if we change the thermodynamic operating conditions and the geometrical parameters such as the diameter of the nozzle and the spherical vessel?
- Can the inhomogeneity within the JSR be captured by a theoretical model if the real JSR does not follow an ideal CSTR?
- Which parameters of the inhomogeneous distributions of the initial mole fractions of the reactants, the reactor volume, the wall temperature, and the heat transfer coefficient capture the inhomogeneity within the JSRs?
- How can the mixing performance inside the reactor be improved by proposing an alternative design of the JSR?

To address these questions, a comprehensive numerical study is performed, divided into two main parts. The first part describes the characterization of the flow field and mixing process through a non-reacting tracer-decay study using the open source CFD toolbox Open Source Field Operation and Manipulation (OpenFOAM)-V.6 (Weller *et al.* 1998). Therein, reaction is neglected and the mixing quality within the JSR is analyzed, including quantitative and qualitative flow visualization, Turbulent Kinetic Energy (TKE), Residence

Time Distribution (RTD), and standard deviation of the tracer mass fraction (Esmaeelzade *et al.* 2021, 2019) using the LES modeling. Further, to improve the numerical results, the modeling of turbulent nozzles and the flow through the nozzles are added to the domain of numerical computation. Next, a parametric study is also carried out to evaluate the mixing quality considering different geometrical parameters and thermodynamic conditions. More specifically, the mixing process is studied by varying the diameter of the nozzle outlets and the JSR vessel at different operating pressures and temperatures.

As mentioned in the literature review (Stoehr *et al.* 2015, Abdalla *et al.* 1982), a significant sustained temperature oscillation and mixture inhomogeneity within the JSR were captured. More specifically, Abdalla *et al.* (1982) measured fluctuations of the temperature field and species concentrations in a conical JSR. They showed that the temperature fluctuations are not uniformly distributed within the reactor and increase dramatically at the edge of the JSR and along the wall. Furthermore, Patel *et al.* (2010) discussed that the performance of a laboratory-scale continuous stirred-tank reactor is significantly affected due to the presence of inhomogeneity and short circulation of the unreacted species. Therefore, it could be argued that the use of four turbulent jets inside the JSRs may not result in a fully mixed and homogeneous mixture. Consequently, the assumption of ideal mixing in the Perfectly Stirred Reactor (PSR) model (Dryer *et al.* 2014, Battin-Leclerc 2008, Herbinet and Battin-Leclerc 2014, Brown *et al.* 1998), which is typically applied to the CSTRs for modeling chemical kinetics, may not be applicable to the non-ideal JSRs. In this study, in order to identify the origin of inhomogeneity inside the non-ideal spherical JSRs, a multi-zone model is developed.

In order to overcome the limitations of the PSR and the single zone models, effective predictive models have been developed such as multi-zone models (Bissoli *et al.* 2016, Kodavasal *et al.* 2013) and Probability Density Function (PDF) (Chen 1997) approaches. These methods are used to perform detailed chemistry studies on various combustion facilities, taking into account thermal and composition nonuniformity. The multi-zone models emphasize chemical kinetics together with mixture composition and thermal stratification rather than resolving small-scale fluid dynamics (Hultqvist *et al.* 2001, Bissoli *et al.* 2016). In these models, the combustion chamber is divided into a number of discrete zones or well-mixed reactors with consideration of composition and thermal inhomogeneities (Kodavasal

et al. 2013). For example, in the "Ballon type" multi-zone model, the combustion cylinder is divided into several reactors (zones) to predict the engine performance of a Homogeneous Charge Compression Ignition (HCCI) engine (Kodavasal *et al.* 2013). However, heat and mass exchange between zones are neglected in this model; only heat loss from each zone to the cylinder wall is considered (Kodavasal *et al.* 2013, Andreatta 1995). Empirical correlations are also used to predict the overall heat loss (Woschni 1967, Annand 1963, Hohenberg 1979). Moreover, the "Onion-skin" multi-zone approach was applied in the HCCI engine during the compression and expansion phases of a four-stroke cycle by Bissoli *et al.* (2016). Their approach divides the reactive volume into multiple zones, while the exchanges of heat and mass are limited between adjacent zones based on mixing rates determined by turbulent length scales. For the rapid compression expansion machine, Werler *et al.* (2017) used the onion model to compare the numerical approach with the experiments. In their model, mass and heat exchange are only considered at the interface of two nearby zones. However, the assumption of exchange to the nearby zones cannot be applied in the current study because, according to the spherical JSR design, a high-intensity flow stream is simultaneously injected into the vessel by four turbulent jets, and all cells in the computational domain are involved during the auto-ignition process. Therefore, to accurately predict the behavior of the non-ideal JSRs, the exchange of mass and heat between all zones in a reactor network is necessary. Furthermore, the spherical chamber of the JSR, unlike the HCCI engine and rapid compression machines, has no moving parts; therefore, the volume of each zone is kept constant in the studied multi-zone model.

In addition, the hybrid CFD-Chemical Reactor Network (CRN) approach is utilized in geometrically complex practical gas turbine combustors (Novosselov *et al.* 2006, Innocenti *et al.* 2018, Sturgess and Shouse 1996) to predict the exhaust emission. In these models, the total domain of the combustor is divided into a number of PSR, Plug Flow Reactor (PFR), and mixed models according to the local flow conditions, which are followed by CFD results. Depending on the complexity of the flow field, emissions, and blowout conditions, different zones are physically defined. Novosselov *et al.* (2006) applied a CRN model to a dry low emission gas turbine combustor that consists of 31 chemical reactors, including several distinct regions such as the main flame zone, the pilot flame zone, the center recirculation zone, and the post flame zone. To reduce computational

costs, a low number of reactors (zones) is considered in this study to represent the concept of the proposed model applied to a non-ideal JSR. Furthermore, the developed zero-dimensional multi-zone model considers chemistry zones that are independent of physical space.

The Probability Density Function (PDF) approach is based on chemistry space instead of physical space (Kraft *et al.* 2000, Pitsch *et al.* 1998). Indeed, chemical kinetics are addressed by transforming coordinates from the physical space in the combustion chamber to coordinates in pure chemistry space (Kodavasal *et al.* 2013, Bissoli *et al.* 2016). Maigaard *et al.* (2003) used a stochastic model that can simulate the effect of thermal inhomogeneity in the combustion chamber of a HCCI engine caused by the thermal boundary layer adjacent to the cylinder walls on the combustion process. Moreover, the joint scalar PDF of the Partially Stirred Reactor (PaSR) models was developed by Chen (1997) to reflect the effects of the unmixed levels of the reacting flows. More specifically, different mixing models were so far used to mimic the finite rate mixing of particles in the stochastic simulations such as Exchange with the Mean (IEM) (Sabel'nikov *et al.* 2006), Modified Curl (MC) (Ren and Pope 2004), Conditional Moment Closure (CMC) (Klimenko and Bilger 1999), and Euclidean Minimum Spanning Tree (EMST) models (Subramaniam and Pope 1998), etc., (Magnussen 1981, Krisman *et al.* 2014, Celis and da Silva 2015). While such PDF approaches mimic the stochastic character of the mixing, it is also desirable to analyze the sensitivity of the reaction process in PaSR using a simple deterministic model, which allows performing parametric studies with minimal computational effort, while at the same time accounting for the interaction of chemical reaction and mixing in the reactor. To that end, a deterministic, zero-dimensional multi-zone model is developed and then applied in the simulation tools of HOMogeneous REAction (HOMREA) (Maas and Warnatz 1988).

The developed model is structured in such a way that the total volume of the reactor is divided into a number of individual zones that interact with each other in terms of mass and heat exchange, while keeping the volume of the zones constant over time. Indeed, distributing the thermodynamic variables nonuniformly into a number of representative zones causes the inhomogeneity to be captured in the non-ideal JSR. Also, the heat transfer coefficient, the wall temperature, the initial mole fraction of the reactants, and the size of the zone volume can be randomly distributed over each zone

in a network of the reactor in order to reflect the inhomogeneous feature of the real JSRs. According to the multi-zone model, the interaction between the zones is also modeled using a mass exchange model, which depends on the mass of the interacting zones and the turbulent mixing.

In this thesis, flow field analysis using CFD tools and HOMREA provides a comprehensive understanding of mixing quality and inhomogeneity within the JSR. In order to improve the mixing efficiency inside the reactor, an alternative configuration of nozzles for the spherical JSR is proposed. The mixing parameters in the proposed JSR design are then investigated.

2 JET STIRRED REACTOR

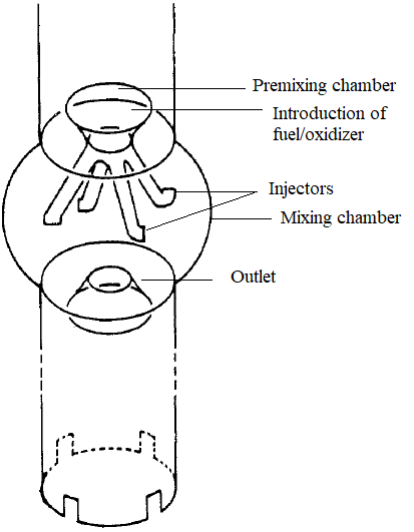

Figure 2.1: Schematic of the JSR setup with four inclined nozzles designed by Dagaut *et al.* (1986)

A schematic of a spherical JSR with four inclined nozzles is illustrated in Fig. 2.1. In this setup, the preheated fuel/diluent mixture meets the oxidizer/diluent mixture in the premixing section (upstream of the nozzles in Fig. 2.1). The mixture of fuel/oxidizer/diluent is then introduced into the mixing chamber of the JSR through four turbulent nozzles. High-intensity turbulent jets issuing from the nozzles pointing in four different directions (upward, downward, and horizontal) result in a mixed composition inside the JSR. Note that, the temperature and pressure of the chamber can be elevated using an electrically heated oven and a pressure-resistant jacket. Finally, the products leave the reactor through the outlet situated at the bottom of the mixing chamber. Subsequently, the products are analyzed as a function of reactants, residence time, and thermodynamic variables (Glaude *et al.* 2010, Dubreuil *et al.* 2007, Moshammer *et al.* 2016).

As mentioned in Chapter 1, an ideal JSR provides a perfectly mixed composition where temperature and species concentration are homogeneously distributed independently of time and space. Such an ideal JSR is desired to be obtained by employing highly-turbulent jets in a spherical vessel (Dagaut *et al.* 1986). Therefore, in order to achieve the homogeneity of the mixture, the design of the JSR vessel and the arrangement of the nozzles are crucial.

The spherical design of the JSR having four inclined nozzles situated in the equatorial plane was first proposed by Matras and Villermaux (1973) and later built by Dagaut *et al.* (1986). Analyzing the distribution of residence time through the JSR revealed adequate mixing under pressure up to 10 bar for the mean residence time from 0.01 s to several seconds (Dagaut *et al.* 1986). At the same time, the impact of good mixing on the combustion process of *n*-heptane and *i*-octane within a stainless-steel Jet Stirred Flow Reactor (JSFR) with an internal volume of 100 cm^3 and four crossed nozzles was studied (Lignola and Reverchon 1986). The experimental apparatus design of Lignola and Reverchon (1986) was capable of measuring residence time as short as 0.01 s at temperatures up to 1000 K and pressure of 20 bar. Later, Cavaliere *et al.* (1993) utilized the JSFR to study the low-temperature oxidation and ignition of *n*-tetradecane under high pressure similar to diesel-like conditions. Furthermore, using a crossed and inclined configuration of the nozzles inside the spherical JSR can affect the mixing intensity, as investigated in Ref. (Ayass *et al.* 2016).

In addition to the spherical reactors, a cylindrical configuration of the JSR is studied by David *et al.* (1979). They showed that their design is capable of providing sufficient macro-mixing for the residence time range of 0.5 - 4 s together with high heat transfer at the walls (David *et al.* 1979). An improvement to the standard design of the spherical JSR has also been made by Rota *et al.* (1994). In their experimental setup, the exhaust gas is directed through four holes, which are located in the upper part of the reactor and consequently preheat the inflow mixture. They found good agreement between the experimental results and the model predictions for the oxidation of ethane.

In recent years, Davani and Ronney (2017) proposed an arrangement of eight impinging turbulent jets surrounded by the concentric annular outlets in a spherical vessel of the JSR. They outlined that their design significantly improved the mixing quality for the study of chemical kinetics and provided inferred reaction rate con-

stants (Davani and Ronney 2017). Afterward, the concentric annular outlet design is changed by applying four pairs of jets to induce four vortices with different directions, the so-called inwardly off-center shearing JSR (Zhang *et al.* 2018). The performance of this reactor is enhanced in terms of mixture uniformity and a narrower residence time distribution.

Note that among several types of JSR such as toroidal reactor (Nenniger *et al.* 1985, Lignola and Reverchon 1988), cylindrical (David *et al.* 1979), conical (Gil and Mocek 2012), and spherical configurations (Dagaut *et al.* 1986), the mixing level is significantly improved in the spherical JSR by minimizing the dead volumes. Gil and Mocek (2012) compared the mixing level and turbulent Peclet number in three types of cylindrical, conical, and spherical JSRs and concluded that the spherical JSR provides a more homogeneous mixture. However, the instabilities and temperature oscillations that affect the homogeneity of a JSR are later observed by Lammersen *et al.* (2013) and Stoehr *et al.* (2015). As a result of the high-intensity mixing inside the spherical JSRs, the present study focuses on this type of reactor.

2.1 DEVELOPMENT REGION OF THE TURBULENT JETS

Since turbulent jets have a significant impact on the mixing within the JSR, the evolution of the flow field through the nozzle and the distribution of velocity are matters of concern. The mixing performance of the free turbulent jets issuing from different types of nozzles, such as contoured (or smooth contraction) nozzle, sharp-edged orifice, and straight pipe-shaped (tube nozzle), could be different due to various underlying turbulent structures and initial conditions (Mi *et al.* 2001a).

In the straight pipe-shaped nozzle, the velocity profile at the entry of the nozzle has a top-hat shape because the shear layer is not yet formed at the entrance of the nozzle (Mi *et al.* 2001b). Further, through the nozzle, a thin layer of fluid adheres to the wall of the nozzle and forms a velocity profile from zero at the walls to a maximum at the axis of the nozzle (Keulegan and Beij 1937). Note that the velocity profile inside the nozzle changes gradually in the turbulent regime and leaves the exit of the nozzle according to the power law (Pope 2000, Mi *et al.* 2001a). In addition, due to the frictional energy loss caused by the fluid viscous effects through the straight pipe nozzles, a pressure drop in the direction of flow movement is expected (Keulegan and Beij 1937).

After all, the pipe nozzles installed inside the studied JSR are not straight and have curvatures at the entrance and the exit of the nozzles pointing upwards, downwards, and in horizontal directions. Therefore, due to these curvatures, the velocity profile through the nozzles is not symmetrical across the pipe. According to Keulegan and Beij (1937), in the curved pipe nozzles with laminar flow regime, the maximum velocity is located between the center and the wall closer to the outer radius of the bend due to centrifugal force; therefore generates strong secondary motions or streamwise vorticity. However, in the turbulent regime, the maximum value of the velocity profile moves towards the inner radius due to the presence of smaller secondary motions at the inlet (Al-Rafai *et al.* 1990). In addition, due to the velocity distortion along the pipe axes, a larger pressure loss occurs compared to the similar condition in a straight pipe nozzle (Keulegan and Beij 1937).

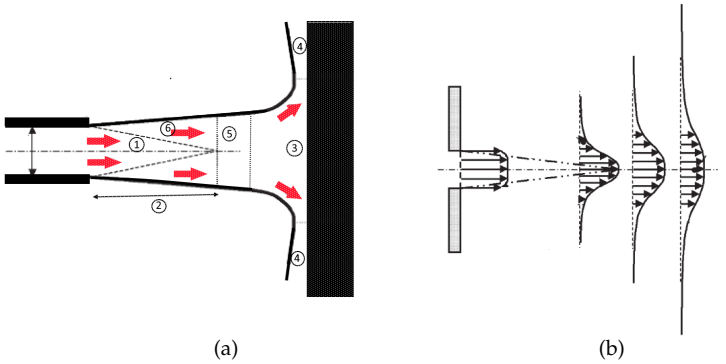

Figure 2.2: Schematic of (a) an jet impinges on the surface and the surrounding regions: 1) potential core, 2) initial free jet, 3) stagnation region, 4) wall jet region, 5) decaying jet region, 6) shear layer region, (b) the velocity profile exited by a jet (Zuckerman and Lior 2006)

In addition to the importance of the fluid flow passing through the nozzles, when the flow exited by the nozzle hits the spherical wall of the JSR, mixing intensity is improved due to the transfer of mass and energy (Zuckerman and Lior 2006). Figure 2.2a illustrates different regions formed by a jet (Zuckerman and Lior 2006). Depending on the upstream flow field and the geometry of the nozzle outlet, the velocity profile at the exit of the nozzle could be different (Mi *et al.* 2001a). Note that the initial magnitude of the veloc-

ity is preserved along the potential core of the free jet (Zuckerman and Lior 2006) (See region 1 in Fig. 2.2a). The velocity gradient outside of the core creates a progressively increasing shear layer which transfers momentum outward. Therefore, the maximum velocity at the center-line is decreased along the shear layer region (Zuckerman and Lior 2006). As the shear layer moves downstream, a decaying jet region forms (see region 5 in Fig. 2.2a). In this region, the energy of the jet decays and the profile of velocity is spatially widened. This means that the axial velocity is decreased in the center-line along the sides of the jet and forms a Gaussian velocity profile (Viskanta 1993). Afterward, a stagnation region is created when the jet impinges on the in-front wall because the axial velocity is converted to the radial velocity on both sides. According to Zuckerman and Lior (2006), higher shearing stress leads to stretched vortices in the flow, which increases turbulence. After impingement of the jets on the wall, the flow moves parallel to the walls and forms a wall jet region. Figure 2.2b shows the velocity profile developed at the exit of the nozzles and along the decaying region.

2.2 CONSTRUCTION OF THE JSR

In order to assure sufficiently mixing inside the JSR, the following design criteria developed by the theory of the free jet (David and Matras 1975, Lignola and Reverchon 1988) must be taken into account. First, the flow coming from the jets must be turbulent in order to provide adequate micro-mixing (Herbinet and Dayma 2013). Therefore, the Re_{N} number, which is determined experimentally, must be larger than 800 as follows (Herbinet and Dayma 2013),

$$Re_{\mathrm{N}} = \frac{\gamma(2r_n)}{\mu}\frac{Q_s}{\pi\, r_n^2} > 800\,, \tag{2.1}$$

where r_n, Q_s, γ, and μ denote the radial distance from the axe of the jet, the volumetric flow rate through the section of jet's cone, specific weight, and dynamic viscosity, respectively.

Second, the nozzle's outflow velocities must not exceed the speed of sound to prevent supersonic flow conditions (Herbinet and Dayma 2013), which is described by,

$$\boldsymbol{u}_{\mathrm{exit}} = \frac{V}{\tau A_s} = \frac{4R^3}{3\tau d^2} \leq c\,. \tag{2.2}$$

In the above equation, u_{exit}, V, A_s, R, τ, d, and c represent the velocity at the outlets of the nozzles, the total volume of the reactor, surface of the nozzle, the radius of the reactor, mean residence time, diameter of the nozzles, and the sound speed, respectively. To be more specific, limiting subsonic jet velocities in a JSR helps avoid shock wave disturbances, maintains efficient mixing, and promotes combustion stability. Equation 2.2 provides a limit for the maximum mean residence time (Herbinet and Dayma 2013).

At the latter, the internal recycling stream inside the reactor should be provided by the jets (Herbinet and Dayma 2013). To this end, the following empirical relationship should be satisfied (Lignola and Reverchon 1988, David and Matras 1975),

$$\frac{A_p R}{d} > 19\,, \tag{2.3}$$

where A_p is a dimensionless parameter depending on physical properties of flow inside the reactor (Herbinet and Dayma 2013).

2.3 RESIDENCE TIME

To characterize the behavior of the CSTRs, the residence time data and its functions such as the mean residence time τ, the residence time distribution function $E(t)$, the cumulative distribution function, and the standard deviation of the species mass fraction are commonly studied (Fogler 1999, Wolf and Resnick 1963). These functions help us to understand how far the studied real reactor is from the ideal reactor (CSTR, PFR, Packed Bed Reactor (PBR)). Moreover, we will be able to diagnose the problems with the real reactors, such as dead volumes and by-passing (short circulation), errors in the determination of the average residence time, and lag in response (Fogler 1999) using the residence time functions. Wolf and Resnick (1963) concluded that a system may be described by a combination of the mentioned plausible flow models by comparing the experimental data to the theoretical model.

The mean residence time is an effective parameter for evaluating mixing efficiency and characterizing bulk flow in the JSR (Fogler 1999). More specifically, τ represents the amount of time a fluid element spends on average in the reactor. The following formula is used to theoretically compute the mean (nominal) residence time for an ideal reactor,

$$\tau = V/Q\,, \tag{2.4}$$

where V and Q are reactor volume, and volumetric flow rate, respectively.

To calculate residence time experimentally, two methods of pulse input and step input experiments are generally used (Fogler 1999). In this study, to validate the non-reacting and the reacting simulations of JSR, the experimental apparatus of the negative step tracer technique from the work of Ayass *et al.* (2016) and Moshammer *et al.* (2016) is used, in which the response of continuously injected inert gas or reactants inside the reactor is studied. According to the JSR setup studied in Ref. (Ayass *et al.* 2016), a tracer is injected into the reactor at the time of zero and then the tracer concentration and the RTD functions are calculated at the outlet as a function of time (Fogler 1999). The tracer is typically chosen as a non-reactive species with physical characteristics similar to those of the studied reacting mixture in order to avoid being affected by the reactor surface (Fogler 1999).

Mean residence time can also be calculated from numerical simulation results. From the perspective of numerical simulation, the mean residence time is the time-span when the concentration of the tracer drops below 1/e of its initial value (Crawford 2014). The mixing quality of the JSR can be determined by comparing these values to the one that corresponds to the ideal reactor. Thus, the tracer decay at the reactor outlet is calculated by performing the following material balance on the CSTR as,

$$V \frac{\mathrm{d}C_{\mathrm{out}}}{\mathrm{d}t} = -Q\, C_{\mathrm{out}}\,, \tag{2.5}$$

where time is denoted by t. Integrating from both side of Eq. 2.5 gives the concentration at the outlet,

$$C_{\mathrm{out}}(t) = C_0\, \mathrm{e}^{\frac{-t}{\tau}}\,, \tag{2.6}$$

where $C_{\mathrm{out}}(t)$ represents the outlet concentration at the time of t for the case of the JSR and C_0 the initial steady-state concentration of the tracer. Moreover, the residence time distribution function E is defined as (Fogler 1999),

$$E(t) = \frac{C(t)}{\int_0^\infty C(t)\,\mathrm{d}t.}. \tag{2.7}$$

The distribution of residence time describes how much time different fluid elements have spent in the reactor. Replacing Eq. 2.6 into Eq. 2.7 leads to the following formula (Fogler 1999),

$$E(t) = \frac{1}{\tau} e^{-t/\tau}. \tag{2.8}$$

We can also derive the normalized RTD function $E(t/\tau)$ from Eq. 2.8 as follows (Ayass *et al.* 2016),

$$E(t/\tau) = \tau E(t) = e^{-t/\tau}. \tag{2.9}$$

Here, $E(t/\tau)$ represents the amount of tracer in the reactor normalized by its initial amount, after the normalized time period t/τ. It can be inferred from Eqs. 2.8-2.9 that for two different volumetric flow rates at identical times, the value of $E(t)$ may differ significantly. However, for a given value of t/τ, the value of $E(t/\tau)$ is the same, regardless of the size of a perfectly mixed CSTR (Fogler 1999). Therefore, to directly compare the flow performance inside reactors of various sizes, the normalized RTD function is developed.

In addition, another parameter used to study mixing within the reactor is the normalized weighted standard deviation. More specifically, macro-mixing is concerned with the overall mixing process of the reactants at large scales (up to the size of the reactor diameter), while micro-mixing is related to the local mixing process that occurs at small scales (down to the molecular level) (Fogler 1999). Depending on the selected filter width, the normalized weighted standard deviation is represented by,

$$\sigma_m = \sqrt{\frac{\sum (w - \bar{w})^2 \cdot V_l}{\sum \bar{w}^2 \; V_l}}, \tag{2.10}$$

where V_l, w, and $\bar{w}$ are the volume of each cell, the species mass fraction, and its spatially averaged value (over each cell), respectively. Furthermore, Eq. 2.10 represents how far the composition homogeneity is from its spatially-averaged value. As long as σ_m is closer to zero, a homogeneous composition is obtained inside the reactor, while larger σ_m represents a more nonuniform composition. Note that the normalized weighted standard deviation using mass as the weighting factor (mass-weighted value of 0.116) gives similar results to the volume-weighted value σ_m of 0.114 because temperature and density do not change significantly for a non-reacting mixture.

2.4 KINETICS AND RATE OF REACTION

The JSRs are in general used for the development and the validation of detailed gas phase chemical mechanisms. These chemical mechanisms contain a series of elementary reactions (one-step global reaction) that happen between specific species because of their collisions. As a result of numerous elementary processes inside the chemical reactor, the global reactions are formed (Warnatz *et al.* 2006, Peters 2000). According to Warnatz *et al.* (2006), if the time scale of chemical reactions is comparable to the time scale of molecular transport processes, the rate of chemical reactions is of great importance. The following is an elementary reaction with the consideration of the total number of species n_s and the number of reactions n_R (Warnatz *et al.* 2006),

$$\sum_{k=1}^{n_s} \nu_{rk}^{(e)} A_k \quad \xrightarrow{k_r} \quad \sum_{k=1}^{n_s} \nu_{rk}^{(p)} A_k \,, \quad r = 1, ..., n_R \tag{2.11}$$

where A_k denotes the name of the chemical species and k_r the rate coefficient of the reaction r. Moreover, $\nu_{rk}^{(e)}$ and $\nu_{rk}^{(p)}$ are the stoichiometric coefficients of reactants and products, respectively. The molar rate of formation of the ith species $\dot{\omega}_i$ is calculated by summation over the rate equations of all elementary reactions (Warnatz *et al.* 2006),

$$\dot{\omega}_i = \sum_{r=1}^{n_R} k_r (\nu_{ri}^{(p)} - \nu_{ri}^{(e)}) \prod_{k=1}^{n_s} C_k^{\nu_{rk}^{(e)}} \,, \quad i = 1, ..., n_s \tag{2.12}$$

where C_k is the concentrations of species of k.

Usually, for each elementary reaction, there is a backward reaction. The rate coefficient of forward reaction k^f and backward reaction k^b are related to each other by the equilibrium constant of k_c (Warnatz *et al.* 2006),

$$k_c = \frac{k^f}{k^b} \,, \tag{2.13}$$

where equilibrium constant of the reaction of r, $k_{c,r}$ is determined by the change of free enthalpy of the rth reaction as following formula (Warnatz *et al.* 2006),

$$k_{c,r} = \Big(\frac{p_{atm}}{R_0 T}\Big)^{\sum \nu_{rk}^{(p)} - \nu_{rk}^{(e)}} exp(-\frac{\Delta G_r^0}{R_0 T}) \,, \tag{2.14}$$

here ΔG_r^0, p_{atm}, T and R_0 are the change of free enthalpy under 1 atm, the atmospheric pressure, temperature and the gas constant, respectively. Furthermore, the rate constant k_r is non-linearly dependent to temperature given by Arrhenius equation as follows (Peters 2000),

$$k_r = A_r T^{\beta} exp(-E_a / R_0 T)\,. \tag{2.15}$$

In the above equation, A_r, β, and E_a represent the pre-exponential constant, the temperature exponent, and the activation energy, respectively. Note that the pre-exponential factor is related to the oriented collision between molecules in a reaction and the exponential term to the quantity of collisions providing adequate energy to overcome the reactions' activation barrier (Pauling 1970). Therefore, the calculation of the chemical reaction rates based on the Arrhenius law is highly nonlinear (Warnatz *et al.* 2006, Iavarone *et al.* 2021) as well as computationally expensive. Due to this, a number of models have attempted to simulate the average reaction rate; nevertheless, it is not possible to estimate this rate directly from average quantities such as species mass fractions, densities, or temperatures.

Part II

MATHEMATICAL MODEL

3

APPLIED MATHEMATICAL MODEL FOR OpenFOAM

In this chapter, the basic governing equations used in OpenFOAM (Section 3.1), the characteristics of turbulent flow (Section 3.2), modeling of turbulence structures (Section 3.3), calculation of turbulent kinetic energy (Section 3.4), and turbulent dissipation rate (Section 3.5) together with the thermophysical modeling (Section 3.6) are described in detail.

3.1 GOVERNING EQUATIONS

In this study, in order to simulate a reacting turbulent flow inside a spherical Jet Stirred Reactor (JSR), the solver of *reactingFoam* in the open source code of OpenFOAM is used. Based on this solver, a set of the following transport equations in terms of mass, momentum, energy, and species mass fraction equations are coupled to the ideal gas in the Cartesian coordinates (Poinsot and Veynante 2005),

$$\frac{\partial \rho}{\partial t} + \frac{\partial}{\partial x_j}(\rho u_j) = 0\,, \tag{3.1}$$

$$\frac{\partial}{\partial t}(\rho u_i) + \frac{\partial}{\partial x_j}(\rho u_j u_i) = \rho g_i - \frac{\partial p}{\partial x_i} + \frac{\partial \sigma_{ij}}{\partial x_j}\,, \tag{3.2}$$

$$\frac{\partial}{\partial t}(\rho h) + \frac{\partial}{\partial x_j}(\rho u_j h) = \frac{\mathrm{D}p}{\mathrm{D}t} + \sigma_{ij} \cdot \frac{\partial u_j}{\partial x_i} + \frac{\partial}{\partial x_j}\big(\rho\ \alpha\ \frac{\partial h}{\partial x_j}\big)\,, \tag{3.3}$$

$$\frac{\partial}{\partial t}(\rho w_{\mathrm{k}}) + \frac{\partial}{\partial x_j}(\rho u_j w_{\mathrm{k}}) = \frac{\partial}{\partial x_j}\big(\rho\ D_{m,\mathrm{k}}\ \frac{\partial w_{\mathrm{k}}}{\partial x_j}\big) + M_{\mathrm{k}} \cdot \dot{\omega}_{\mathrm{k}}\,, \tag{3.4}$$

where thermal diffusivity and the mixture specific enthalpy (the sum of the sensible and species formation enthalpy) are denoted by α and h, respectively. Further, ρ, p, $\boldsymbol{u}$, g, M, w, D_m, and $\dot{\omega}_{\mathrm{k}}$ are density, pressure, velocity, gravitational acceleration, the molar weight, the mass fraction, the mass diffusivity, and the source term related to the molar rate of formation of kth species per unit volume, respectively. The material derivation is defined as $\frac{\mathrm{D}\phi}{\mathrm{D}t} = \frac{\partial \phi}{\partial t} + \frac{\partial u_i \phi}{\partial x_j}$.

Moreover, assuming that the gas mixture can be considered as Newtonian fluid, the viscous stress tensor can be described as follows,

$$\sigma_{ij} = \mu \left(\frac{\partial u_i}{\partial x_j} + \frac{\partial u_j}{\partial x_i} - \frac{2}{3}\delta_{ij}\frac{\partial u_k}{\partial x_k} \right), \tag{3.5}$$

where μ is the dynamic viscosity and δ_{ij} the Kronecker delta.

In the current study, due to the complex geometry of the JSR and in order to increase the Courant number limit while ensuring simulation stability, the Pressure IMplicit with splitting of operator for Pressure Linked Equations (PIMPLE) algorithm for coupling pressure-velocity is chosen (Rezaeiravesh and Liefvendahl 2018). This algorithm is a hybrid between the Pressure-Implicit Splitting of Operators (PISO) and the Semi-Implicit Method for Pressure-Link Equations (SIMPLE), and must be calculated in the transient mode for larger time steps with larger Courant numbers (Venier *et al.* 2017).

3.2 TURBULENT FLOWS

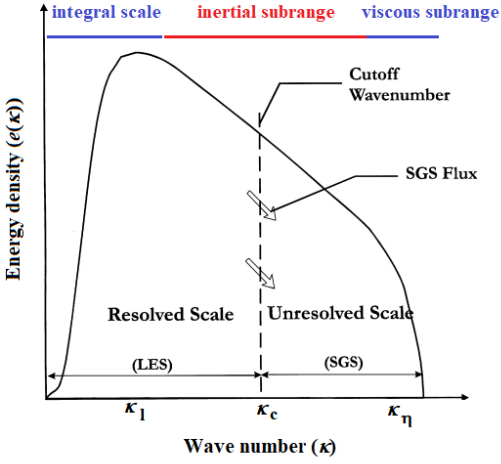

Figure 3.1: Schematic representation of the spectrum of the Turbulent Kinetic Energy (TKE) versus wave number

Turbulent flows are a representation of random and chaotic movement of flow motions on both the time and the spatial scales (Cantwell

1981, Pope 2000, Mathieu and Scott 2000). Due to the effect of turbulence on the successful mixing of chemical species, turbulent flows are drawing a lot of attention from the chemical industry. Indeed, the diffusive nature of turbulence helps to transport mass and energy much more effectively than the laminar case flow. The Reynolds number is a transition point between laminar and turbulent flows which represents fluid inertia to viscous forces as $Re = \boldsymbol{u}\, L/\nu$.

In turbulent fluids, eddies typically have a wide range of velocities, length scales, and times, from integral to Kolmogorov scales (Pope 2000). Figure 3.1 illustrates a schematic of the energy spectra over a wide range of wave numbers of flow length scales. In fact, the energy density $e(\kappa)$ represents the dependency of the TKE on the wave number κ. The largest scales, which absorb the energy from the mean flow, contain most of the energy of the turbulent unsteady motions and the smaller scales dissipate the turbulent energy into internal energy (Sheng *et al.* 2000, Pope 2000).

The energy containing range represents a range for the integral length scales where large-scales turbulent structures produce the highest turbulent kinetic energy (represented by k_1 in Fig. 3.1). In the inertial subrange, energy is transferred from the larger scales to the smaller scales; it means no more turbulent kinetic energy is generated or dissipated. The energy spectrum in this subrange follows the well-known -5/3 law. Furthermore, κ_c describes the cut-off wavenumber where the bandwidth is defined as $\Delta_m = 2\pi/\kappa_c$. Over the viscous subrange, the energy provided by the integral scales (flow-dependent) is dissipated by the dissipation subrange (universal small range) into internal energy (Sheng *et al.* 2000).

Pope (2000) approximated the largest scale size of the turbulent structure as L_0 and the turbulent velocity of these structures as u_0=$u_0(L_0)$. Accordingly, the Reynolds number based on the largest scale is calculated such that,

$$Re_0 = \frac{L_0\, \boldsymbol{u_0}}{\nu}. \tag{3.6}$$

Also, the smallest scales in turbulent flows are approximated by the Kolmogorov length scale η, the Kolmogorov velocity scale u_η, the Kolmogorov time scale τ_η (Pope 2000, Peters 2000). Therefore, the Reynolds number based on the Kolmogorov scales is calculated based on,

$$Re_\eta = \frac{\eta\, u_\eta}{\nu}, \tag{3.7}$$

where the Kolmogorov Reynolds number is approximated as unity (Pope 2000). Note that the small scales are related to each other by their dissipation rate ε and kinematic viscosity ν as follows,

$$\eta \equiv \left(\frac{\nu^3}{\varepsilon}\right)^{1/4}, \tag{3.8}$$

$$u_\eta \equiv (\nu\varepsilon)^{1/4}, \tag{3.9}$$

$$\tau_\eta \equiv \left(\frac{\nu}{\varepsilon}\right)^{1/2}. \tag{3.10}$$

Note that the ratio of the smallest to the largest scale turbulent motions is given by (Pope 2000),

$$\frac{\eta}{L_0} \equiv Re_0^{-3/4}, \tag{3.11}$$

$$\frac{u_\eta}{u_0} \equiv Re_0^{-1/4}, \tag{3.12}$$

$$\frac{\tau_\eta}{\tau_0} \equiv Re_0^{-1/2}. \tag{3.13}$$

One may conclude that in a highly turbulent regime having a large Reynolds number, the smallest eddies with a length of η are much smaller than those of the largest eddies with a length of L_0.

3.3 TURBULENCE MODELING

Due to the complexity of the turbulent structures in the turbulent flow regime, several approaches try to simplify turbulence modeling through computational fluid dynamics. The main approaches are Direct Numerical Simulation (DNS), Reynolds-Averaged Navier-Stokes (RANS), and Large Eddy Simulation (LES) (Pope 2000, Pitsch 2000, Wilcox 1998, Poinsot and Veynante 2005). The governing equations in the DNS solve the smallest structures down to the Kolmogorov length scales η. Therefore, the DNS approach represents very precise results. However, it is computationally expensive, especially in the presence of chemical reactions and it is only appropriate for basic geometries with low Reynolds flows (Pope 2000). According to the RANS turbulence model, all thermodynamic variables (velocity field, pressure, density, and temperature) are decomposed into mean and fluctuating terms. This implies that the Navier-Stokes equations are formulated in terms of the time-averaged flow field and that all the fluctuating components (turbulent structures)

are modeled using different turbulence models. The complexity of simulating turbulent flows is greatly reduced by the RANS simulations, although high-intensity and transient turbulent structures cannot be captured using this method (Poinsot and Veynante 2005). Another option is the LES turbulence model approach, which is widely used for turbulent combustion simulations. This approach performs low-pass spatial filtering over the control volume to filter larger turbulent motions from smaller scales. Using this filtering, the largest turbulent scales, which contribute the highest energy level to the transport of fluid particles, are resolved by the spatial-filtered Navier-Stokes equations and just the smallest scales, which are more uniform, are modeled by the sub-grid scale (SGS) models. The LES approach is actually a compromise between the DNS and the RANS turbulence models (Poinsot and Veynante 2005). It is worth mentioning that modeling the smallest scales in the LES is simpler than modeling the fluctuations in the RANS simulations (Morar 2014).

In the present study, highly-resolved LES modeling is chosen since the large-scale motions that control the mixing and transport of mass are impressed by the interaction of the inclined nozzles inside the JSR and should be resolved by the governing equations. The universal SGS motions, which behave independently from the boundary conditions, are modeled (Pope 2000). In the present study, Subsection 3.3.1 describes the low-pass filtering methods that are generally used for the LES approach. Later, the filtering method is applied to the governing equations as described in Subsection 3.3.2. Finally, the details of the Smagornisky model are given in Subsection 3.3.3.

3.3.1 *Filtering*

To separate the large (resolved) and the small (unresolved) scales in the LES approach, a low-pass filter is applied to the field of ϕ as follows (Leonard 1974, Pope 2000),

$$\overline{\phi}(\boldsymbol{x},t) = \int_{Do} G(\boldsymbol{x}-\boldsymbol{s})\ \phi(\boldsymbol{s},t)\ \mathrm{d}\boldsymbol{s}, \tag{3.14}$$

where $\boldsymbol{x}$, $\boldsymbol{s}$ are the coordinate and integration variable. Moreover, G is a decaying filter function (convolution kernel) on the computational domain of Do, and follows the expression of $\int_{Do} G(x)dx = 1$. This function damps fluctuations shorter than some characteristic filter width (Froehlich and Rodi 2000). Given that the turbulent

flows are randomly distributed, the instantaneous flow variable of $\phi(x,t)$ in the LES approach is decomposed into a resolved (filtered) part of ϕ^{res} and an un-resolved (residual or SGS) part of ϕ^{sgs} (Pierce 2001).

For compressible flows, the density fluctuation terms make the averaged governing equations more complicated. Therefore, a Favre averaging (density-weighted filtering) is introduced by splitting $\phi(x,t)$ into the time averaging $\widetilde{\phi}(x)$ and the remaining fluctuating part $\phi''(x,t)$ as follows (Pope 2000, Wilcox 1998),

$$\phi(\boldsymbol{x},t) = \widetilde{\phi}(\boldsymbol{x}) + \phi''(\boldsymbol{x},t), \tag{3.15}$$

where,

$$\overline{\rho\phi} = \overline{\rho}\widetilde{\phi}, \qquad \widetilde{\rho\phi''} = 0, \qquad \widetilde{\phi''} \neq 0\,. \tag{3.16}$$

3.3.2 *Formulation of the filtered governing equations: Applied mathematical model on the Large Eddy Simulation*

Applying the Favre filter operation to Eqs. 3.1 to 3.4 yields the following equations (Pope 2000),

$$\frac{\partial\overline{\rho}}{\partial t} + \frac{\partial}{\partial x_j}(\overline{\rho}\widetilde{u}_j) = 0\,, \tag{3.17}$$

$$\frac{\partial(\overline{\rho}\widetilde{u}_i)}{\partial t} + \frac{\partial(\overline{\rho}\widetilde{u}_j\widetilde{u}_i)}{\partial x_j} = \overline{\rho}g_i - \frac{\partial\overline{p}}{\partial x_i} + \frac{\partial\overline{\sigma}_{ij}}{\partial x_j} - \frac{\partial\left[\overline{\rho}(\widetilde{u_iu_j} - \widetilde{u}_i\widetilde{u}_j)\right]}{\partial x_j}\,, \tag{3.18}$$

$$\frac{\partial(\overline{\rho}\widetilde{h})}{\partial t} + \frac{\partial(\overline{\rho}\widetilde{u}_j\widetilde{h})}{\partial x_j} = \frac{\overline{\mathrm{D}p}}{\mathrm{D}t} + \frac{\partial}{\partial x_j}(\overline{\rho}\,\alpha\frac{\partial\widetilde{h}}{\partial x_j}) - \frac{\partial\left[\overline{\rho}(\widetilde{u_jh} - \widetilde{u}_j\widetilde{h})\right]}{\partial x_j}\,, \tag{3.19}$$

$$\frac{\partial(\overline{\rho}\widetilde{w}_{\mathrm{k}})}{\partial t} + \frac{\partial(\overline{\rho}\widetilde{u}_j\widetilde{w}_{\mathrm{k}})}{\partial x_j} = \frac{\partial}{\partial x_j}\left(\overline{\rho}D_{m,\mathrm{k}}\frac{\partial\widetilde{w}_{\mathrm{k}}}{\partial x_j}\right) - \frac{\partial\left[\overline{\rho}(\widetilde{u_jw_{\mathrm{k}}} - \widetilde{u}_j\widetilde{w}_{\mathrm{k}})\right]}{\partial x_j} + \overline{M}_{\mathrm{k}}\overline{\dot{\omega}}_{\mathrm{k}}\,. \tag{3.20}$$

In order to solve Eqs. 3.17-3.20 the following unclosed terms need to be modeled,

$$\sigma_{ij}^{\text{sgs}} = \bar{\rho}\,(\widetilde{u_iu_j} - \widetilde{u}_i\widetilde{u}_j) = \rho\widetilde{u_i''u_j''}, \tag{3.21}$$

$$\sigma_{w_k}^{\text{sgs}} = \bar{\rho}\,(\widetilde{u_jw_{\mathrm{k}}} - \widetilde{u}_j\widetilde{w}_{\mathrm{k}})\,, \tag{3.22}$$

$$\sigma_{h}^{\text{sgs}} = \bar{\rho}\,(\widetilde{u_jh} - \widetilde{u}_j\widetilde{h})\,, \tag{3.23}$$

where σ_{ij}^{sgs}, $\sigma_{w_k}^{\text{sgs}}$, and σ_{h}^{sgs} denote subgrid stress tensor, subgrid scale flux of species, and enthalpy, respectively.

3.3.3 *Subgrid scale modeling*

Smagorinsky model

For the modeling of subgrid-scales in the filtered governing equations, different turbulence models (closure model) are used in the LES such as Smagorinsky, Wall-Adapting Local Eddy-viscosity (WALE), subgrid-scale kinetic energy model, etc., (Germano *et al.* 1991, Bertolini *et al.* 2021, Smagorinsky 1963). In the present study, the Smagorinsky model is chosen because of its low computational costs (Smagorinsky 1963). More precisely, only subgrid-scale turbulence isotropy is considered in the standard Smagorinsky model, which facilitates possible large-scale turbulence anisotropy (Van Balen *et al.* 2010). Through the Smagorinsky model, the residual stress tensor is closed by the following eddy-viscosity model (Smagorinsky 1963),

$$\sigma_{ij}^{\mathrm{sgs}} - \frac{1}{3}\sigma_{kk}^{\mathrm{sgs}}\delta_{ij} = -2\,\nu_{\mathrm{sgs}}\,\bar{\rho}\,\left(\widetilde{S}_{\mathrm{ij}} - \frac{1}{3}\widetilde{S}_{\mathrm{kk}}\,\delta_{ij}\right), \tag{3.24}$$

where $\sigma_{kk}^{\mathrm{sgs}}$ and $\frac{1}{3}\sigma_{kk}^{\mathrm{sgs}}\,\delta_{ij}$ represents the anisotropic and isotropic stress tensor, respectively. The resolved strain rate $\widetilde{S}$ is obtained by,

$$\widetilde{S}_{\mathrm{ij}} = \frac{1}{2}\left(\frac{\partial \widetilde{u_i}}{\partial x_j} + \frac{\partial \widetilde{u_j}}{\partial x_i}\right). \tag{3.25}$$

In the Smagorinsky model, the subgrid scale viscosity is proportional to the magnitude of the filtered strain rate such that (Fureby *et al.* 1997, Weller *et al.* 1998),

$$\nu_{\mathrm{sgs}} \;=\; (C_{\mathrm{s}}\Delta_m)^2|\widetilde{S}_{\mathrm{ij}}|\,, \qquad\qquad |\widetilde{S}_{\mathrm{ij}}| = \sqrt{2\;\widetilde{S}_{\mathrm{ij}}\;\widetilde{S}_{\mathrm{ij}}}\,. \tag{3.26}$$

Note that gravitational force is neglected in the current study. In the above equation, C_{s} represents the Smagorinsky coefficient and is approximated as 0.162 in the current study. Also, Δ_m stands for the filter width, (the cube root of the minimum cell volume) which is calculated as 1.5×10^{-5} m.

Subgrid scale transport

The unresolved subgrid transport of the species and enthalpy are modeled as follows,

$$\sigma_{w_k}^{\mathrm{sgs}} = -\frac{\bar{\rho}\;\nu_{\mathrm{sgs}}}{Sc_{\mathrm{sgs}}}\;\frac{\partial \widetilde{w}_k}{\partial x_j}\,, \tag{3.27}$$

$$\sigma_h^{\text{sgs}} = -\frac{\bar{\rho}\,\nu_{\text{sgs}}}{Pr_{\text{sgs}}}\,\frac{\partial \widetilde{h}}{\partial x_j}\,, \tag{3.28}$$

where Pr_{sgs} and Sc_{sgs} represent the Prandtl and Schmidt numbers for the subgrid scales, respectively, which are considered as 1, in the present study.

3.4 TURBULENT KINETIC ENERGY (TKE)

As already discussed in Section 3.2, in a turbulent flow, energy is transferred from the mean flow to the larger scale motions and thus from these motions to the fine structures, until friction dissipates the kinetic energy into heat (Pope 2000). Therefore, in the context of the micro-mixing within the JSRs, the values of the turbulent kinetic energy and its dissipation rate are of great importance. The total specific turbulent kinetic energy K_{tot} in the LES approach consists of the specific turbulent kinetic energy in the resolved scales K_{res}, and the sub-grid scales K_{sgs} as follows (Pope 2000),

$$K_{\text{tot}} = K_{\text{res}} + K_{\text{sgs}}\,. \tag{3.29}$$

The specific turbulent kinetic energy of subgrids scales can be calculated from the contribution of the SGS turbulence modeling (Smagorinsky model) using,

$$K_{\text{sgs}} = \frac{\nu_{\text{sgs}}^2}{(C_{\text{s}}\,\Delta_{\text{m}})^2}\,. \tag{3.30}$$

Moreover, the resolved specific turbulent kinetic energy is given by (Pope 2000),

$$K_{\text{res}} = \frac{1}{2}\widetilde{u_i'' u_i''}\,. \tag{3.31}$$

It is important to mention that the resolved TKE of the integral length contains 80% of the total turbulent kinetic energy in the LES simulations (Pope 2000).

3.5 TURBULENCE DISSIPATION RATE

Various methods have been used to estimate the dissipation rate of the TKE, such as turbulence power spectrum turbulent (Sheng *et al.* 2000), kinetic energy balance (Hussein and Martinuzzi 1996), Taylor's frozen turbulence hypothesis (Hinze 1994), large eddy Particle Image Velocimetry (PIV) (Sheng *et al.* 2000), dimensional analysis

(Kresta and Wood 1993), and based on the DNS methods (Andreopoulos and Honkan 1996). Since the DNS calculations are expensive to compute and to conduct experimentally, the large eddy PIV approach would be an appropriate way to evaluate the dissipation rate in a stirred tank (Sheng *et al.* 2000). Sheng *et al.* (2000) concluded that whereas large scale motions in turbulent regimes are responsible for absorbing energy from mean flow, successively smaller scale motions tend to dissipate the energy provided by larger scale structures.

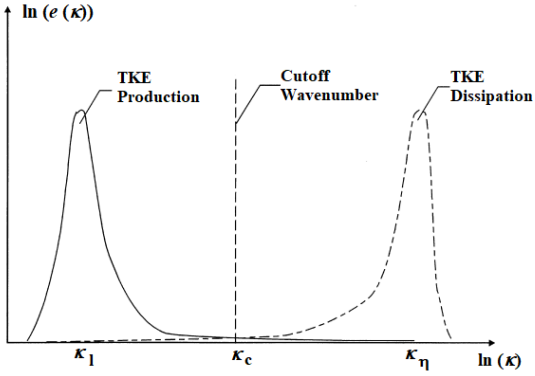

Figure 3.2: Production of TKE by the large scale structures (integral length scales) and dissipation of TKE by the small scale structures (Kolmogorov length scales)(Sheng *et al.* 2000)

Figure 3.2 shows the production and dissipation of the TKE over different wavelengths of turbulent structures (Sheng *et al.* 2000). As can be seen, a maximum value of the TKE is generated in the range of the wavelength of κ_1 and the same amount of the generated energy is dissipated by the Kolmogorov scales in the range of the wavelength of κ_η. Furthermore, in between, over the inertial subrange region or close to the cutoff wavelength, TKE is neither generated nor dissipated. According to Ref. (Wang *et al.* 2021), the dissipation rate of the small grid scale contains at least 70% of the total dissipation in the Smagorinsky model. Therefore, the total turbulence dissipation rate of the TKE in the current study using the LES

approach is approximated by the turbulence dissipation rate of the SGS as (Zhang *et al.* 2020, Jaworski and Murasiewicz 2010),

$$\varepsilon \approx \varepsilon_{\text{sgs}} = C_\epsilon \, \frac{K_{\text{sgs}}^{3/2}}{\Delta_m} \,, \tag{3.32}$$

where the model constant of C_ϵ is considered as 1.04 in this study.

3.6 THERMOPHYSICAL MODELING

Thermophysical models in OpenFOAM are related to the physical properties of fluid, energy, and heat (Weller *et al.* 1998). Furthermore, the computation of these thermophysical properties is based on a pressure-temperature system. In this study, the *hePsiThermo* model (Weller *et al.* 1998) is considered, which calculates general thermophysical properties based on the enthalpy and compressibility of $\psi = (R_0 \; T)^{-1}$ (Makhija and Giri 2021).

In the current study, the dynamic viscosity of the pure gas follows the Sutherland's law using (Sutherland 1893),

$$\mu = \frac{A_{su}\sqrt{T}}{1 + \dfrac{T_s}{T}} \,, \tag{3.33}$$

where A_{su} and T_s are the Sutherland constants. Since a mixture of N_2 and CO_2 is considered for the non-reacting case and the oxidation of dimethyl ether for the reacting case, the dynamic viscosity of the mixture is calculated in the present simulations. The dynamic viscosity for a mixture μ_{mix} consisting of different species is obtained by the following expression (Cengel 2003),

$$\mu_{\text{mix}} = \sum_{k=1}^{n_s} w_k \; \mu_k \,. \tag{3.34}$$

In the current study, the model of perfect gas is chosen to calculate the density of gas flow as $\rho = p/R_0 \; T$. Therefore, in order to calculate thermo and physical properties of the ideal gases, the existing JANAF table is needed (Stull and Prophet 1971). An example, the specific heat capacity of c_p is calculated as follows,

$$c_p(T) = R_0 \; (a_0 + a_1 T + a_2 T^2 + a_3 T^3 + a_4 T^4) \,, \tag{3.35}$$

where a_0, a_1, a_2, a_3, and a_4 are constants which can be found in JANAF polynomials in Ref. (Stull and Prophet 1971). Moreover, the specific heat capacity for a mixture is calculated as,

$$c_{p,\mathrm{mix}} = \sum_{k=1}^{n_s} w_\mathrm{k}\, c_{p,\mathrm{k}}\,. \tag{3.36}$$

According to Cengel (2003), the internal energy of a system consists of sensible, latent, chemical and nuclear forms. In the current study, sensible enthalpy, which is the energy required to heat/cool the system from a reference temperature, is considered.

It should be noted that Eqs. 3.35-3.36 are also used in the HOMogeneous REAction (HOMREA) for calculation of thermophysical properties.

4 MULTI-ZONE MODEL

To numerically predict species concentration and temperature in a perfectly mixed reactor at steady state conditions, the model of Perfectly Stirred Reactor (PSR) is commonly used. However, the assumption of an ideal PSR model may not be valid in reality for the non-ideal JSRs due to the instabilities that exist in closed systems (Abdalla *et al.* 1982, Patel *et al.* 2010, Lammersen *et al.* 2013, Stoehr *et al.* 2015). Therefore, in order to identify the origin of the inhomogeneity, a zero-dimensional mathematical model is developed. In the developed multi-zone model, the JSR is divided into a number of separate homogeneous PSR where all scalar fields are uniform in each zone. However, the initial mole fraction of the reactants, the volume, the wall temperature, and the heat transfer coefficient in each zone can be considered differently. In addition, the mass and energy exchange between all zones in the developed multi-zone model is considered, while keeping the volume of the zones constant over time. Due to the inhomogeneous distribution of the turbulence parameters, such as turbulent kinetic energy (Abdalla *et al.* 1982), the mixing exchange rate between zones is calculated as a function of turbulence frequency. It is worth mentioning that the variation of the wall temperature, the heat transfer coefficient, the initial mole fraction of the reactants, and volume have been considered in this study as the highest possible deviations predicted by the experimental study in Ref. (Moshammer *et al.* 2016) to mimic the stochastic process inside the JSR.

In this chapter, the governing equations for describing a PSR are first described in Section 4.1 and then the developed theoretical multi-zone model is formulated in Sections 4.2 - 4.4.

4.1 GOVERNING EQUATIONS IN THE PERFECTLY STIRRED REACTOR

An idealized stirred reactor is a small chamber with inlet and exit ducts while keeping the condition of thermal insulation. Figure 4.1 shows a schematic of a PSR in which fuel and oxidizers are delivered continuously from the inlet in such a way that high-intensity turbu-

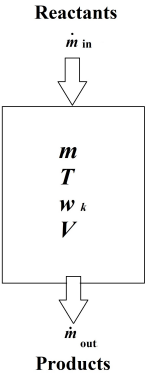

Figure 4.1: Schematic of a PSR model

lent mixing makes the reactor's properties spatially uniform. Therefore, chemical reaction rates, rather than mixing procedures, govern how quickly reactants turn into products. Note that the walls of the well stirred reactors are considered to be non-catalytic. The model of PSR is generally used for predicting the behavior of the well-stirred reactors, developing and validating the chemical kinetic mechanism (Lu and Law 2006), analyzing the system performance, including species concentrations, reaction rates, and ignition delay times (Wagnon *et al.* 2018), studying lean premixed combustion in gas turbine reactor (Dagaut *et al.* 2005), soot particle formation modeling (Marchal *et al.* 2009, Brown *et al.* 1998).

A set of conservation equations govern the different processes taking place in the well-stirred reactors. The PSR model is described by the following conservation of mass, species mass fraction, and energy equations (Glarborg *et al.* 1986) considering a constant pressure system (p = constant), negligible kinetic and potential energies ($KE = 0$, $PE = 0$),

$$\frac{dm}{dt} = \dot{m}_{in} - |\dot{m}_{out}|\,, \tag{4.1}$$

$$\dot{Q}_h + \dot{W}_h + h_{in}\ \dot{m}_{in} - h_{out}\ |\dot{m}_{out}| = \frac{dm \cdot U}{dt}\,, \tag{4.2}$$

$$\frac{dw_k}{dt} = \frac{\dot{m}_{in}}{m}(w_{in,k} - w_k) + \frac{M_k\ \dot{\omega}_k}{\rho_i}\,, \tag{4.3}$$

where mass inflow rate, mass outflow rate, rate of heat transfer, rate of work, specific internal energy, specific enthalpy, species mass fraction, molecular weight, and molar production rate of the kth species are denoted by $\dot{m}_{in}$, $\dot{m}_{out}$, $\dot{Q}_h$, $\dot{W}_h$, U, h, w, M, and $\dot{\omega}$, respectively.

4.2 GOVERNING EQUATIONS IN THE MULTI-ZONE MODEL

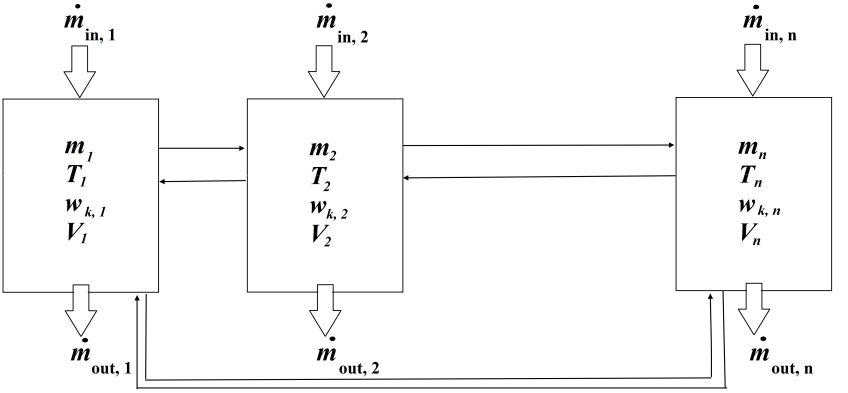

Figure 4.2: Schematic of a multi-zone model

Figure 4.2 depicts a schematic of the multi-zone model, in which the mass inflow ($\dot{m}_{\mathbf{in}}$) and the mass outflow rates ($\dot{m}_{\mathbf{out}}$) is defined separately in each zone. Furthermore, the arrows between the zones represent the mixing exchange rates. In this model, the sum of the mass inflow rates over all zones equals the total mass inflow rate of the reactor. The multi-zone model is later implemented in the in-house simulation program of HOMREA (Maas and Warnatz 1988). This software package is commonly used for computing time-dependent homogeneous reaction systems under various thermodynamics variables such as constant or user-specified time-dependent profiles of pressure, volume, temperature or adiabatic conditions. To effectively simulate the flow field within a JSR and simultaneously solve the governing equations for all zones in the multi-zone model, it is necessary to make certain simplifications. These simplifications aim to replicate the actual conditions inside the JSR and capture the available nonhomogeneity following the experimental

setup of the JSR (Moshammer *et al.* 2016). The following assumptions are considered in the multi-zone model.

- The total volume of the JSR (the volume of the confined spherical chamber) is kept constant over time because the JSR configuration has no moving parts. Subsequently, the volume of each zone is assumed to be constant over time. Therefore, no work exchange is included in this model. If the volume of each zone is allowed to vary over time, the hottest zone will expand to fill the entire JSR chamber, eliminating the cooler zones, which is not realistic.
- The sum of the volumes over all zones is equal to the total volume.
- Surface reactions are neglected.
- The pressure over all zones is constant over time and equal to the initial pressure value. Following the experimental setup of the JSR (Moshammer *et al.* 2015), exhaust gas is continuously removed by the outlet to keep the pressure constant.
- In the current study, only the heat transfer of the reactor side is considered, not the heat transfer of the oven side and the reactor wall (Lignola and Reverchon 1988). The reason for this simplification is related to the computational domain, which is limited to the reactor side in order to reduce computational costs and to focus only on the behavior of the flow within the reactor chamber.
- Radiation heat transfer and heat conduction between the zones are not considered in the studied model.

The differential algebraic system of mass, species mass fraction, and energy conservation equations for the zone i are implemented in the HOMREA as following,

$$\frac{dm_i}{dt} = \dot{m}_{in,i} + \sum_{j=1}^{n_z} \dot{m}_{i,j}^{+} + \sum_{j=1}^{n_z} \dot{m}_{i,j}^{-} + \dot{m}_{out,i}\,, \tag{4.4}$$

$$\frac{dw_{i,k}}{dt} = \dot{X}_{in,i}(w_{in,i,k} - w_{i,k}) + \sum_{j=1}^{n_z} \dot{X}_{i,j}^{+}\,(w_{j,k} - w_{i,k}) + \frac{M_{i,k}\,\dot{\omega}_{i,k}}{\rho_i}\,, \tag{4.5}$$

$$\frac{dT_i}{dt} = \frac{1}{c_{p,i}}\Bigg\{ -\frac{h_t\ A\ (T_\mathrm{w} - T_i)}{m_i} + \frac{p}{\bar{M}_i \rho_i}\frac{d\bar{M}_i}{dt} - \frac{1}{\rho_i}\sum_{k=1}^{n_\mathrm{s}} (M_{i,k}\ U_{i,k}\ \dot{\omega}_{i,k}) + \dot{X}_{in,i}\sum_{k=1}^{n_\mathrm{s}} (h_{in,i,k} - h_{i,k})\ w_{in,i,k} + \dot{X}_{in,i}\sum_{k=1}^{n_\mathrm{s}} (h_{i,k} - U_{i,k})\ (w_{in,i,k} - w_{i,k}) + \sum_{j=1}^{n_\mathrm{z}} \dot{X}^{+}_{i,j}\sum_{k=1}^{n_\mathrm{s}} (h_{j,k} - h_{i,k})\ w_{j,k} + \sum_{j=1}^{n_\mathrm{z}} \dot{X}^{+}_{i,j}\sum_{k=1}^{n_\mathrm{s}} (h_{i,k} - U_{i,k})\ (w_{j,k} - w_{i,k})\Bigg\}, \tag{4.6}$$

together with the equations of molar mass variation and mass variation induced by ideal gas (in constant volume and pressure) as follows,

$$\frac{d\bar{M}_i}{dt} = -\bar{M}_i^2 \sum_{k=1}^{n_\mathrm{s}} \frac{1}{M_{i,k}}\frac{dw_{i,k}}{dt}, \tag{4.7}$$

$$\frac{dm_i}{dt} = -\frac{m_i}{T_i}\frac{dT_i}{dt} + \frac{m_i}{\bar{M}_i}\frac{d\bar{M}_i}{dt}. \tag{4.8}$$

Here, the total number of zones, the total number of species, convective heat transfer coefficient, surface area between the gas mixture and the zone's wall, wall temperature, mean molecular weight, and specific heat capacity at constant pressure are denoted by n_z, n_s, h_t, A, T_w, $\bar{M}$, and c_p, respectively.

The mass exchange rate of $\dot{m}^{+}_{i,j}$ represents the mass flow rate obtained by the zone i from zone j and $\dot{m}^{-}_{i,j}$ the mass flow rate given by the zone i to the zone j. Since the highly turbulent, chaotic, and unpredictable fluid motions promote the transport of mass and heat transfer within the JSR, the exchange of mass and energy between two zones is considered equally in the multi-zone model. That means the mass flow rate obtained by the zone i from the zone j and given by the zone i to the zone j has the same value. Therefore, the sum of these pair variables is zero. Details are provided in Section 4.3.

Furthermore, the first term of the right-hand side (RHS) of Eq. 4.5 represents the exchange due to the difference between the mass fraction of the inflow gas and the flow inside the chamber; the second term refers to the exchange between the zones since species mass fraction in each zone may be different. The last term also represents

the chemical reaction source term. In addition, in Eq. 4.6, the first term of the RHS stands for the convective heat transfer to/from the walls, the second term for the variation of molecular weight; the third term for the source term of heat generation during chemical reactions; the fourth and the fifth terms for exchange between the inflow gas and the flow inside the reactor due to differences in enthalpy and species mass fraction; and finally the sixth and the seventh terms for the exchange between the zones due to difference in enthalpy and mass fraction. It should be noted that the developed multi-zone model can be considered as a single zone model if the terms related to the interaction between the zone are removed from the Eqs. 4.4 - 4.6.

In Eqs. 4.5 and 4.6, the mass fraction of the inflow rate $\dot{X}_{\text{in}}$ and the mass exchange fraction between zones $\dot{X}^{+}_{\text{i,j}}$ are specified as,

$$\dot{X}_{in,i} = \frac{\dot{m}_{in,i}}{m_i}, \qquad \dot{X}^{+}_{i,j} = \frac{\dot{m}^{+}_{i,j}}{m_i}\,. \tag{4.9}$$

Note that the mass of each zone is calculated by the ideal gas law, since temperature, pressure, mole fraction of the reactants, and volume of each zone are defined as the input values. In this study, the values of temperature, pressure, initial species mass fraction of the reactants, and the total volume of the reactor are given by the experimental data (Moshammer *et al.* 2016) and the turbulence parameters are obtained by the LES simulations of the JSR (Esmaeelzade *et al.* 2021). Furthermore, the mass variation for each zone in the multi-zone model is calculated using the partial derivatives of the ideal gas law with respect to time (Eq. 4.8), while the system pressure and the volume of each zone are kept constant. Thus, having the mass variation from Eq. 4.8, the outflow rate for each zone ($\dot{m}_{out}$) can be calculated by the conservation of mass equation (Eq. 4.4).

4.3 MODELING MASS EXCHANGE RATES

In the present study, the mass obtained/given by a zone (mass exchange) is proportional to 1) the zone's mass given/obtained by a zone $\boldsymbol{m}$; 2) mass coming from/given to a zone is distributed to the different zones according to their mass ratios represented by $\boldsymbol{\zeta}\ \boldsymbol{\zeta}^T$; 3) mixing frequency of $\boldsymbol{f_{mix}}$ which is affected by turbulent time-scales. Note that multiplying the mass weighted vector $\boldsymbol{\zeta}$ by its transpose $\boldsymbol{\zeta}^T$ produces a matrix which each element is the product of the corresponding mass of each zone. The model of mass

exchange rate obtained by a zone $\dot{\boldsymbol{\Omega}}_{\boldsymbol{m}}^{+}$ and given to a zone $\dot{\boldsymbol{\Omega}}_{\boldsymbol{m}}^{-}$ in matrix notation can be obtained by,

$$\dot{\boldsymbol{\Omega}}_{\boldsymbol{m}}{}^{+} = \boldsymbol{\zeta}\,\boldsymbol{\zeta}^{T}\,\boldsymbol{m}\,\boldsymbol{f}_{\boldsymbol{mix}}, \quad \dot{\boldsymbol{\Omega}}_{\boldsymbol{m}}{}^{-} = -\boldsymbol{\zeta}\,\boldsymbol{\zeta}^{T}\,\boldsymbol{m}\,\boldsymbol{f}_{\boldsymbol{mix}}\,. \tag{4.10}$$

Specifically, we defined the mass exchange rates of $\dot{m}_{i,j}^{+}$ (the mass flow rate obtained by the zone i from zone j) and $\dot{m}_{i,j}^{-}$ (the mass flow rate given by the zone i to the zone j) in index notation as,

$$\dot{m}_{i,j}^{+} = \zeta_j\,\zeta_i\,m_j\,f_{mix,j}\,, \tag{4.11}$$

$$\dot{m}_{i,j}^{-} = -\zeta_i\,\zeta_j\,m_j\,f_{mix,j}\,, \tag{4.12}$$

where the mass weighted variable of ζ is calculated as,

$$\zeta_i = \frac{m_i}{\sum_{i=1}^{n_z} m_i}\,. \tag{4.13}$$

It is noteworthy that the net mass exchange between any two zones (sum of the mass obtained and given by a zone) is equal to zero, as described in Eq. 4.10. Due to the intense mixing and the fast motion of the flow field inside the JSR, the absolute value of the mass exchange between any two zones is assumed to be identical ($|\dot{\Omega}_{m}^{+}| = |\dot{\Omega}_{m}^{-}|$). However, the overall mass within an individual zone does not remain constant over time due to the presence of mass inflow and outflow rates. The inflow and outflow contribute to changes in the mass content within the zone, leading to temporal variations in the mass of the zone despite the balanced mass exchange between zones. Also, in this study, the mass exchange rate is defined only between different zones, not from zone i to the zone i.

Following the mixing models in Refs. (Pope 1985, Celis and da Silva 2015, Subramaniam and Pope 1998), the mean mixing frequency f_{mix} is defined as a function of mixing model parameter of C_ϕ and turbulent frequency of each zone f as follows,

$$f_{\text{mix},i} = C_{\phi,i}\,f_i\,. \tag{4.14}$$

The model parameter obtains a wide range of values depending on the mixing model (Krisman *et al.* 2014). As mentioned in Ref. (Celis and da Silva 2015), C_ϕ varies with the characteristic length scales of the scalar fields; therefore is not a universal constant. In the current study, the sensitivity of the multi-zone model to a wide range for the model parameter is examined and the best value of 0.18 is selected for further investigation.

As mentioned in Sections 3.4 and 3.5, high Reynolds number turbulent flow comprise a range of eddies with different sizes (Pope 2000). Within turbulent flows, turbulent kinetic energy is generated by the interaction between the larger eddies and the mean flow. On the other hand, the dissipation of the kinetic energy into heat occurs within the smallest eddies (Sheng *et al.* 2000). Hence, the turbulent kinetic energy and dissipation rates serve as key parameters for characterizing mixing processes. The turbulent frequency $\boldsymbol{f}$ is defined in this study as follows (Celis and da Silva 2015, Magnussen 2005),

$$\boldsymbol{f} = \varepsilon_{\mathbf{tot}} / \boldsymbol{K}_{\mathbf{tot}}\,, \tag{4.15}$$

where the total turbulent kinetic energy and its dissipation rate are denoted by $\boldsymbol{K}_{\mathbf{tot}}$ and $\varepsilon_{\mathbf{tot}}$, respectively. As mentioned in Section 3.5, the total dissipation rate can be approximated by SGS dissipation rate. In the current study, the mixing frequency is specified as an input parameter from the CFD studies (Esmaeelzade *et al.* 2021) for the developed zero-dimensional multi-zone model. Chen (1997) studied the influence of unmixedness in terms of residence time and mixing frequency scale using the Probability Density Function (PDF) equations for a Partially Stirred Reactor (PaSR). However, the developed model in this study provides a simpler deterministic model to reflect the inhomogeneity of the JSRs.

4.4 MODELING HEAT TRANSFER COEFFICIENT

According to David *et al.* (1979) and Lignola and Reverchon (1988), the heat transfer coefficient in the JSRs depends on the fluid dynamic of the gas mixture. Later, the variation of the heat transfer function in predicting the oscillation frequency during the oxidation of dimethyl ether (DME) is investigated (Stoehr *et al.* 2015). An empirical correlation for the heat transfer of a cylindrical JSR is derived by David *et al.* (1979). In this study, this correlation is adapted to represent heat transfer between the zone and its wall for a spherical JSR. The heat transfer coefficient, denoted as h_t, is derived based on the Nusselt number, as described by Lignola and Reverchon (1988),

$$h_t = 0.89\,\frac{\lambda}{D}\,Re_{\mathrm{N}}^{0.683}\,Pr^{1/3}\,, \tag{4.16}$$

in which the Prandtl number follows the formula $Pr = \mu\ c_p/\lambda$ and the Reynolds number based on the nozzle conditions $Re_N = \rho\ Q/\pi\ d\ \mu$.

In this study, the heat transfer coefficient for a spherical JSR of 40 mm having four inclined nozzles of diameter of 1 mm based on the Computational Fluid Dynamic (CFD) results is calculated, in which the Reynolds number is based on an averaged velocity and the nozzle diameter, and Prandtl number is based on viscous and thermal diffusion rate of the mixture.Therefore, in the current study, the heat transfer coefficient is computed as $3.28\,\mathrm{W\,m^{-2}\,K^{-1}}$.

Part III

RESULTS

To understand the mixing quality in a spherical JSR designed by Dagaut *et al.* (1986), the details of flow field characteristics, turbulence structures, homogeneity, production of turbulent kinetic energy and its dissipation, etc., are numerically analyzed in the present study. In the first part, a three-dimensional configuration of a JSR is simulated for a non-reacting mixture by the LES turbulent flow model in order to evaluate the mixing process.

Chapter 5 presents the numerical setup of the JSR together with the operating initial and boundary conditions, which were adjusted to the experimental work (tracer decay experiments) of Ayass *et al.* (2016). Subsequently, the mixing performance of a spherical JSR in terms of the mean residence time distribution is analyzed in Chapter 6. Adding the modeling of the turbulent nozzles to the computational domain improves the results, which is discussed in Chapter 7. Later, the effects of different geometrical and thermodynamic parameters on the mixing quality of the JSR are studied in Chapter 8.

The results of the mixing process in Chapters 6-8 show the necessity of a theoretical model to incorporate imperfect mixing with detailed chemistry in the real JSRs. Therefore, in the second part, a theoretical model is developed to capture the inhomogeneous distribution of the species mole fractions and the thermodynamic variables in a reacting composition, as addressed in Chapter 9.

Later, the mixing quality inside a spherical JSR is improved by proposing an alternative design of the nozzles. Chapter 10 discusses the details of the turbulence structure and its effect on the mixing efficiency within the new design of the JSR. Finally, the outcomes of this thesis together with some suggestions for future work are presented in Chapter 11.

5 NUMERICAL SETUP OF A SPHERICAL JSR

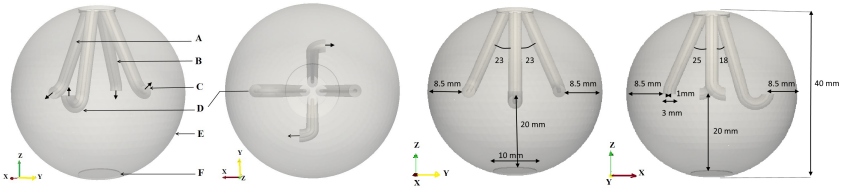

Figure 5.1: The Jet Stirred Reactor (JSR) configuration in three dimensions; nozzle D points in the upward direction, length of 27.1 mm, its orientation from the y-z plane of 18°; nozzle B points in the downward direction, length of 22.8 mm, its orientation from the y-z plane of 25°; nozzles C and A point in the horizontal direction, length of 21.4 mm, their orientations from the x-z plane of 23°; spherical chamber E; outlet F (Esmaeelzade *et al.* 2021)

Figure 5.1 shows different views of a three-dimensional configuration of a spherical JSR following the design of Dagaut *et al.* (1986). The reactor consists of a spherical vessel with a total volume of 32.8 cm^3 and a diameter of 40 mm together with four nozzles (with an outer diameter of 3 mm and an inner diameter of 1 mm), and an outlet of the diameter of 10 mm. The inclinations of the nozzles to the z-axis and their distances to the outlet and to the walls are described in the captions of Fig. 5.1. Positioning four turbulent nozzles in the equatorial plane leads to the generation of two circulating streams in the x-y and the x-z planes. Therefore, to understand how far the studied JSR is from the ideal and homogeneous conditions, the mixing quality inside a spherical JSR is numerically investigated using the Open Source Field Operation and Manipulation (OpenFOAM) software.

5.1 SIMULATION SETUP IN OPENFOAM

The flow field inside the JSR is simulated by the solver of *reactingFoam*. The filtered governing equations of Eqs. 3.17-3.20 are solved

in this solver. The simulations follow a tracer-decay technique using carbon dioxide and nitrogen according to the experimental setup (Ayass *et al.* 2016). Note that the study choice of a mixture of two nonreacting species of carbon dioxide and nitrogen allows to focus on the mixing quality without considering the reactions between the species. Therefore, the source terms of Eqs. 3.19 and 3.20 are neglected for all simulations in this study performed by OpenFOAM. According to the experiments (Ayass *et al.* 2016), a continuous stream of CO_2 gas is first injected into the JSR until the flow reaches the steady state condition. Then, a solenoid valve suddenly blocks CO_2 and a constant N_2 stream hits the JSR walls by turbulent jets. The turbulent jets exiting from the nozzles in four different directions facilitate effective mixing of the flow. Finally, the flow leaves the reactor through the outlet.

In this study, a 3-D configuration of the JSR is numerically analyzed considering constant volumetric flow rates of $18.9\,\mathrm{cm^3\,s^{-1}}$, $84.6\,\mathrm{cm^3\,s^{-1}}$, and $162.2\,\mathrm{cm^3\,s^{-1}}$ depending on the desired mean residence time. The numerical calculation of the mean residence time based on the computed concentration at the outlet is also addressed in Section 2.3.

Boundary	Temperature	Pressure
jets inlets	*fixedValue* of 298 K	*fixedFluxPressure* of 100 kPa
outlet	*zeroGradient*	*totalPressure*
spherical vessel	*fixedValue* of 298 K	*zeroGradient*

velocity	mass fraction $t < 1\,\mathrm{s}$	mass fraction $t > 1\,\mathrm{s}$
fixedValue of $\lvert u_z \rvert = 26.96\,\mathrm{m\,s^{-1}}$	*fixedValue* of $CO_2 = 1$; $N_2 = 0$	*fixedValue* of $CO_2 = 0$; $N_2 = 1$
zeroGradient	*zeroGradient*	*zeroGradient*
noSlip	*zeroGradient*	*zeroGradient*

Table 5.1: Boundary conditions for the standard JSR over the jets inlets, outlet and the spherical vessel in the case of $Q = 84.6\,\mathrm{cm^3\,s^{-1}}$

The initial and the boundary conditions for the simulations follow the experimental setup (Ayass *et al.* 2016). Herein, an ambient temperature of 298 K, pressure of 100 kPa, and velocity of $0\,\mathrm{m\,s^{-1}}$ were set as the internal field. The boundary conditions are sum-

marized in Table 5.1. The *zeroGradient* condition represents that the boundary face value is set to the value of its owner cell ($\frac{\partial \phi}{\partial n} = 0$) (Weller *et al.* 1998). However, the *noSlip* fixes a zero velocity at the surface of the spherical chamber of the JSR. Over the *fixedValue*, the variable's value is kept fixed. The *fixedFluxPressure* on the jet inlets chooses the pressure gradient such that it agrees with the velocity boundary condition. Furthermore, the *totalPressure* boundary condition at the outlet of the spherical JSR is considered. The total pressure (also known as stagnation pressure) and static pressure are connected by $p_{\text{static}} = p_{\text{tot}} - \frac{\rho \boldsymbol{u}^2}{2}$ (Boite *et al.* 2023). This boundary condition allows the static pressure to vary freely on the surface according to the velocity vector. Therefore, it improves the numerical stability of the solution. Moreover, regarding the mass fraction of carbon dioxide, a constant value of 1 is first considered inside the reactor and at the inlets and in the same way, a constant value of nitrogen is defined as zero at all inlets, as outlined in Table 5.1. After running the simulations for 1 s, which is 660 times the ratio of the JSR diameter to the injection velocity, the flow of CO_2 gas is stopped, following the procedure described in the experimental setup by Ayass *et al.* (2016) for filling the JSR. Therefore, a stationary steady-state condition is reached before the injection of N_2 into the reactor. Subsequently, the boundary conditions at the inlets of the jets were modified such that the CO_2 mass fraction became 0, while the N_2 gas was set to 1.

It should be noted that the flow inside the nozzle is first neglected and a top-hat velocity profile is considered at the exit of the nozzles in order to focus only on the decay of the tracer within the spherical chamber and to simplify the calculations (as discussed in Chapter 6). Next, the flow modeling through the nozzles is added to the computational domain and a top-hat velocity profile is considered at the entrance of the nozzles (as presented in Chapter 7). Note that the calculated Reynolds number based on an averaged injection velocity of 26.9 m s^{-1}, a nozzle diameter of 1 mm, and a reactor diameter of 40 mm, the Reynolds number (for CO_2 flow) is 2620 and 10400, respectively.

6

CALCULATION OF NON-REACTING FLOW (NOZZLE FLOW MODELING NEGLECTED)

In this chapter, the modeling of the flow through the nozzles is neglected and the injection of the flow stream at the outlet of the nozzles is considered (boundary conditions were set on the nozzles outlet). Due to these simplifications, fewer cells are generated over the JSR, resulting in lower computational cost.

The details of the generated mesh was presented in Section 6.1. Furthermore, a grid resolution study on three different cells was used to understand the accuracy of the numerical simulations. Afterwards, the results of the flow field characteristics in terms of the decaying process of the tracer and velocity distribution were discussed in Section 6.2. Further, the mean residence time for different constant volumetric flow rates was studied in Section 6.3. The results of the current chapter have been compared with an ideal JSR and the experimental data presented by Ayass *et al.* (2016).

6.1 OVERVIEW ON THE GENERATED MESH

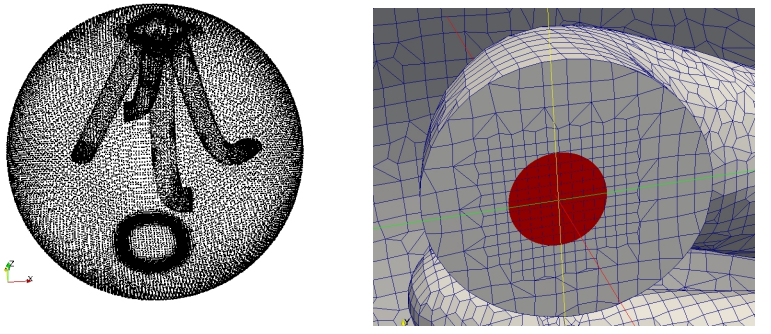

(a) (b)

Figure 6.1: Generated mesh over (a) the internal field (b) the exit of the nozzle (Esmaeelzade *et al.* 2019)

Figures 6.1a and 6.1b show the generated meshes inside the JSR configuration and close to the exit of one nozzle, respectively. Since a high velocity stream is injected from the nozzles, smaller meshes are distributed in the regions that are close to the exits of the nozzles. The mesh structure consists mainly of hexahedral and polyhedral grids which are distributed non-uniformly within the JSR by the mesh generator of the *SnappyHexMesh* utility (OpenFOAM). The mesh refinement is also applied at the walls and the outlet. These regions have a higher rate of change of the flow properties, such as velocity, pressure, and species concentration.

The meshing process is followed by drawing the JSR in SALOME platform (Ribes and Caremoli 2007). Then, the STereoLithography (STL) format of the drawing is imported into OpenFOAM. After that, a rectangular box covering the entire geometry with a background mesh is created by *blockMesh*. Thus, the *snappyHexMeshDict* executes the control of the meshing, such as splitting all cells intersected by STL geometries, cell refinement, splitting cells at edges and surfaces, and adding layers. The mesh is finally projected back from the surface in the direction normal to the surface by a specified thickness (Gisen 2014).

Cells	50k	130k	260k
$(CO_2)_{rms}$	0.034	0.033	0.032

Table 6.1: Study of grid resolution in terms of the root mean square of the tracer mass fraction

In order to understand the accuracy of the numerical results, the grid refinement study is performed on progressively increased mesh size. To this end, the JSR is distributed into increasing mesh sizes of 50k, 130k and 260k cells. The Root Mean Square (RMS) of the CO_2 mas fraction is calculated and given in Table 6.1. As can be concluded from Table 6.1, the RMS of the CO_2 mas fractions are very close to each other by increment of the cell size. Therefore, the mesh size of 130k was used for further analyses in this chapter to reduce the computational efforts. Note that the previous CFD simulation of the same spherical JSR using the RANS modeling, was performed on 70k cells (Gil and Mocek 2012).

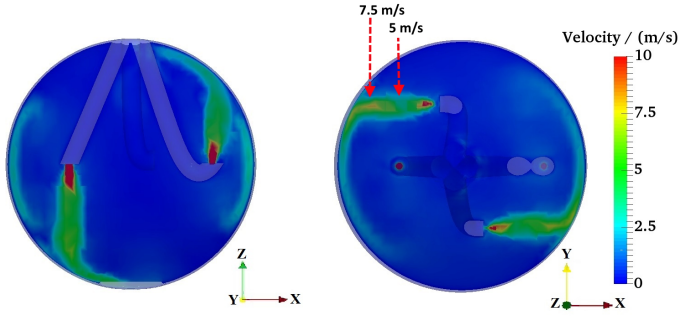

(a) (b)

Figure 6.2: Time averaged distribution of the velocity at the cross section of (a) the x-z plane and (b) the x-y plane considering a volumetric flow rate of $Q = 84.6\,\mathrm{cm^3\,s^{-1}}$

6.2 RESULTS OF FLOW PROPERTIES WITHIN THE JSR

The interactions of the turbulent jets originating from the nozzles are of great interest in studying the mixing process within the JSR. Figure 6.2 shows the time-averaged magnitude of the velocity field in the cross-sections of the x-z and the x-y axes. The average is calculated over the time instances where the flow is statistically stationary and the injection of nitrogen has not yet started inside the JSR. As can be concluded from Fig. 6.2a, the flow issued by the nozzles pointing upwards and downwards hits the front wall; then bends counter-clockwise in the plane of the x-z. While at the same time, a pair of horizontally oriented nozzles drive the flow circumstantially in the x-y plane in the counter-clockwise direction, as illustrated in Fig. 6.2b. Therefore, a continuous perpendicular flow generated by two pairs of nozzles (i.e., the upwards and downwards pointing nozzles and the horizontal pointing nozzles) enhances the turbulence level and the efficient mixing through the JSR.

In this section, a top-hat velocity profile with a uniform velocity distribution of $26.96\,\mathrm{m\,s^{-1}}$ is set at the outlet of the nozzles (over the entire cross-sectional area of the nozzle). The top-hat velocity over the nozzle exit is not clear, because the color map is restricted to the range of 0 - $10\,\mathrm{m\,s^{-1}}$ for a better visualization of the velocity distribution within the reactor.

Further, the flow velocity decreases by $5\,\mathrm{m\,s^{-1}}$ by being far away from the orifice nozzle. However, where the flow stream meets the surface of the spherical wall, the flow velocity magnitude increases to about $7.5\,\mathrm{m\,s^{-1}}$ (see Fig. 6.2b).

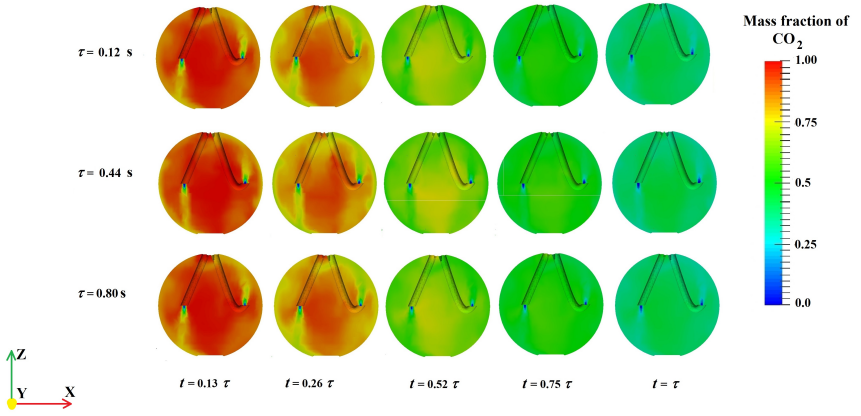

Figure 6.3: Instantaneous snapshots of the tracer mass fraction over time related to a volumetric flow rate of $Q = 162.2\,\mathrm{cm^3\,s^{-1}}$ (first row), $Q = 84.6\,\mathrm{cm^3\,s^{-1}}$ (second row) and $Q = 18.9\,\mathrm{cm^3\,s^{-1}}$ (third row) (Esmaeelzade *et al.* 2019)

As mentioned in Section 5.1, the process of evacuating the JSR from CO_2 stream by instantaneous injection of N_2 stream is simulated using the Large Eddy Simulation (LES) modeling in three cases of volumetric rates of $162.2\,\mathrm{cm^3\,s^{-1}}$, $84.6\,\mathrm{cm^3\,s^{-1}}$ and $18.9\,\mathrm{cm^3\,s^{-1}}$. An overview over the temporal evolution of CO_2 mass fraction after injection of N_2 over the cross section of the x-z axes is shown in Fig. 6.3. From the first to the third row, the volumetric flow rates are decreased and therefore their corresponding mean residence times τ for each case are changed to 0.12 s, 0.44 s, and 0.80 s, respectively. It is important to notice that for all three cases, a considerable non-homogeneous tracer concentration is observed at time instants less than 0.26τ and CO_2 concentration becomes more uniform over time. The results of the LES simulations in the current study are in rather good agreement with the RANS simulations from earlier publications (Crawford 2014), which predict a high inhomogeneity over the spherical JSR at the time of less than 0.2 s.

It should be noted that at the shorter residence time, the inhomogeneity between the inflow gas (N_2) and the existing gas within

the JSR (CO_2) is very high in comparison to the longer residence time. Therefore, the tracer mass fraction changes rapidly between 0.13τ to 0.52τ, compared to the time interval from 0.75τ to τ, as can be seen in Fig. 6.3. More specifically, at the initial time, a stagnation (dead) zone is created in the JSR center and the distance between the nozzles, which leads to the later decay of the tracer, as already predicted by Zhang *et al.* (2018). As time progresses and the residence time increases, the overall mass fraction gradient tends to decrease, leading to a more uniform distribution of the tracer and a slower rate of change of CO_2 mass fraction.

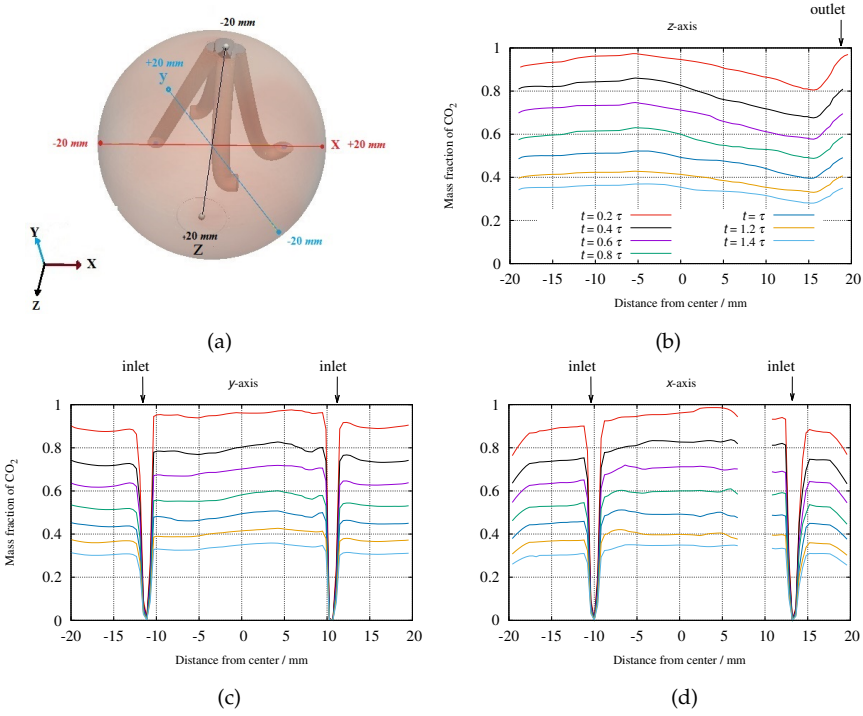

Figure 6.4: Profiles of the mass fraction CO_2 for the case of $Q = 84.6\ \mathrm{cm}^3/\mathrm{s}$ along (b) the z-axis, (c) the y-axis, and (d) the x-axis. The location of the axes is clarified in (a) segment (Esmaeelzade *et al.* 2019)

As shown in Fig. 6.3, a nearly homogeneous distribution of CO_2 mass fraction is obtained at $t{=}\tau$ for all three cases of volumetric flow rates. However, capturing the tracer mass fraction distribution is not enough to evaluate the mixing quality inside the JSR. Therefore, fur-

ther investigations on the mean residence time and the normalized Residence Time Distribution (RTD) are performed.

Figure 6.4 depicts the spatial distribution of CO_2 along three different axes of the z, y, and x as a function of residence time. The positions of the three orthogonal axes are shown in Fig. 6.4a. As shown in Figs. 6.4b - 6.4d, the spatial deviation of CO_2 mass fraction is decreased over time and accordingly homogeneity within the JSR is improved. However, the mixture inside the studied JSR does not achieve complete homogeneity at the mean residence time ($t = \tau$).

Figure 6.4b shows that regions close to the outlet (around $z \approx 15\,\text{mm}$) predict a lower CO_2 mass fraction, while a higher tracer mass fraction is captured at the location of the outlet ($z = 20\,\text{mm}$, where the arrow points) due to the circular flow created by the horizontal nozzles and the flow reversal that occurs as the flow leaves the reactor. Moreover, the CO_2 mass fraction decreases slightly in a region close to the top wall around $z \approx -20\,\text{mm}$ compared to the regions close to center of the JSR ($z = 5\,\text{mm}$) due to the circulating stream generated by the upwards and downwards pointing nozzles (see Fig. 6.4b). In addition, the presence of the horizontal nozzles at $x \approx \pm 10$ mm and the upward and the downward pointing nozzles at $y \approx \pm 10$ mm leads to a drop in the tracer mass fraction to zero due to the injection of fresh N_2 stream, as shown in Figs. 6.4c and 6.4d, respectively. Also, the discontinuity in the profiles of Fig. 6.4d is caused by the nozzle pointing upwards in this area.

6.3 RESULTS OF MEAN RESIDENCE TIME STUDIES

Table 6.2: A representation of the residence times corresponding to an ideal reactor (τ), experimentally measured in Ref. (Ayass *et al.* 2016, Ayass 2013) (τ_{exp}) and predicted by the numerical simulations (τ_{num}) for different flow rates (Q) (Esmaeelzade *et al.* 2019)

Q	τ	τ_{exp}	τ_{num}
$18.9\,\text{cm}^3\,\text{s}^{-1}$	0.70 s	0.725 ± 0.027 s	0.80 s
$84.6\,\text{cm}^3\,\text{s}^{-1}$	0.37 s	0.415 ± 0.011 s	0.44 s
$162.2\,\text{cm}^3\,\text{s}^{-1}$	0.10 s	0.207 ± 0.014 s	0.12 s

In order to understand the mixing performance of the studied JSR and its deviations from idealty, the mean residence time and the normalized RTD are studied, which aid in further improvement of the design of the real reactors. Table 6.2 presents the mean residence time calculated based on the highly resolved LES simulations, the experimental measurement from Ref. (Ayass *et al.* 2016), and the theoretical calculations for an ideal JSR (see Eq. 2.4). Here, the volumetric flow rates change as $18.9\,\mathrm{cm^3\,s^{-1}}$, $84.6\,\mathrm{cm^3\,s^{-1}}$, and $162.2\,\mathrm{cm^3\,s^{-1}}$. Note that the residence time estimated by the LES simulations for a spherical JSR at the operating conditions of 298 K and 1 bar is consistent with the range of 0.01 - 3 s previously estimated by Dagaut *et al.* (1986). Table 6.2 shows that a lower volumetric flow rate predicts a longer mean residence time since it corresponds to a lower velocity and consequently, a lower exchange of the flow within the JSR. Furthermore, the mean residence time predicted by the simulation at the high flow rate of $162.2\,\mathrm{cm^3\,s^{-1}}$ is very close to the theoretical mean residence time, since a higher velocity is defined at the nozzle exit and consequently a faster exchange of flow within the JSR is predicted.

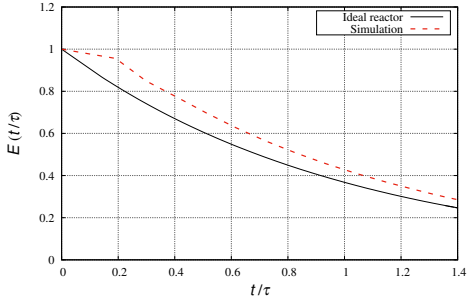

Figure 6.5: Comparing numerically calculated normalized RTD to an ideal reactor (Eq. 2.4) considering volumetric flow rate of $18.9\,\mathrm{cm^3\,s^{-1}}$

Since the mean residence time alone cannot accurately represent the overall level of mixing within the JSR, the residence time distribution (RTD) are generally used to characterize and diagnose the problems in the non-ideal reactors (Fogler 1999), as mentioned in Section 2.3. To characterize the mixing over the simulated JSR, the normalized RTD versus normalized time is calculated for the studied JSR having the volumetric flow rate of $18.9\,\mathrm{cm^3\,s^{-1}}$ and compared to an ideal reactor, as shown in Fig. 6.5. In fact, the normalized RTD ($E(t/\tau)$) for an ideal reactor is calculated based on the

exponential expression $e^{-t/\tau}$, where the theoretical mean residence time is 0.70 s (see Table 6.2). In addition, the numerically predicted $E(t/\tau)$ for the simulated reactor is calculated based on the expression $(C_{out}(t)/C_0)$, using Eqs. 2.6 and 2.9.

As shown in Fig. 6.5, the normalized RTD for the simulated JSR has a unity value at the time of zero since the tracer concentration at the outlet C_{out} is equal to the initial concentration of the tracer C_0. The normalized RTD curve has a large deviation from the ideal reactor at the earlier time (around 0.2 s), which represents short-circulating flow (bypassing process), following the RTD studies of Fogler (1999) and (Wolf and Resnick 1963). In addition, a long tail of the RTD curve at longer times represents the dead (stagnant) zones (Fogler 1999). Dead zones reduce the effective volume of the JSR, resulting in a smaller active reactor volume than expected (Fogler 1999). It can be concluded that the RTD curve for the simulated JSR does not follow the ideal perfectly mixed reactor because it does not coincide with the ideal reactor. Therefore, a theoretical model is needed to represent the inhomogeneity within the JSR.

6.4 CONCLUSIONS

In this chapter, a numerical analysis using the LES, Smagorinsly model is performed to analyze the flow characteristics in a 3-D configuration of a spherical JSR. In these simulations, the mixing quality is studied during a tracer decay technique following the experimental work of Ayass *et al.* (2016), in which nitrogen gas is injected into the steady state stream of carbon dioxide. The present large eddy simulations reproduce the large scale dynamics of the flow within the reactor, and the small scales are also modeled by the Smagorinsky turbulence model. This allows to capture the details of the flow field inside the JSR such as the temporal distribution of the tracer concentration and the velocity field, together with the evaluation of the mixing quality and the location of the dead spaces within the JSR.

The results of this chapter show that a continuous perpendicular stream is generated by two pairs of nozzles (i.e., the upwards and downwards pointing nozzles and the horizontal pointing nozzles) which leads to the enhancement of the turbulence level and the mixing efficiency inside the reactor. Furthermore, capturing the temporal evolution of the tracer mass fraction along three axes shows that a totally uniform composition is not obtained at the mean residence

time. In addition, comparing the calculated normalized RTD curve for the simulated JSR with an ideal reactor predicts the short circulating flow and dead spaces within the studied reactor.

7

CALCULATION OF NON-REACTING FLOW (INCLUDING NOZZLE FLOW MODELING)

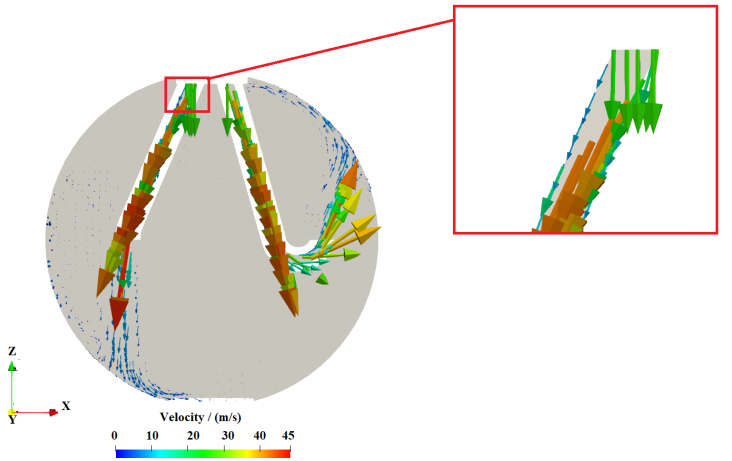

Figure 7.1: Velocity vectors through the upward and downward nozzles the x-z cross section (red box illustrates the velocity profile at the entrance of the downward nozzle)

In order to improve the results of the RTD studies presented in Section 6.3, the flow inside the nozzles is additionally considered in this chapter. It means, modeling of flow field inside the nozzles is added to the previous simulations (the JSR chamber having a spherical vessel of diameter of 40 mm). Figure 7.1 shows the 2-D distribution of the direction and the magnitude of the velocity vectors through the nozzles and inside the JSR. The velocity profile at the entrance exhibits a top-hat shape (as shown in the magnified red box of Fig. 7.1), characterized by a uniform and constant velocity of $26.96\,\mathrm{m\,s^{-1}}$ over the cross-sectional area of the nozzle entrance. Furthermore, obtaining a fully-developed turbulent flow at the outlet of the nozzle orifices results in a maximum velocity of approximately $48\,\mathrm{m\,s^{-1}}$. Therefore, it is expected that a flow with a higher turbulence level will be generated by the high velocity nozzle flow com-

pared to the results of the JSR modeling neglecting the flow through the nozzle (Chapter 6).

In this chapter, in order to estimate the accuracy of the numerical discretization, the Grid Convergence Method (GCI) (Celik *et al.* 2008) is first applied to a progressively reduced mesh size as presented in Section 7.1. Next, the flow characteristics inside the nozzles, such as the pressure and velocity distribution in the regions close to the nozzles are studied in Section 7.2. The initial and boundary conditions were presented in Section 5.1. Later, the details of the flow field within the spherical vessel such as the $\mathcal{Q}$-criterion and the velocity contour are analyzed in Section 7.3.

7.1 NUMERICAL ACCURACY IN TERMS OF RICHARDSON- EXTRAPOLATION

The main errors which might emerge through numerical simulations of the flow field are modeling errors, iterative convergence errors, and discretization errors (Roache 1997). In this section, the focus is on discretization error, which arise from the difference between the exact solution of the governing equations and the exact solution of the algebraic expressions in a discrete domain of space and time. In order to calculate discretization error estimation in the LES simulations, the Grid Convergence Index (GCI (Celik *et al.* 2008)) is used in the present study, which is based on Richardson- extrapolation method (Richardson 1911).

Discrete solution of a dependent variable ϕ can be written as follows (Roache 1998),

$$\phi_{\text{ext}} = \phi_{\mathcal{H}} + B_1\mathcal{H} + B_2\,\mathcal{H}^2 + B_3\mathcal{H}^3 + \dots, \tag{7.1}$$

where the exact value of a dependent variable and its approximations are denoted by ϕ_{ext} and $\phi_{\mathcal{H}}$, respectively, with a grid cell size of $\mathcal{H}$. The grid size can also be calculated using the following expression,

$$\mathcal{H} = \Big[\frac{1}{N}\sum_{i=1}^{N}(\Delta V_i)\Big]^{1/3}, \tag{7.2}$$

where ΔV_i is the volume of the ith cell. The error between the exact value and the approximated value E_r on the finite grid size is explained by,

$$E_r = \phi_{\text{ext}} - \phi_{\mathcal{H}} = B\,\mathcal{H}^{\mathcal{P}} + O(\mathcal{H}^{\mathcal{P}+1}) + \dots, \tag{7.3}$$

where $\mathcal{P}$ represents the apparent order of the numerical accuracy. The errors for three different grid sizes of $\mathcal{H}_1$, $\mathcal{H}_2$, and $\mathcal{H}_3$ from fine to coarse mesh are computed as (Roache 1998),

$$E_{r,1} = \phi_{\text{ext}} - \phi_1 = B\ \mathcal{H}_1^{\mathcal{P}}\,, \tag{7.4}$$

$$E_{r,2} = \phi_{\text{ext}} - \phi_2 = B\ \mathcal{H}_2^{\mathcal{P}}\,, \tag{7.5}$$

$$E_{r,3} = \phi_{\text{ext}} - \phi_3 = B\ \mathcal{H}_3^{\mathcal{P}}\,, \tag{7.6}$$

By subtracting Eq. 7.4 from Eq. 7.5 and Eq. 7.5 from Eq. 7.6, the following formula is obtained (Celik *et al.* 2008),

$$\mathcal{P} = \frac{\left|\ln\left(\left|\frac{\phi_3-\phi_2}{\phi_2-\phi_1}\right| + W_m(\mathcal{P})\right)\right|}{\ln(r_{21})}\,, \tag{7.7}$$

$$W_m(\mathcal{P}) = \ln\Big(\frac{\mathrm{r}_{21}^{\mathcal{P}} - \mathrm{s_m}}{\mathrm{r}_{32}^{\mathcal{P}} - \mathrm{s_m}}\Big)\,, \tag{7.8}$$

$$s_m = \mathrm{sgn}\Big(\frac{\phi_3 - \phi_2}{\phi_2 - \phi_1}\Big)\,. \tag{7.9}$$

The grid refinement factor is computed based on $r_{32} = \mathcal{H}_3/\mathcal{H}_2$ and $r_{21} = \mathcal{H}_2/\mathcal{H}_1$, which should be larger than 1.3 (Celik *et al.* 2008).

Also, the error of e_{a} approximates the error between the fine grid solution and the unknown exact solution, which is given by

$$e_{\mathrm{a}} = \left|\frac{\phi_1 - \phi_2}{\phi_1}\right|\,. \tag{7.10}$$

Using this method, the numerical uncertainty on the finest grid is evaluated by the GCI. The fine-grid convergence index, GCI_{fine} (Celik *et al.* 2008) is also estimated as (Celik *et al.* 2008),

$$GCI_{\text{fine}} = \frac{1.25\ e_{\mathrm{a}}}{r_{21}^{\mathcal{P}} - 1}\,. \tag{7.11}$$

Procedure to calculate Grid Convergence Index (GCI)

First, a representative grid size of $\mathcal{H}$ is defined based on the averaged cell size on progressively 3-D mesh sets of 1M, 490k, and 240k cells. Next, a number of essential variables were chosen to compute the discretization errors based on them, such as averaged velocity u_{ave} and mean residence time τ. Then, following the GCI procedure, the apparent order $\mathcal{P}$ is extracted from the three solutions ϕ_1, ϕ_2,

Table 7.1: An overview of discretization error over the time-averaged velocity u_{ave}, and the mean residence time τ (Esmaeelzade *et al.* 2021)

	u_{ave}	τ
$\mathcal{H}_1$	2.9×10^{-11} m	2.9×10^{-11} m
$\mathcal{H}_2$	6.61×10^{-11} m	6.61×10^{-11} m
$\mathcal{H}_3$	1.28×10^{-10} m	1.28×10^{-10} m
r_{21}	2.72	2.72
r_{32}	1.93	1.93
ϕ_1	$1.125\,\mathrm{m\,s^{-1}}$	0.339 s
ϕ_2	$0.982\,\mathrm{m\,s^{-1}}$	0.369 s
ϕ_3	$0.956\,\mathrm{m\,s^{-1}}$	0.374 s
$\mathcal{P}$	1.25	1.23
e_a	12%	8.8%
GCI_{fine}	4%	3.2%

and ϕ_3 on the mesh sets with an average cell size of $\mathcal{H}_1$, $\mathcal{H}_2$, and $\mathcal{H}_3$, respectively, based on Eq. 7.7. Table 7.1 outlines the results of numerical uncertainty. The apparent order of discretization for the average velocity is approximated as 1.25 and for the mean residence time as 1.23, which both are in the expected range as mentioned in the literature (Celik *et al.* 2008). The GCI represents the numerical errors which is estimated as 4% and 3.2%. Even though we cannot separate the contributions of the errors, their sum has a minor effect on the key results (Bose *et al.* 2010). Therefore, it can be concluded that the numerical errors can be neglected in this chapter and for further simulations a total number of cells of 490k is considered.

7.2 FLOW FIELD STUDY OVER THE NOZZLES

Due to the importance of the turbulent jets generated by the nozzle on the flow mixing inside the JSR, this section focuses on the flow field characteristics through the nozzles.The distribution of the time averaged velocity magnitude (time interval from 0.01 s to 0.04 s) over four lines is shown in Fig. 7.2. These lines are located inside and outside of the downstream nozzle, parallel to the x-axis, with a grid spacing of 3×10^{-6} m. The vertical distances of the segments from the entrance of the nozzle are presented by z (see Fig. 7.2b).

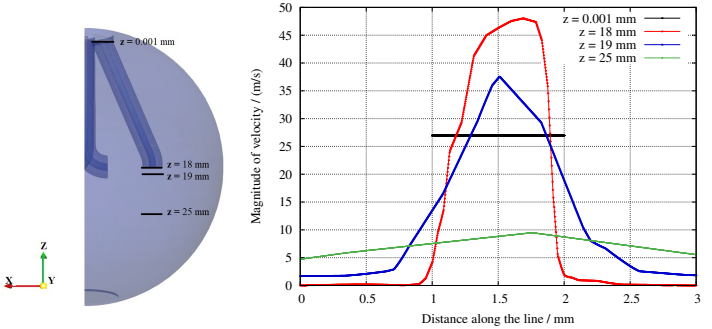

(a) (b)

Figure 7.2: Magnitude of the velocity profile along four segments over the downwards pointing nozzle

Specifically, the segment of $z = 0.001$ mm is situated inside the nozzle (very close to the nozzle entry) and extends for a length of 1 mm. The other three segments are located outside the nozzle at $z = 18$ mm (very close to the nozzle exit), $z = 19$ mm, and $z = 25$ mm with a length of 3 mm (see Fig. 7.2a).

As shown in Fig. 7.2b, a top-hat and uniform velocity profile of $26.96\,\mathrm{m\,s^{-1}}$ is distributed over the line of $z = 0.001$ mm. Furthermore, the velocity profile is fully developed along the nozzle axis and reaches its highest magnitude of $48.9\,\mathrm{m\,s^{-1}}$ (see segment $z = 18$ mm) due to the pressure drop inside the nozzle, which can be described by the head form of the energy (White 1990). According to White (1990), the turbulent velocity profile in the center of the nozzle drops sharply to zero at the wall. Such a trend is predicted by the segment $z = 18$ mm in Fig. 7.2b, but an asymmetric profile of the velocity distribution is captured due to the bend of the downward nozzle at the exit of the orifice. It should be noted that such a curvature along the upwards and the horizontal pointing nozzles of the JSR has a drastic effect on the asymmetry of the velocity profile, which improves the mixing within the reactor (Keulegan and Beij 1937).

In the same way, for two additional segments located outside the nozzle at $z = 19$ mm and $z = 25$ mm, a higher magnitude of velocity is obtained at the region closer to the center of the jet. Furthermore, within the decaying jet region (region between the nozzle exit and the walls, see Section 2.1), the velocity magnitudes along these segments ($z = 19$ mm, 25 mm) predict lower values compared to the

exit of the downward nozzle (z = 18 mm). Comparing the segments of z = 19 mm and z = 25 mm shows that the axial velocity in the center line of the z-axis decays and the radial velocity along the x-axis increases (as already discussed in section 2.1) (Fellouah *et al.* 2009). Note that the interaction of other nozzles pointing upwards, and horizontally can affect the asymmetrical distribution of velocity.

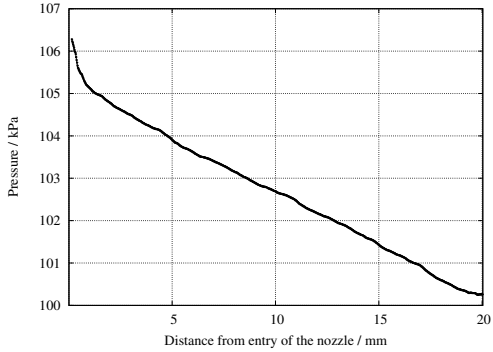

Figure 7.3: Time averaged pressure distribution over the length of the nozzle downward pointing

Next, the distribution of the time averaged pressure along the axis of the downwards pointing nozzle is illustrated in Fig. 7.3. The averaged pressure declines in the direction of flow movement due to the energy loss resulting from flow friction, as already predicted by the work of Keulegan and Beij (1937). Such a pressure drop along three other nozzles (upward and horizontal nozzles) is also captured. Al-Rafai *et al.* (1990) predicted more pressure drop in a smaller and highly curved nozzles, which can improve mixing inside the chamber.

Furthermore, the rate of pressure loss at the nozzle entrance (where a nearly inviscid stream flow converges and enters the nozzle (White 1990)) is greater than in the fully developed region, as already predicted by Düz (2019) (see the slope of the pressure distribution over the distance of 0 mm-2 mm from the nozzle entry in Fig. 7.3). The reason for the significant change in the pressure drop at the nozzle entry (around 1 kPa) is related to the difference in the direction of flow injection and the inclination of the nozzle. More specifically, the downward nozzle has an inclination of 25° to the y-z plane, although a top-hat velocity profile parallel to the z axis is defined at the nozzle entrance. Therefore, the adjustment of the velocity distri-

bution to the nozzle bend, which takes place at the entrance of the nozzle, affects the pressure drop more than the pressure drop along the nozzle (Keulegan and Beij 1937).

7.3 DETAILS OF THE FLOW FIELD

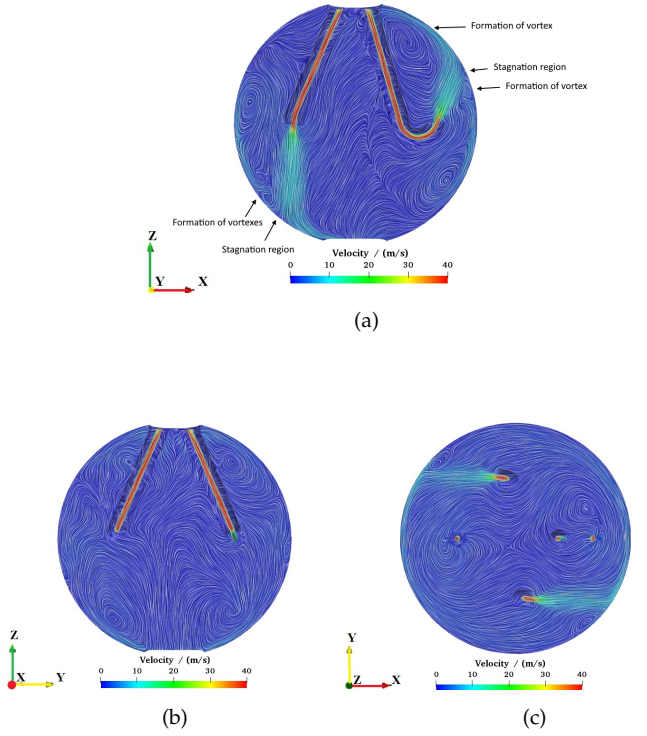

Figure 7.4: Time averaged velocity field visualized by the LIC method in the cross-sections of (a) the $x-z$ axes, (b) the $y-z$ axes, (c) the $x-y$ axes

Due to the importance of the jets in the performance of a JSR, the post processing tools of surface-Line Integral Convolution (LIC) technique in *paraview* is used in the current study to illustrate the velocity contour over the spherical vessel and inside the nozzles, as shown in Fig. 7.4. The LIC technique was first introduced by Cabral and Leedom (1993) and used an image vector field algorithm to visualize the flow traces more efficiently. This method provides a qualitative representation of the flow, indicating regions of high

or low velocity, vortices, separation regions, and gradients, allowing for a better understanding of the complex and detailed flow fields compared to the streamlines (Satheesh Kumar *et al.* 2020). As shown in Fig. 7.4a, the turbulent jets issuing from the nozzles pointing downwards and upwards, approach the in-front walls of the spherical vessel, the axial velocity of the jets is reduced in the stagnation region and then several vortices are formed along the wall jet region (see Section 2.1). The vortical structures, which contain a wide range of turbulent lengths, play a leading role in improving the mixing quality inside the JSR. The same behavior is captured for the other two jets issuing from the nozzles pointing in horizontal directions, as illustrated in Figs. 7.4b and 7.4c. In conclusion, generating a highly turbulent vortex regime emerges from four nozzles leads to improving the mixing of the composition inside the reactor.

In contrast to the generation of several vortices near the spherical vessel and the outer diameter of the nozzles, fewer vortical structures were captured in the center of the JSR and the conical area between the nozzles (see Fig. 7.4), which negatively impacts the efficiency of mixing within the reactor. This could be a motivation for the development of an optimal configuration of multiple pairs of the jets as discussed in Chapter 10.

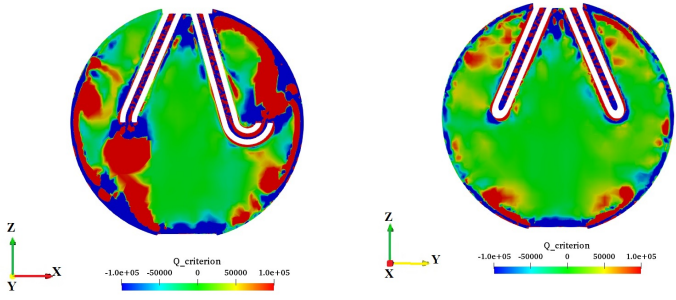

(a) (b)

Figure 7.5: Visualization of the distribution of time averaged $\mathcal{Q}$-criterion in the cross section of (a) the x-z and (b) z-y planes (Esmaeelzade *et al.* 2021)

To identify existence of the vortex and the vortical structures within the JSR, the post processing tools of $\mathcal{Q}$-criterion is used in

this study (Jawahar *et al.* 2018). This criterion is calculated based on the second invariant of velocity gradient tensor (OpenFOAM, Jawahar *et al.* 2018),

$$\boldsymbol{\mathcal{Q}} = \frac{1}{2}(\boldsymbol{\Omega}^2 - \boldsymbol{S}^2)\,, \tag{7.12}$$

$$\Omega_{i,j} = \frac{\partial u_i}{\partial x_j} - \frac{\partial u_j}{\partial x_i}\,, \tag{7.13}$$

where,

$$S_{i,j} = \frac{\partial u_i}{\partial x_j} + \frac{\partial u_j}{\partial x_i}\,. \tag{7.14}$$

Here, $\boldsymbol{S}$ and $\boldsymbol{\Omega}$ represent the strain rate tensor and the rotation tensor, respectively (Chong *et al.* 1990), which are derived from the velocity components. A positive value of the $\boldsymbol{\mathcal{Q}}$ represents that the vorticity field is dominant and a negative value of it means that shear and strain rates have the leading roles. Figures 7.5a and 7.5b illustrate the distributions of the time-averaged $\boldsymbol{\mathcal{Q}}$-criterion in the cross section of the x-z and the y-z planes, respectively. As expected, the regions coherent to the spherical vessel walls, to the nozzle walls, and close to the outlet predict a strong shear region (see blue regions in Fig. 7.5). Slightly farther from the walls and in the areas where the turbulent jets hit the in-front wall, significant vorticity is generated (see Fig. 7.5a). This shows the importance of the turbulent jets in generating the vortical structures within the JSR. On the other hand, in the center of the spherical chamber, the value of the $\boldsymbol{\mathcal{Q}}$-criterion is almost zero due to the interaction of two circumferential flows generated by two pairs of nozzles. This means that the values of vorticity and strain rate in the center of the JSR are equal. It can be concluded that the center of the JSR acts as a dead zone within the reactor, preventing efficient mixing within the JSR.

In order to obtain a homogeneous and fully-mixed composition inside the JSRs, the highly-turbulent structures are desired to be distributed uniformly over space and time (Abdalla *et al.* 1982). To study this issue, turbulent kinetic energy and turbulent dissipation rate could be a proper representative of the mixing quality within the JSR. Figures 7.6a and 7.6b show the distribution of the resolved turbulent kinetic energy calculated based on Eq. 3.31 and the subgrid scale (SGS) dissipation rate using the LES turbulence modeling, respectively. Note that the resolved turbulent kinetic energy using a well-resolved LES simulation could be a representative of a total Turbulent Kinetic Energy (TKE) since the resolved one contains 80%

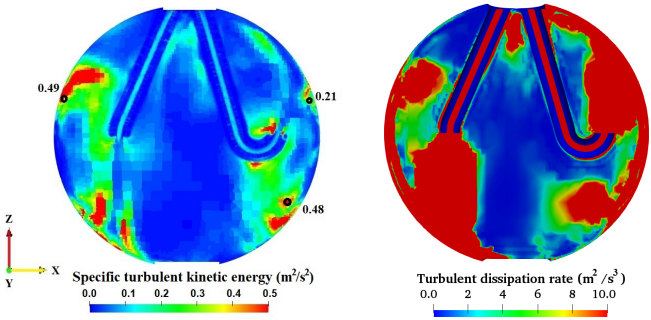

(a) (b)

Figure 7.6: (a) Distribution of the resolved specific turbulent kinetic energy, and (b) SGS dissipation rate in the x-z plane (Esmaeelzade *et al.* 2021)

of the total energy (Pope 2000). As can be concluded from Fig. 7.6a, the highest turbulence fluctuations occur where the jets hit the inner surface of the vessel, as discussed previously by Hodzic *et al.* (2018). This behavior indicates the importance of jets for the design of the JSRs. Furthermore, capturing the TKE and dissipation rate at the center of the JSR proves the lack of the turbulent structures there.

The SGS dissipation rate in Fig. 7.6b is computed based on Eq. 3.32, which is nearly equal to the total dissipation rate. As can be concluded from Fig. 7.6b, the highest dissipation rates are obtained at the exit and through the nozzles, as well as where the jets impinges the spherical wall. Note that the values of the resolved specific turbulent kinetic energy over three points were specified in Fig. 7.6a for further comparison of cases mentioned in Chapters 8 and 10.

As mentioned in Section 3.2, in order to analyze the distribution of TKE across eddies of different sizes (wave number) and frequencies, the energy spectra is studied (Pope 1985). Figure 7.7 shows the specific kinetic energy density versus frequency for a point located at the center of the JSR. In order to plot the energy spectra, the Fast Fourier Transform (FFT) of the velocity field is computed over a time interval of 0.01 - 0.06 s, which is larger than the integral time (Grosshans and Papalexandris 2017). According to Fig. 7.7, the specific kinetic energy density has a maximum value for the frequency numbers corresponding to the large energy-containing ed-

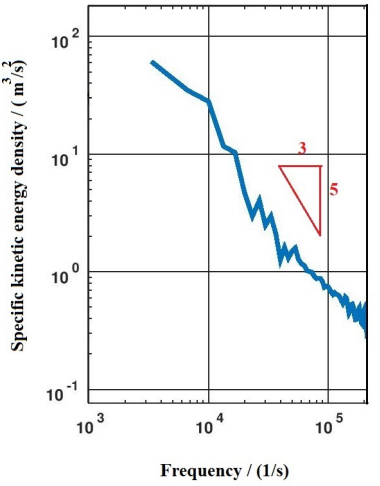

Figure 7.7: Specific kinetic energy spectrum at the point located in the center of reactor (Esmaeelzade *et al.* 2021)

dies. Moreover, the energy spectrum follows the $-5/3$ law for a wide range of frequencies, which indicates a state of fully-developed turbulence. Note that the energy spectrum is captured for frequencies less than $10^5\,\mathrm{s}^{-1}$. That means for those frequencies that are properly resolved by the numerical time step.

7.4 CONCLUSIONS

The turbulent flow inside the nozzles is modeled and its characteristics are further studied by means of well-resolved large vortex simulations. First, the accuracy of the numerical modeling is proved by applying the Richardson-extrapolation method. By initializing a top-hat shaped velocity at the nozzles entry, a developed velocity profile is obtained at the exit of the nozzle. As the turbulent jets leave the nozzles and approach the in-front walls, axial velocity develops over the walls of the spherical vessels and forms vortical structures.

In this chapter, the flow streams and the interaction of four jets were illustrated using the LIC method. This approach effectively captures the vortical structures in the regions close to the JSR walls. In

addition, analyzing the time-averaged distribution of the $\mathcal{Q}$-criterion reveals the potential of the coherent regions to the walls for the shear stress and the regions farther from the walls and the jets for the vorticity. Moreover, the center of the JSR chamber and between the jets suffers from good mixing and predicts an almost zero value of the $\mathcal{Q}$- criterion. Therefore, the center of the JSR is considered a dead zone that prevents sufficient mixing inside the reactor. The absence of turbulent structures in the central region is subsequently confirmed through the comprehensive analysis of the TKE and its dissipation rate within the JSR. Furthermore, the result obtained by plotting the energy spectrum over a wide range of frequencies follows the $-5/3$ law, which is representative of a fully developed turbulent state.

8

PARAMETRIC STUDY

In order to find out the best mixing condition within the spherical JSR, a parametric study is performed on the geometrical (Section 8.1) and thermodynamic parameters (Section 8.2). For this purpose, the diameter of the spherical vessel and the turbulent nozzles together with the operating pressure and temperature are changed. Table 8.1 represents an overview of the studied conditions which are discussed in this chapter. To compare the mixing behavior within the studied JSRs with different sizes, the theoretical residence time is kept identical to 0.37 s (ideal case, Eq. 2.4). Accordingly, the volumetric flow rate for each case is calculated. It should be mentioned that a JSR with a vessel diameter smaller than 35 mm and larger than 65 mm and also the nozzles diameter less than 1 mm were not studied in the present work, because of the limitations of the construction of the JSR, as discussed in Section 2.2.

Table 8.1: Operating conditions in terms of the diameter of the spherical chamber (D), the diameter of the nozzles (d), temperature (T), and pressure (p)

D	d	T	p
40 mm	1 mm	298 K	1 bar
60 mm	1 mm	298 K	1 bar
35 mm	1 mm	298 K	1 bar
40 mm	1.5 mm	298 K	1 bar
40 mm	1 mm	700 K	1 bar
40 mm	1 mm	298 K	0.1 bar
40 mm	1 mm	298 K	10 bar

Next, to compare the mixing performance inside the JSR considering different conditions, the normalized weighted standard deviation of CO_2 mass fraction is calculated according to Eq. 2.10. The standard deviation using volume as a weighted factor shows the deviation of the tracer mass fraction from its mean value considering

the volume of each zone. Therefore, when σ_m approaches zero, the deviation between the tracer mass fraction and the average value becomes smaller, leading to a more homogeneous composition.

8.1 PARAMETRIC INVESTIGATION OF THE THERMODYNAMIC CONDITIONS

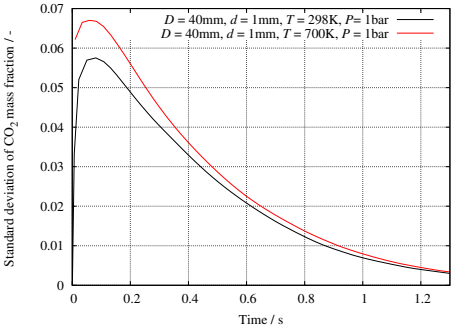

Figure 8.1: Temporal evolution of the weighted normalized standard deviation of the tracer mass fraction at different operating temperatures

Figure. 8.1 shows the normalized weighted standard deviation σ_m of the tracer over time at different operating temperatures of 298 K and 700 K in a non-reacting mixture of CO_2 and N_2 within the JSR. It should be mentioned that the initial and boundary conditions of temperature are only elevated to the mentioned value and other parameters such as the operating pressure of 1 bar and the geometrical conditions have the same values as the standard JSR designed by Dagaut *et al.* (1986), as discussed in Section 5.1. As shown in Fig. 8.1, σ_m increases at the beginning time ($t < 0.05$ s) for the both cases. This is because, according to the experimental procedure (Ayass *et al.* 2016), N_2 stream is suddenly injected through the nozzles into CO_2 stream and increases the standard deviations of CO_2 mass fraction. However, after a certain moment (around $t > 0.05$ s), the deviation between CO_2 mass fraction and the averaged value (σ_m) decreases as the fluid elements leave the JSR.

According to Fig. 8.1, a higher operating temperature predicts a higher value of σ_m compared to the lower operating temperature case in the initial phase (the time interval of 0 s-1.2 s). Hence, one

might include that a higher amount of inhomogeneity is predicted for the JSR operating at higher temperatures at the mean residence time of 0.37 s. However, at the steady state (after time instant of 1.2 s), which is approximately 3.2 times longer than the mean residence time duration, both cases converge to a level of the standard deviations under 0.006. Therefore, it can be concluded that mixing efficiency and homogeneity at higher temperature predict similar values to those at lower temperature over a longer period of time.

The reason for the higher standard deviation of the temperature of 700 K compared to the temperature of 298 K at the mean residence time can be explained by a number of reasons. First, higher temperatures decrease the gas density following the ideal gas law. Therefore, a decrease in the gas density leads to a decrease in the Reynolds number and a decrease in the residence time. Second, the molecular viscosity is calculated by the Sutherland law as a function of temperature,as already described in Section 3.6. This means that increasing temperature leads to an increase in the dynamic gas viscosity (Kenney *et al.* 1956). More specifically, higher temperatures affect the rapid motion of gas molecules and their collision, and thus the gas viscosity rises. An increase in the gas viscosity also decreases the Reynolds number. Consequently, the Reynolds number of the gas mixture decreases as the temperature increases. In lower Reynolds number flow, less turbulent fluctuations are generated, which leads to low-intensity mixing and consequently impairs the homogeneity of the composition inside the JSR. To prove that the TKE and its dissipation rate inside the JSR for both temperatures are compared. The resolved turbulent kinetic energy and the turbulent dissipation rate (calculated based on Eq. 3.32) globally and locally (over three identical points for both cases), at the temperature of 700 K is shown in Fig. 8.2. Comparing these figures with the TKE and dissipation rate at the temperature of 298 K (as shown in Fig. 7.6) shows that the kinetic energies of the resolved turbulent structures and their dissipation rate at higher temperature have lower values; hence, mixing quality is poor compared to that at the temperature 298 K. This leads to the prediction of a higher standard deviation of the tracer mass fraction at the higher temperatures.

Next, the effect of the operating pressure on the JSR homogeneity and mixing quality is studied. For a Jet Stirred Flow Reactor (JSFR), maximum mixing for gas phase operation is captured at higher pressures since pressure improves fluid dynamic jet stirring (Lignola and Reverchon 1988). Such a behavior (improving the JSR mix-

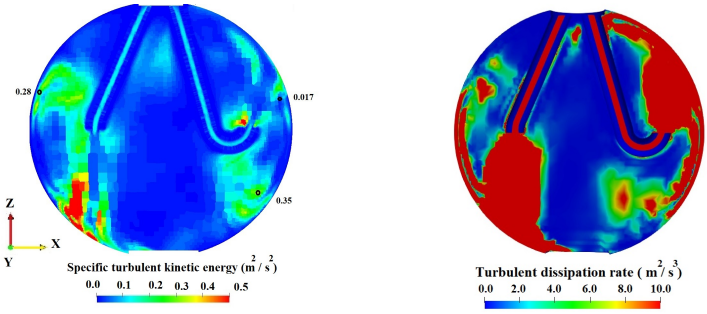

(a) (b)

Figure 8.2: Distribution of the (a) resolved specific turbulent kinetic energy and (b) turbulent dissipation rate of the flow field in the x-z plane for the case of $T = 700\,\mathrm{K}$ (Esmaeelzade *et al.* 2021)

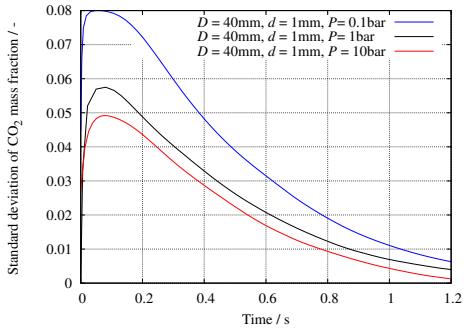

Figure 8.3: Temporal evolution of the normalized weighted standard deviation of the tracer mass fraction for an elevated pressure (Esmaeelzade *et al.* 2021)

ing quality at higher pressures) is also captured through the studied simulation. As shown in Fig. 8.3, simulating the JSR at the operating pressure of 0.1 bar predicts a greater standard deviation and consequently less optimal mixing within the JSR compared to the pressures of 1 bar and 10 bar, especially in the initial stages. The reason for improving the mixing quality at the higher operating pressure can be related to the increase in gas density at higher pressure. Therefore, a gas composition having a higher gas density tends to

keep the fluid elements inside the reactor longer and prevents the short circulation of the fluid elements.

Another reason can be related to the distribution of fluctuating components and vortical structures inside the reactor and their role in mixing. In fact, an increase in gas density leads to a higher Reynolds number of the gas mixture, resulting in more turbulent fluctuations and better mixing at the higher pressure compared to the lower pressures. Figures 8.4a and 8.4b represent the time-averaged velocity magnitude captured with the LIC method at the location close to the outlet surface (over the x-y plane) for a pressure of 1 bar and 10 bar, respectively. Comparing these two figures shows that the higher pressure of 10 bar predicts a higher value of velocity and also a larger number of vortexes. It is therefore expected that the mixing field will be improved in high Re number flows with highly turbulent structures (Pope 2000).

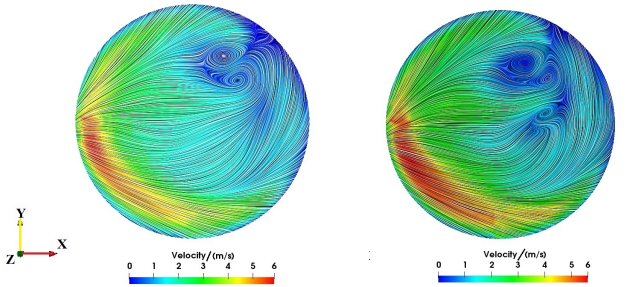

(a) (b)

Figure 8.4: Time-averaged velocity contour (in the range of 0.08 s - 0.09 s after tracer injection) extracted with the LIC method in the cross section described by the x-y axes over the outlet surface for the case of (a) p=1 bar and (b) p=10 bar (Esmaeelzade *et al.* 2021)

8.2 PARAMETRIC INVESTIGATION OF THE GEOMETRICAL CONDITIONS

Figure. 8.5a illustrates the comparison of the normalized weighted standard deviation of CO_2 mass fraction over time for different diameters of a spherical vessel and the size of the nozzle diameter, while the thermodynamic conditions for all cases were kept as ambient conditions.

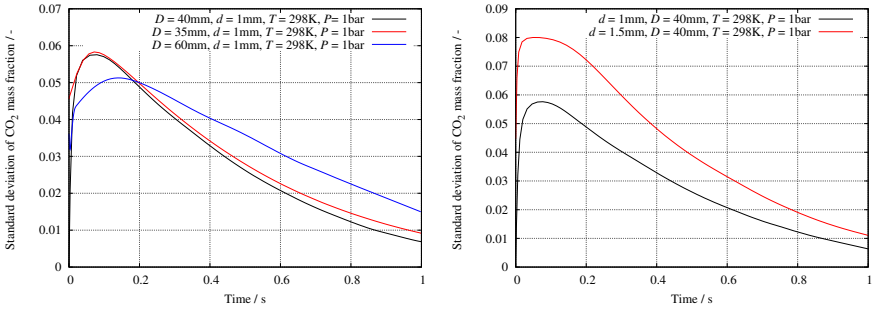

(a) (b)

Figure 8.5: Temporal evolution of the normalized weighted standard deviation of the tracer mass fraction for different (a) diameters of spherical vessel and (b) nozzle diameters (Esmaeelzade *et al.* 2021)

From this plot, we understand that the JSR with a diameter of 40 mm predicts a lower value of the standard deviations of the tracer compared to the case of D = 35 mm and D = 60 mm in the steady behavior (over the longer time period). That means the standard design of the JSR with spherical chamber of 40 mm (Dagaut *et al.* 1986) predicts a more homogeneous composition and better mixing performance. Although the JSR with a diameter of 35 mm predicts values very close to the standard JSR at earlier times, it shows a deviation in the steady state. Indeed, the smaller vessel of 35 mm with the same diameter of outlet of 10 mm leads to more short circulation of the flow compared to the case of 40 mm, since the distance between the nozzles and the outlet is shorter than the case of smaller reactor.

Note that during the filling process of the JSR, the reactor of D= 60 mm reaches its maximum of standard deviation later (at t = 0.15 s) compared to the other two cases. Because N_2 stream is suddenly injected into a homogeneous composition of CO_2, therefore the fluid elements leave the outlet in a longer distance and time compared to a smaller vessel. Therefore, a homogeneous composition is achieved in a later stage.

Further, the tracer standard deviation over time for two cases of the JSR having a nozzle diameter of d = 1.5 mm and d = 1 mm are compared in Fig. 8.5b. The results indicate that increasing the nozzle diameter does not improve mixing inside the JSR since a higher standard deviation is predicted for the nozzle diameter of

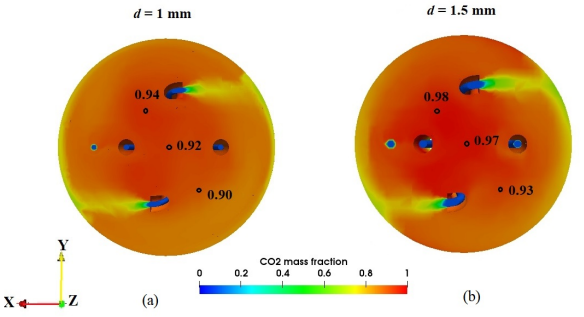

Figure 8.6: Dead spaces visible in the time-averaged distribution of CO_2 mass fraction (at the time interval of 0.08 s - 0.09 s after the tracer's injection) over the x-y plane for the cases of (a) d = 1 mm; D = 40 mm, (b) d = 1.5 mm; D = 40 mm (Esmaeelzade *et al.* 2021)

d = 1.5 mm. The reason can be explained by comparing the highest Reynolds number for both cases. For a better comparison, the theoretical mean residence time of 0.37 s is considered identical for both cases. Therefore, the volumetric flow rate and the volume must be equal. The total volume of both reactors is the same since only the nozzle diameter was changed. In order to keep the same volumetric flow rate (Q= $\boldsymbol{u}A_s$) in both situations, the inflow velocity magnitude at the nozzle exit must be smaller in the case of d = 1.5 mm than in the case of d = 1 mm, which leads to a lower Re number. Accordingly, a flow with a lower Re number is expected to have less turbulence, resulting in poor mixing within the JSR. Furthermore, lower intensive vortical structures intensify the dead zones, which means a very small exchange of material happens inside the reactor with insufficient molecular mixing (Corrigan and Beavers 1968).

Figure 8.6 compares the time-averaged mass fraction of the tracer over the x-y plane in the case of the nozzle diameter of (a) d = 1 mm and (b) d = 1.5 mm. Considering the same time interval for both cases, the local mass fraction of CO_2 over three points inside the JSR for the case of the larger diameter of nozzles reveals a larger value of the tracer mass fraction. This means that a more intensive distribution of the dead zones is captured in the case of the large diameter of the nozzle, which impairs the efficient mixing of the composition inside the JSR.

8.3 CONCLUSIONS

This chapter presents the results of a parametric study of the effect of temperature and geometrical parameters on mixing inside a spherical JSR. The normalized weighted standard deviation is calculated for each case over a longer period of time. Operating the JSR at a lower temperature for a non-reacting case leads to a better mixing inside the JSR. Since the calculated turbulent kinetic energy and its dissipation have lower values compared to the ambient temperature. Therefore, lower fluctuations lead to a weaker mixing quality. Note that after a certain time, the standard deviation of the different temperatures will coincide, representing the achievement of a similar level of homogeneity over time. Furthermore, the simulation of the spherical JSR at higher pressure leads to better mixing at earlier times. The formations of vorticity over the outlet at the pressure of 10 bar confirms the existence of more turbulent structures and therefore a more efficient mixing compared to the cases of 0.1 bar and 1 bar. Moreover, comparing the results of the standard deviation of the tracer mass fraction in different sizes of the vessel shows that a standard JSR design with a vessel diameter of 40 mm and nozzle diameter of 1 mm predicts a more homogeneous composition.

9 APPLICATION OF MULTI-ZONE MODEL

The results of Chapters 6- 7, and the experimental residence time distribution curves presented in Ref. (Ayass *et al.* 2016), show that an ideal JSR with a theoretical mean residence time of 0.37 s cannot be achieved. Therefore, the Perfectly Stirred Reactor (PSR) model, which assumes a fully-mixed and homogeneous composition, cannot be used for analyzing the detailed chemical kinetic mechanisms inside the JSRs. In order to model the imperfect mixing within the studied JSR, a theoretical multi-zone model is developed as described in Section 4.2 and later implemented in HOMogeneous REAction (HOMREA) (Maas and Warnatz 1988). In this chapter, the developed multi-zone model is applied to the oxidation processes of dimethyl ether (DME) or CH_3OCH_3 from the NUI-Galway mechanism (Burke *et al.* 2015b).

First, the initial conditions of the simulation setups are introduced in Section 9.1. Subsequently, the non-uniform distribution of the mole fractions of the reactants during DME oxidation over several zones inside the JSR is studied in Section 9.2. Next, the impact of mixing exchange rate between zones on the multi-zone model is investigated in Subsection 9.2.1. Additionally, the effect of different numbers of zones on capturing the non-ideal behavior of the JSRs is elaborated in Subsection 9.2.2. After that, Section 9.3 addresses the results of the inhomogeneous distribution of the total volume through the reactor, while each zone's temperature and the initial mole fraction of the reactants do not change over time. Later, the effect of nonuniform wall temperature over the zones is investigated in Section 9.4. Next, the effect of different heat transfer coefficients using the single zone model is investigated in Section 9.5. Finally, the nonuniform distribution of heat transfer coefficient over zones using the developed multi-zone model is studied in Section 9.6. Therein, the volume and the initial mole fractions of the reactants are kept identical over all zones.

In this chapter, the predicted species mole fraction profiles using the multi-zone model are compared to a PSR model and the experimental results reported in Ref. (Moshammer *et al.* 2016).

9.1 SIMULATION SETUP IN HOMREA

Since the applied multi-zone model uses zero-dimensional equations, the JSR vessel cannot be divided into spatial zones. Therefore, in the present study, the JSR volume is divided into a number of representative zones. Based on the multi-zone model the sum of all five zones must be equal to the total volume. The multi-zone model proceeds through the following steps.

1. The inflow and initial conditions for the HOMREA input file are derived from the experimental data in Ref. (Moshammer *et al.* 2016). These include parameters such as the inflow and the initial mixture composition of $X_{\mathrm{DME}} = 2.295$, $X_{\mathrm{Ar}} = 78.097$, and $X_{\mathrm{O_2}} = 19.607$, the pressure of 0.933 bar, the total internal volume of $33.5 \times 10^{-6}\,\mathrm{m^3}$, the inflow rate of $8.51 \times 10^{-6}\,\mathrm{kg\,s^{-1}}$, the inflow temperature of 350 K, and the initial wall temperature in the range of 460 - 1000 K.

2. Subsequently, the multi-zone model examines several parameters individually to capture the source of the inhomogeneity within the JSR. These parameters include the inhomogeneous distribution of the initial mole fractions, the total volume, the initial wall temperature, and the heat transfer coefficient. Limits for each parameter were determined based on experimental data (Cornell *et al.* 2022, Rousso *et al.* 2018, Stoehr *et al.* 2015). For example, following the estimated uncertainty of the reactant composition in Ref. (Cornell *et al.* 2022), inhomogeneous distribution of the reactant mole fractions of 4% were considered between the zones using the multi-zone model, as discussed in Section 9.2. However, the volume of 0.2 V_{tot}, the heat transfer coefficient of $25\,\mathrm{W\,m^{-2}\,K^{-1}}$, and the inflow gas temperature of 350 K are assumed to be identical for all zones.

   Section 9.3 specifies inhomogeneous distribution of the total volume, considering the volume of 1%, 24%, 35%, 5%, and 26% of the total volume from the first to the fifth zone, respectively. In this section, the inflow composition of $\mathrm{DME/Ar/O_2}$ with the equivalence ratio of 0.35 enters the JSR at a temperature of 350 K.

   Next, based on the temperature uncertainty reported by Rousso *et al.* (2018), the wall temperature of the JSR is considered differently for each zone (10 K between the zones), as studied in Section 9.4. Here, the initial mole fraction of the reactants

(equivalence ratio of 0.35), the volume (0.2 V_{tot}), the heat transfer coefficient (25 $W\,m^{-2}\,K^{-1}$), and the inlet gas temperature of 350 K are maintained identical for all zones.

Finally, the stability of the oxidation of DME is investigated by a single zone model considering different values of the heat transfer coefficient in Section 9.5. Based on the results of the single zone model, the multi-zone model considers inhomogeneous distribution of the heat transfer coefficient over zones in Section 9.6. In this section, the inflow and the initial conditions for the mole fractions, the volume, and the initial temperature are considered identical for all zones.

3. The multi-zone codes calculate the model parameters (mass and heat exchange rates between the zones, and heat transfer coefficient) based on the Computational Fluid Dynamic (CFD) results. More specifically, the mass exchange rate obtained/-given by a zone is proportional to the mass of the zone, the mass ratio of the interacting zones, and the mixing frequency (see Eqs. 4.11 and 4.12). In this study, the mixing frequency of 1.2 s^{-1} is given to the HOMREA as an input value and is calculated as Eq. 4.14 (the model parameter of 0.18 and the turbulent frequency of 6.8 s^{-1}). The turbulent frequency is calculated as the dissipation rate of the TKE divided by the total turbulent kinetic energy (see Eq. 4.15). The turbulent frequency is determined by dividing the dissipation rate of turbulent kinetic energy (TKE) by the total turbulent kinetic energy, as derived from CFD calculations.

   The heat exchange rate between zones is specified in the multi-zone as a function of the mass exchange rate and the difference between the enthalpy and mass fraction of the interacting zones (see the sixth and the seventh terms of Eq. 4.6). Furthermore, the heat transfer coefficient of 3.28 $W\,m^{-2}\,K^{-1}$ between the zone and its wall follows the gas heat transfer correlation based on the Nusselt number (Lignola and Reverchon 1986). In particular, the heat transfer coefficient is specified as a function of the thermal conductivity of the mixture, the Reynolds number (based on the averaged velocity), the Prandtl number (based on the viscous and thermal diffusion rate of the mixture), and the diameter of the spherical chamber (see Eq. 4.16). Note that enthalpy, internal energy, molar

production rate, and molar mass of species are provided by the HOMREA.

4. Finally, the governing equations from Eq. 4.4 to 4.6 are solved in the multi-zone model.

Note that the initial time step of 1.00×10^{-7} s is considered for all simulations in the multi-zone model. Furthermore, the absolute and relative error tolerance of 1.00×10^{-9} and 1.00×10^{-7} are specified, respectively, for defining accuracy of mole fractions, and the thermodynamic parameters.

Table 9.1: Adjustment of the total volume (V_{tot}) with the reactor temperature (T) and the residence time ($\frac{m}{\dot{m}_{in}}$), following the PSR model in Ref. (Moshammer *et al.* 2016)

T	$\frac{m}{\dot{m}_{in}}$	V_{tot}
460 K	3.93 s	35.5×10^{-6} m^3
500 K	3.89 s	38.2×10^{-6} m^3
540 K	3.85 s	40.9×10^{-6} m^3
580 K	3.82 s	44.4×10^{-6} m^3
620 K	3.80 s	47.1×10^{-6} m^3
660 K	3.77 s	49.5×10^{-6} m^3
700 K	3.75 s	52.0×10^{-6} m^3
740 K	3.73 s	54.6×10^{-6} m^3
780 K	3.72 s	57.7×10^{-6} m^3
820 K	3.70 s	61.4×10^{-6} m^3
860 K	3.69 s	64.7×10^{-6} m^3
900 K	3.68 s	67.6×10^{-6} m^3
940 K	3.67 s	70.2×10^{-6} m^3
980 K	3.66 s	72.7×10^{-6} m^3
1000 K	3.65 s	73.9×10^{-6} m^3

Moreover, following the PSR model used in Ref. (Moshammer *et al.* 2016), the mean residence time was calculated based on $\tau = \frac{m}{\dot{m}_{in}}$ and was adjusted in the range of 3.65 - 3.93 s. As mentioned in Ref. (Moshammer *et al.* 2016), the temperature measured by the thermocouple is lower than the actual reactor temperature. Therefore, the residence times obtained by the experimental data (Moshammer *et al.* 2016) were lower than the targeted value of 4 s, because the inflow mass

flow rate is fixed for all cases. Accordingly, it was necessary to adjust the residence time to the experimental values. To this end, the reactor volume was adjusted for each temperature (Moshammer *et al.* 2016). Table 9.1 represents the adjusted residence times and the volume reactor in the temperature range used in Ref. (Moshammer *et al.* 2016) and applied in the studied simulations.

9.2 CONSIDERING INHOMOGENEOUS MOLE FRACTION DISTRIBUTION

According to the JSR experimental setup in Refs. (Cornell *et al.* 2022, Moshammer *et al.* 2015), an uncertainty in the reactant mixture composition is estimated. In order to study the effect of the uncertainty of the reactant composition on the products during the oxidation of DME, the developed multi-zone is applied considering different initial mole fractions distributed in the representative zones. In this section, the total volume of the JSR is divided equally into five zones. From the first to the last zone, the mole fraction of DME changes by 4%, while keeping the equivalence ratio of 0.35. Table 9.2 represents the distribution of the initial mole fraction of the reactants in each zone.

Table 9.2: Operating conditions for the case of inhomogeneous mole fraction distribution

Zone	X_{Ar}	X_{DME}	X_{O_2}
1	76.344	2.478	21.176
2	77.220	2.387	20.391
3	78.097	2.295	19.607
4	78.973	2.203	18.823
5	79.84	2.111	18.039

Furthermore, the inlet gas temperature of 350 K is assumed for all simulations. The wall temperature and the initial temperature of the zone are both set to the same value (in the range of 460 - 1000 K). Note that assuming a large value for the heat transfer coefficient ($25\,\mathrm{W\,m^{-2}\,K^{-1}}$) prevents any major changes in zone temperature. Note that the steady state condition is typically considered when there is no significant change in the product mole fractions. In the current study, the steady state condition is reached at approximately 10 s.

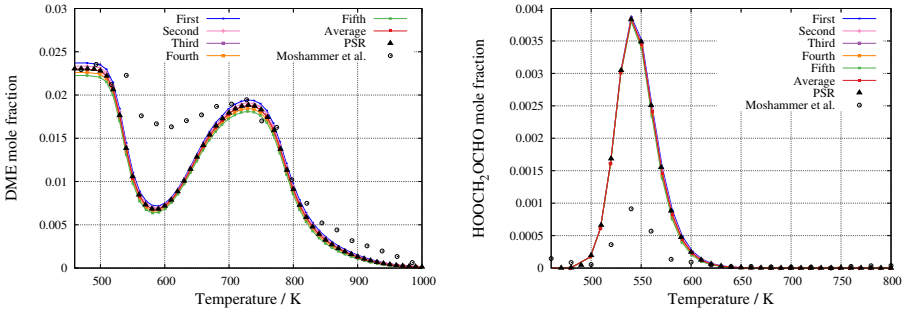

(a) (b)

Figure 9.1: Mole fraction profiles of (a)DME and (b)$HOOCH_2OCHO$ over the initial temperature of the JSR considering inhomogeneous distribution of the initial mole fraction of the reactants (4% difference of the reactant mole fractions between nearby zones)

Figure 9.1 compares the mole fraction profiles of the main species of DME and the intermediate species of keto-hydroperoxide or HMPF ($HOOCH_2OCHO$) during the oxidation of DME over the initial temperature using the multi-zone model to the PSR approach and the experimental results (Moshammer *et al.* 2016). The main conclusions of this section are summarized below.

- The deviations between the zones are quite small, representing the lower sensitivity of the products to the inhomogeneous mole fraction distribution. More specifically, the largest deviation of DME mole fraction between the first and the fifth zone ($\frac{X_{DME,5}-X_{DME,1}}{X_{DME,1}}$) reaches 6%. However, the sensitivity of some products is higher at certain temperatures, such as the mole fraction of H_2O and the mole fraction C_2H_6 over the temperature ranges from 900 K to 1000 K as shown in Figs. A.1a and A.1d of Appendix A.1.

- The averaged DME mole fraction over five zones is almost identical to the PSR model due to the linear increase of the inflow mole fractions. Specifically, a change of 4% in the distribution of inflow mole fractions results in the largest deviation between the averaged DME mole fraction derived from the multi-zone model and the PSR model ($|X_{AV}\text{-}X_{PSR}|)/X_{PSR}$ at 800 K of about 0.05%. Thus, it can be concluded that the predicted product mole fractions during the oxidation of DME for the

case of inhomogeneous distribution of the initial mole fractions of the reactants cannot capture the imperfect mixing inside the JSRs and do not follow the experimental data from Ref. (Moshammer *et al.* 2016), because changing the initial values cannot significantly affect the steady state conditions.

9.2.1 *Studying mass exchange rate between zones*

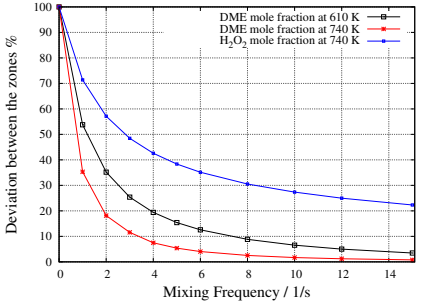

Figure 9.2: Deviation of the species mole fractions between zones over turbulent frequency

According to the developed multi-zone model in Section 4.3, the mixing exchange rates between the zones is a function of the mixing frequency. In order to study the effect of mass exchange rates on the multi-zone model, a parametric analysis of the mixing frequency is performed. The deviation in species mole fractions predicted by the zones is calculated as a function of turbulent frequency (in the range of zero to $15\,s^{-1}$), as shown in Fig. 9.2. The vertical axis represents the deviations in DME and H_2O_2 mole fractions between the first and the fifth using the multi-zone model divided by the predicted mole fraction with zero turbulent frequency (in percentage) ($X_{f_{mix},5}$-$X_{f_{mix},1}$)/($X_{(f_{mix}=0),5}$-$X_{(f_{mix}=0),1}$), where f_{mix} is the mixing frequency. As can be seen from Fig. 9.2, increasing the mixing frequency, which results in an increased mass exchange rate, leads to a reduced deviation between zones. To be more precise, insufficient mixing between zones causes all the zones to behave like several individual PSRs that are coupled by pressure and can have a different amount of initial reactant mole fractions, volumes, wall temperatures, and heat transfer coefficients. However, increasing the exchange rate (better mixing inside the JSR) leads to a decrease in the deviation between

the zones. Consequently, the deviation between the zones (from the first to the fifth zone) in the multi-zone model can be affected by the amount of exchange rate between zones.

9.2.2 *Numerical accuracy in terms of different number of zones*

To understand the effect of the number of zones on the multi-zone model, a nine-zone model is performed in the case of the inhomogeneous distribution of the initial mole fractions of the reactants. Table 9.3 compares the averaged value of the mole fractions of CO and DME for a five-zone and nine-zone model at the temperature of 710 K.

Table 9.3: Comparing the mole fraction of the products of DME oxidation using a 5- and 9-zone model

Number of zones	X_{CO}	X_{DME}
9-zone	0.0029958	0.018312
5-zone	0.0030008	0.018301

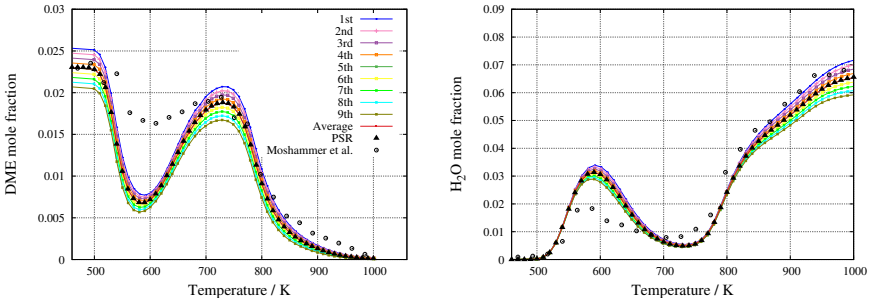

(a) (b)

Figure 9.3: Mole fraction profiles of (a)DME and (b)H_2O over a nine-zone model

Later, the predicted mole fractions of DME and H_2O versus initial temperature are shown in Fig. 9.3a and 9.3b, respectively. By comparing Fig. 9.3 with Fig. 9.1 and referring to the results shown in Table 9.3, it can be concluded that the averaged product mole fractions during the oxidation of DME over nine zones predict values that are quite close to the averaged mole fraction using the five-zone

model. Therefore, the numerical accuracy for a 5-zone model would be sufficient for further investigation and can be used to represent the inhomogeneity within the JSR. Note that the previous study by Aceves *et al.* (2000) had already predicted such behavior and specified that only small differences exist between the results with higher zone numbers in the rapid-compression machine model.

9.3 CONSIDERING INHOMOGENEOUS VOLUME DISTRIBUTION

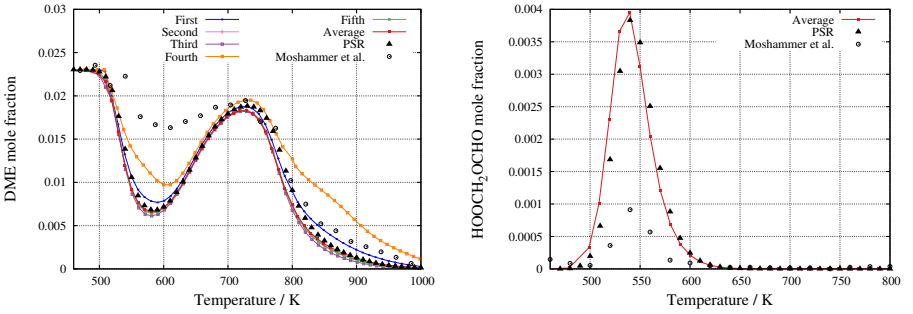

Figure 9.4: Mole fraction profiles of (a)DME and (b)$HOOCH_2OCHO$ over the initial temperature of the JSR considering inhomogeneous distribution of the total volume

Following the results of Chapters 6 and 7, stagnant regions (dead zones) are formed at the center of the JSR and in the conical region between the nozzles. Therefore, the flow moves at the slowest velocity in the dead zones, impairing perfect mixing within the reactor (Hu *et al.* 2021); however, more mass exchange takes place in the regions closer to the turbulent jets. In this section, the volume of each zone is considered to be different over the representative zones, while the sum of all the zones is equal to the total volume. The volume size from the first to the last zone changes as $V_1 = 0.1V_{\text{tot}}$, $V_2 = 0.24V_{\text{tot}}$, $V_3 = 0.35V_{\text{tot}}$, $V_4 = 0.05V_{\text{tot}}$, $V_5 = 0.26V_{\text{tot}}$. The initial mole fractions of all zones are identical to each other as $X_{\text{DME}} = 2.295$, $X_{\text{Ar}} = 78.097$, and $X_{\text{O}_2} = 19.607$. Moreover, initial temperature of the reactor remain nearly constant and equal to the wall temperature due to the assumption of a high heat transfer coefficient ($25\,\text{W}\,\text{m}^{-2}\,\text{K}^{-1}$). In addition, the inflow composition enters the JSR at the temperature of 350 K.

Figure 9.4 shows the species mole fraction profiles during the oxidation of DME and HMPF calculated by the multi-zone model, the PSR model, and measured by experiments (Moshammer *et al.* 2016). Note that in Fig. 9.4b only the averaged mole fraction of HMPF over five zones has been shown for better clarity. The most important conclusions of this section are listed in the following.

- The average value over five zones considering inhomogeneous distribution of total volume is very close to the PSR model. More specifically, changing the distribution of the total volume within the reactor (from the largest to the smallest zone (V_3/V_4)) seven times results in a 1.8% deviation of the average mole fraction of DME over five zones from the PSR model ($|X_{AV}\text{-}X_{PSR}|)/X_{PSR}$ at the temperature of 800 K. Therefore, the multi-zone model, which considers inhomogeneous distribution of volume in each zone, cannot capture the inhomogeneity inside the JSR and be a proper representative of the behavior of real JSRs and the experimental data (Moshammer *et al.* 2016).

- The zones contains the smallest and the largest volume, in a network of five zones deviate more from the PSR model and the experimental data (Moshammer *et al.* 2016), as shown in Fig. 9.4 and Fig. A.2 in Appendix A.2. The reason can be understood by the dependency of the mean residence time on the volume of each zone. That means each zone with a smaller volume has a shorter residence time compared to those with a larger volume with the consideration of the constant inflow mass rate in each zone. The calculated residence times from the first to the fifth zone follow these values, 2.01 s, 4.45 s, 6.54 s, 0.71 s and 4.84 s, respectively, while the average of the mean residence time for all five zones is 3.71 s in the temperature of 800 K.

- The zones with similar volume size predict similar mole fractions (see the second and fifth zones in Fig. 9.4a).

9.4 CONSIDERING NONUNIFORM DISTRIBUTION OF WALL TEMPERATURE

Following the experimental setup of the JSR (Moshammer *et al.* 2016), a temperature-controlled oven completely encloses the reactor to

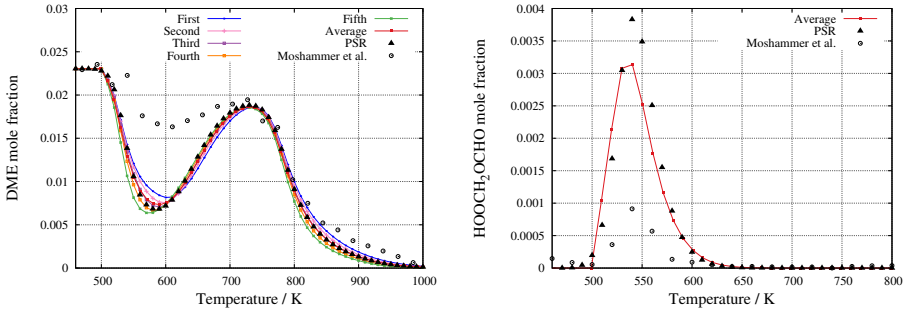

(a) (b)

Figure 9.5: Mole fraction profiles of (a)DME and (b)HMPF considering inhomogeneous distribution of the wall temperature over five zones

keep the gas temperature at the desired temperature. However, the temperatures measured by the thermocouple along the quartz nozzle monitored a temperature uncertainty of around $\pm 20\,\mathrm{K}$, as mentioned in Ref. (Rousso *et al.* 2018). Moreover, Moshammer *et al.* (2016) and Lignola and Reverchon (1986) reported a smaller value for the temperature uncertainty. Note that a small amount of uncertainty in temperature measurement has a significant impact on heat exchange evaluation (Lignola and Reverchon 1986). Therefore, in this section, to study the effect of nonuniform wall temperature on homogeneity, the temperature of the walls is arbitrarily distributed over five zones. In this section, the wall temperature is varied by 10 K from the first to the fifth zone with a mixing frequency of $1.2\,\mathrm{s}^{-1}$. The initial mole fraction of the reactants (equivalence ratio of 0.35), volume (0.2 V_{tot}), the heat transfer coefficient ($25\,\mathrm{W\,m^{-2}\,K^{-1}}$), and the inlet gas temperature of 350 K are assumed to be identical for all zones.

Figures 9.5 and A.3 in Appendix A.3 show the sensitivity of the main and intermediate species during the oxidation of DME, considering non-uniform distribution of the wall temperature. The species mole fractions using the multi-zone model considering nonuniform distribution of the wall temperature give important clues about the sensitivity of different species to temperatures; however, it cannot capture the inhomogeneity within the JSRs, since the averaged value of the species mole fraction coincides with the PSR model. As a result, the multi-zone model using an inhomogeneous distribution of

the wall temperature cannot capture the imperfect mixing inside the JSR.

9.5 STUDYING THE EFFECT OF HEAT TRANSFER COEFFICIENT USING SINGLE ZONE MODEL

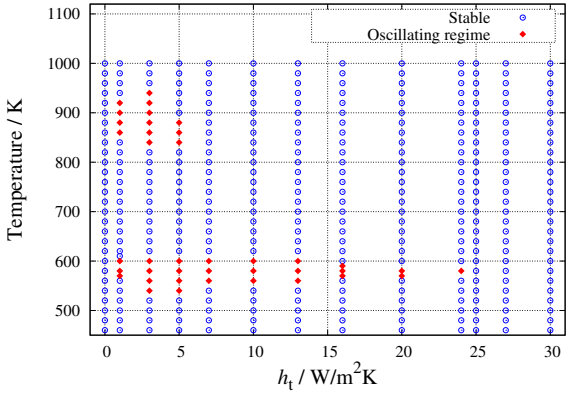

Figure 9.6: Stability diagram during the oxidation of DME dependent on heat transfer coefficient (h_t) and the initial temperature

In this section, the stability of the oxidization of DME is studied dependent on heat transfer coefficient (in the range of 0 - 30 $\mathrm{W\,m^{-2}\,K^{-1}}$) and initial temperature T_{init} (in the range of 460 - 1000 K), using the single zone model. The single zone model is a simplified form of the developed theoretical model in which the terms related to the mixing exchange between the zones are removed from the conservation equations of Eqs. 4.4 - 4.6. For all simulations in this section, the inlet mixture temperature of 350 K is considered. The stability diagram in Fig. 9.6 gives an overview of the stable combustion (blue points) and the oscillations (red points) in the studied JSR. The stability diagram using the single zone model predicts stable combustion during the oxidation of DME in two extreme cases of zero and large heat transfer coefficients ($h_t \geq 25\,\mathrm{W\,m^{-2}\,K^{-1}}$). Indeed, the assumption of a large heat transfer coefficient follows the isothermal perfectly stirred reactor model and therefore predicts stable ignition. Furthermore, when no heat transfer to the walls is considered, the model predicts three different stable combustion regimes, which are discussed in detail in Subsection 9.5.1.

The single zone model predicts low- and high-temperature oscillations for the intermediate heat transfer coefficients (see the red points, representing the low-temperature oscillations in the range of 560 - 610 K and high-temperature oscillations in the range of 820 - 940 K, respectively, in Fig. 9.6). These oscillations were already predicted by the work of Stoehr *et al.* (2015) and Lammersen *et al.* (2013). The high-temperature oscillations are damped at lower heat transfer rates (above $6\,\mathrm{W\,m^{-2}\,K^{-1}}$) in the steady state, but the low-temperature oscillations persist within the JSR (Stoehr *et al.* 2015). The source of the low-temperature oscillations is related to the thermokinetic process of the DME oxidation, since changing the heat transfer coefficient has minimal impact on the oscillations (Stoehr *et al.* 2015). According to the study of Stoehr *et al.* (2015), the formation and consumption of semi-stable intermediate species (such as hydroperoxymethyl formate (HMPF), OH, and formaldehyde) drive the low-temperature oscillations. More details are given in Subsection 9.5.2. Furthermore, the origin of the high-temperature oscillations can be attributed to the initial conditions of the mixture; a fresh inlet gas with a temperature of 350 K enters the JSR, while the initial temperature of the JSR is in the range of 460 - 1000 K. At the same time, the heat of reaction increases the temperature of the mixture, and the heat transfer occurs between the mixture and the walls. The interaction of these three factors (inlet temperature of 350 K, heat of reaction, and heat exchange with the reactor walls), induces oscillations at the higher temperature (in the range of 820 - 940 K).

9.5.1 *Cases of zero and large heat transfer coefficients*

The product mole fractions during the oxidation of DME using the single zone model in two extreme cases of zero and large heat transfer coefficients ($25\,\mathrm{W\,m^{-2}\,K^{-1}}$) over the initial temperature (T_{init}) are compared with the experimental data (Moshammer *et al.* 2016) and the PSR model in Fig. 9.7. The single zone model, which assumes no heat exchange with the walls ($h_t = 0\,\mathrm{W\,m^{-2}\,K^{-1}}$), predicts three distinct ignition behaviors for the studied PSR depending on the initial temperature: no ignition, intermediate ignition (partial oxidation of DME), and full ignition of the mixture (Fully oxidized DME).

At the lower initial temperatures, the oxidation of DME results in no temperature rise, no consumption of reactants, and consequently,

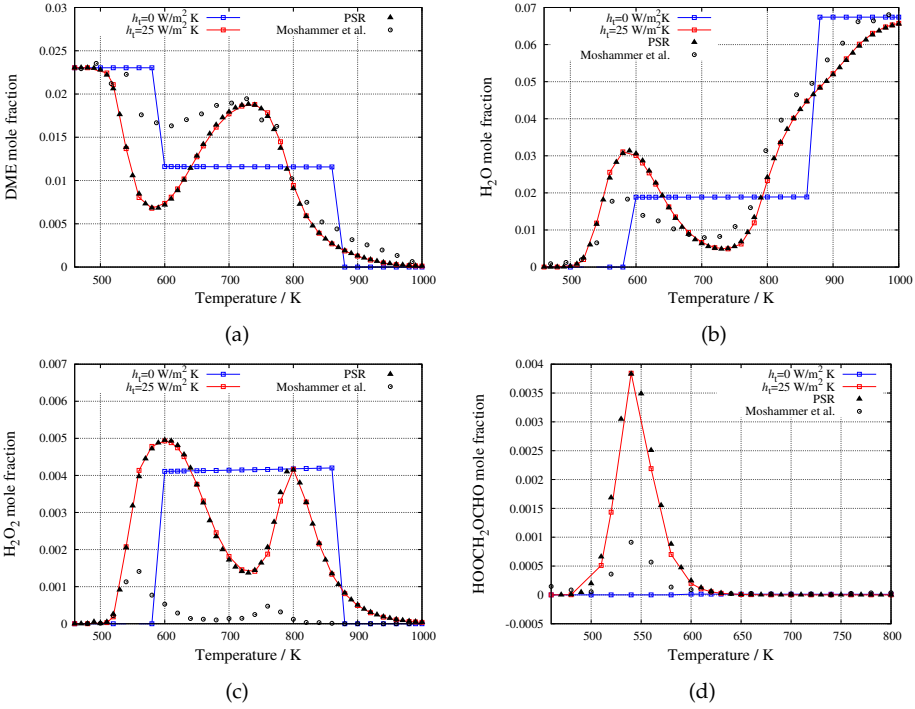

Figure 9.7: Mole fraction profiles of (a)DME, (b)H_2O, (c)H_2O_2, and (d)HMPF over the initial temperature of the JSR: Comparison of the single zone model, considering the heat transfer coefficient of $0\,W\,m^{-2}\,K^{-1}$ (blue curve) and $25\,W\,m^{-2}\,K^{-1}$ (red curve) with the previous experimental study (Moshammer *et al.* 2016) and the PSR model

the absence of the product species formation (see species mole fractions in the temperature range of 460-580 K in Fig. 9.7).

Further increase of T_{init} results in the partial ignition of the mixture and the formation of some intermediate species (such as H_2O_2 mole fraction in the temperature range of 590-880 K as shown in Fig. 9.7c and CO mole fraction in Fig. A.4a in Appendix A.4. In this regime, 50% of the initial fuel (DME) is consumed and the rest leaves the reactor without reacting (Lammersen *et al.* 2013). This happens because the equilibrium temperature of the mixture reaches 640 K, which prevents the DME from becoming fully consumed.

Subsequent increase in the initial temperature leads to the complete oxidation of DME and the increased formation of product species

(see the temperature range of 880-1000 K of the single zone model in Fig. 9.7). As predicted by the single zone model, the entire DME is consumed, and the equilibrium temperature of the mixture reaches 1535 K in the steady state.

The predicted product mole fractions by the single zone model, considering a large heat exchange with the walls ($h_t = 25\,\mathrm{W\,m^{-2}\,K^{-1}}$), coincide with the predicted mole fraction by the PSR model. Indeed, assuming a high heat transfer coefficient, the heat of the reaction transfers to the surroundings and the gas temperature approaches the wall temperature. As a result, the mole fractions of the product are very similar to those obtained by an isothermal perfectly stirred reactor model.

9.5.2 *Case of the heat transfer coefficients of* $3\,\mathrm{W\,m^{-2}\,K^{-1}}$

As shown in the stability diagram in Fig. 9.6, the single zone model with the heat transfer coefficient between zero and $25\,\mathrm{W\,m^{-2}\,K^{-1}}$ predicts temperature oscillations, which are consistent with the earlier studies (Stoehr *et al.* 2015, Lammersen *et al.* 2013). This subsection studies the ignition behavior of the oxidation of DME considering the heat transfer coefficient of $3.0\,\mathrm{W\,m^{-2}\,K^{-1}}$. Figure 9.8 shows the mole fraction profiles in the lowest (min) and highest (max) values of the species oscillations. The ignition process of DME considering the heat transfer coefficient of $3.0\,\mathrm{W\,m^{-2}\,K^{-1}}$ is divided into five regimes depending on the initial temperature (Lammersen *et al.* 2013, Wada *et al.* 2009). These regimes and the main conclusions are summarized as follows.

- When the initial temperature of the JSR is low (in the range of 460 - 530 K), no reaction of the mixture takes place, and no products are generated (1$^{\mathrm{st}}$ regime). Further rise of T_{init} results in an oscillating behavior of temperature and the species mole fraction, where the gas mixture in the JSR periodically ignites and quenches (low- temperature oscillations, 2$^{\mathrm{nd}}$ regime), as can be seen in the temperature range of 540 - 610 K in Fig. 9.8. Further increase of the initial temperature leads to a stable combustion (3$^{\mathrm{rd}}$ regime) (see the temperature range of 620 - 800 K). Subsequent increase of the initial temperature to a higher value leads to the high-temperature oscillations (4$^{\mathrm{th}}$ regime), as shown in the temperature range of 820 - 950 K. A

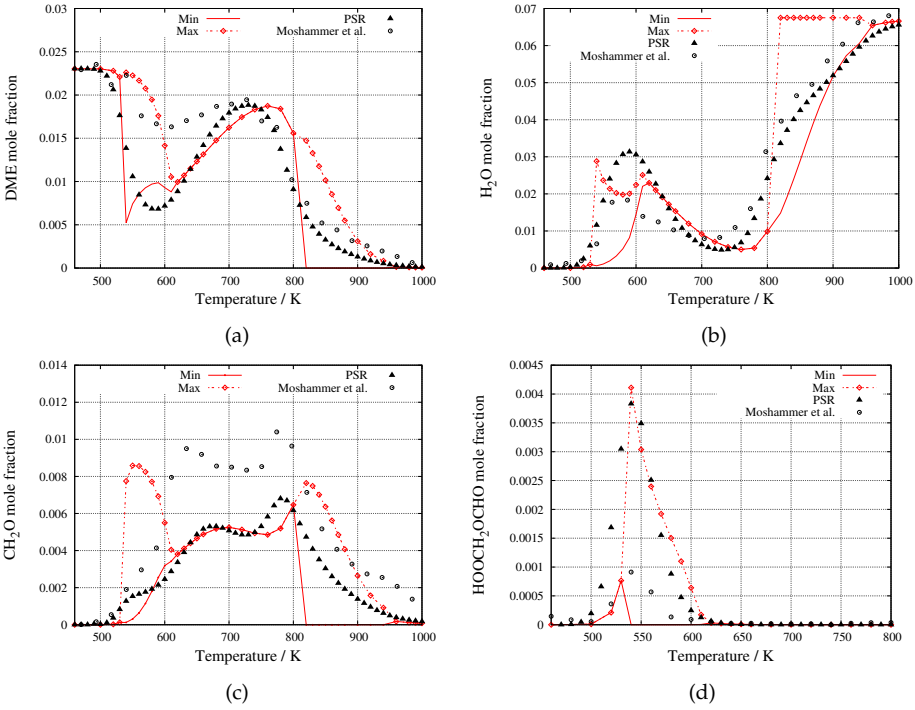

Figure 9.8: Mole fraction profiles of (a)DME, (b)H_2O, (c)CH_2O, and (d)HMPF over the initial temperature of the JSR: Comparison of the single zone model, (considering minimum and maximum value of the species) at the heat transfer coefficient of $3\,W\,m^{-2}\,K^{-1}$ with the previous experimental study (Moshammer *et al.* 2016) and the PSR model

further increase of T_{init} leads to a stable combustion again (5^{th} regime) (see the temperature range of 960 - 1000 K in Fig. 9.8).

- The origin of the low-temperature oscillations in the second regime is related to the formation of HPMF (Stoehr *et al.* 2015), which is formed only at the lower temperatures (see Fig. 9.8d). Furthermore, the formation of formaldehyde (CH_2O) not only increases the temperature, but also acts as an inhibitor for the reaction (Stoehr *et al.* 2015) that leads to a decrease in temperature. Therefore, temperature oscillations are generated at the lower initial temperatures.

- The oscillations at higher temperatures (4^{th} regime) are related to the interaction of three main parameters; 1) a fresh inflow gas with a temperature of 350 K enters the JSR, 2) heat transfers between the mixture and the walls with a constant heat transfer coefficient, 3) the heat of the reaction increases the temperature of the mixture inside the JSR.

- The measured mole fractions of the species by Moshammer *et al.* (2016) are in the range between the lowest and highest oscillations of the species mole fractions predicted by the single zone. This is particularly evident in the case of DME and H_2O mole fractions in the temperature range of 540 - 600 K and 820 - 900 K in Fig. 9.8.

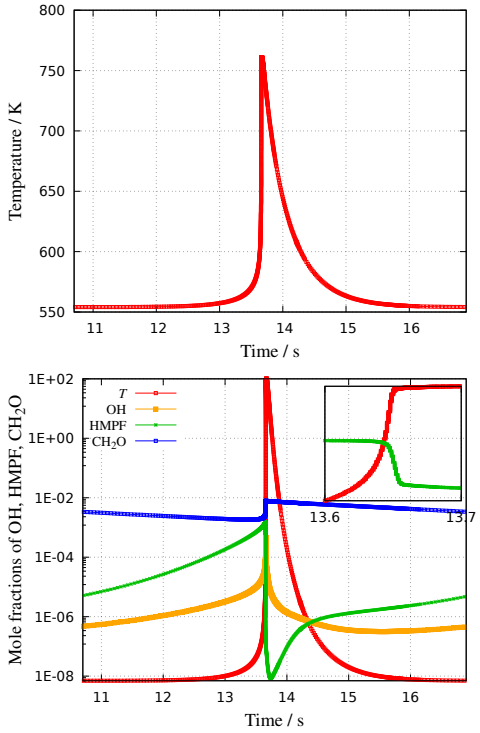

Figure 9.9: Temporal evolution of the gas temperature over one cycle of the oscillations and product mole fractions at an initial temperature of 580 K and a heat transfer coefficient of 3 $W\,m^{-2}\,K^{-1}$

A detailed investigation of the gas temperature and product mole fractions over a cycle provides valuable insights into the underlying mechanisms of low-temperature oscillations within the JSRs. As can be seen from Fig. 9.9, the rates of formation and consumption of product species are different over a cycle of temperature oscillations. The oxidation of DME leads to the production of a large amount of the semi-stable species of HMPF ($HOOCH_2OCHO$). Producing HMPF leads to an increase in the temperature (Stoehr *et al.* 2015). Then, HMPF dissociates suddenly as the temperature reaches around 700 K and provides OH, as shown in the magnified part of Fig. 9.9 (Stoehr *et al.* 2015). After that, the remaining of produced OH and the chain branching lead to the production of CH_2O. The generated formaldehyde (CH_2O) consumes the chain branching radical OH, leading to the further temperature increase up to the temperature of 760 K, as previously predicted by Stoehr *et al.* (2015). The remaining CH_2O acts as a chemical inhibitor and inhibits the further combustion, resulting in a decrease in temperature (reaching the temperature of 580 K). Then the fresh inlet gas enters the reactor again, and the entire cycle is repeated. Finally, it can be concluded that the formation of HMPF and CH_2O during the low temperature oxidation of DME induces temperature oscillations within the reactor.

9.6 CONSIDERING NONUNIFORM DISTRIBUTION OF HEAT TRANSFER COEFFICIENT

Following the construction of the JSR described in Chapter 2, the JSR vessel is located in an oven to adjust the operating temperature for studying the oxidation of DME. Adjustment of the reactor to the temperature of the oven introduces inhomogeneity within the JSR.

This means that the regions inside the JSR, where a fresh inflow enters, have a different amount of heat transfer compared to zones near the walls. Therefore, employing the single zone model cannot represent the conditions exits in the real JSR. In this section, the ignition of DME is studied using the multi-zone model considering different values of the heat transfer coefficients over five representative zones.

Following the gas heat transfer correlation based on the Nusselt number (Lignola and Reverchon 1988), the heat transfer coefficient for the studied JSR is calculated to be $3.28\,W\,m^{-2}\,K^{-1}$. Accordingly, the heat transfer coefficients are distributed differently

Table 9.4: Distribution of the heat transfer coefficients over five zones together with the average of the heat transfer coefficients (Average), their standard deviation (STD), and their deviation divided by the average (STD/Average)

	h_t / W m^{-2} K^{-1}					Over 5 zones		
Case	1st	2nd	3rd	4th	5th	Average	STD	STD/Average
1	0.1	0.7	1.0	5.0	9.6	3.28	4.03	1.22
2	2.0	2.8	3.2	4.0	4.4	3.28	0.95	0.29

over the five zones in two cases, with the same averaged value of the heat transfer coefficients and different amount of deviations between the zones, as can be seen in Table 9.4. Furthermore, the initial temperature of the gas and the wall temperature are assumed to be identical. The inflow gas temperature of 350 K, the initial mole fraction of the reactants (equivalence ratio of 0.35), and the volume size ($V = 0.2V_{tot}$) are kept identical for all zones.

As discussed in Subsection 9.5.2, the oscillations were captured in the temperature range of 540 - 610 K and 820 - 960 K, therefore, the species mole fractions during the DME oxidation were studied in the low- and high temperature regimes using the multi-zone model, as shown in Fig. 9.10.

Comparing the mole fraction profile of the main and intermediate species in cases 1 and 2 with the experimental data and the PSR model in Fig. 9.10 shows a good agreement between the developed model and the experiments. Indeed, the multi-zone model accurately predicts the temperature and mole fraction oscillations within the JSR by defining different zones that exchange mass and heat with each other, a factor neglected by the PSR model. Furthermore, defining larger deviations between the zones (case 1) leads to a more accurate estimation of the experimental data compared to case 2. This is because deviations in the heat transfer coefficients between the zones reflect the real conditions within the studied JSR.

Consequently, the developed multi-zone model in this study considering inhomogeneous distribution of the heat transfer coefficient successfully predicts the temperature oscillations and the product mole fraction profile during the oxidation of DME.

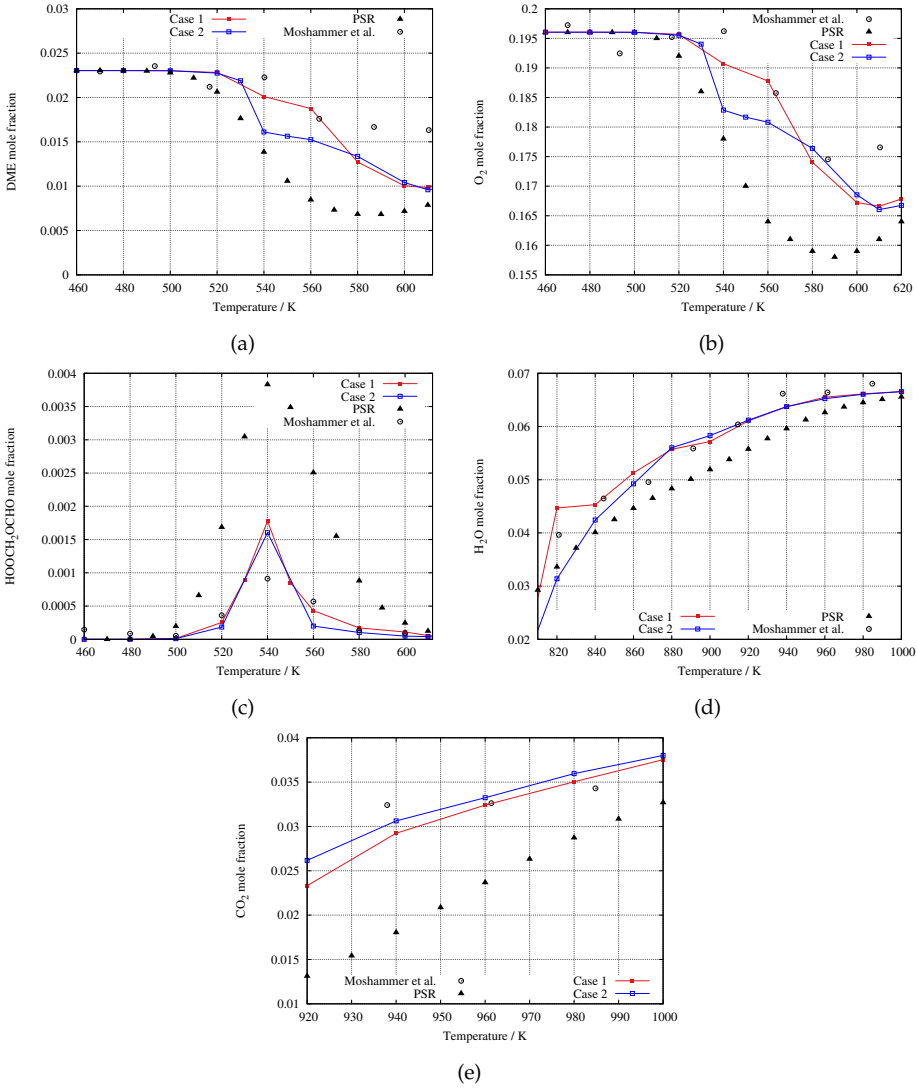

Figure 9.10: Profiles of the averaged mole fractions of (a)DME, (b)O2, (c)HMPF over five zones in the low-temperature regime and (d)H_2O, (e)CO_2 in the high-temperature regime considering different heat transfer coefficients (Cases 1 and 2)

9.7 CONCLUSIONS

In order to capture the inhomogeneity inside the real JSRs, a zero-dimensional multi-zone model is applied to the oxidation of DME.

In this model, the total volume of the JSR is divided into a number of representative zones, in which all scalar fields are assumed to be uniform. However, thermodynamic variables (except pressure), mixture composition, and turbulence characteristics may vary from one zone to the next. As a result, each zone exchanges mass and heat with the other zones, as defined in the model.

It is concluded that the selection of an appropriate mixing exchange rate between zones, representing the intensity of mixing, is crucial for modeling inhomogeneity and accurately estimating the behavior of the real reactor. Moreover, the results show that the inhomogeneous distribution of the heat transfer coefficients more accurately represents the non-perfectly mixed JSR compared to the case of the inhomogeneous distribution of the initial mole fraction of the reactants, the total volume, and the wall temperature. It also captures the product mole fractions during the oxidation of DME and the temperature oscillations predicted by the experimental studies (Moshammer *et al.* 2016, Stoehr *et al.* 2015).

As a result, it can be inferred that the multi-zone model with the consideration of the inhomogeneous distribution of the heat transfer coefficients can be employed to describe mixing characteristics in real JSRs.

10 IMPROVEMENT OF THE JSR DESIGN

The mixing performance was examined in a spherical JSR by analyzing the RTD, the distribution of the velocity field, the TKE and its dissipation in Chapters 6 and 7. According to these chapters, the dead spaces generated in the center of the spherical JSR and the short circulation of flow lead to imperfect mixing. Therefore, the JSR design that could improve the mixing and overcome the problems of dead zones and short circulation is still needed. To this end, the design of the reactor is modified by adding two nozzles to the standard four-nozzle design of the spherical JSR introduced by Dagaut *et al.* (1986) to improve the mixing quality. These two nozzles with an outer diameter of $d = 3\,\text{mm}$ and an inner diameter of $d = 1\,\text{mm}$ point the highly turbulent jets directly into the center of the JSR, eventually eliminating the dead zone. Figure 10.1 provides an overview of the simulated six-nozzle JSR design by OpenFOAM. As can be seen, nozzles G and H direct the flow straight to the center.

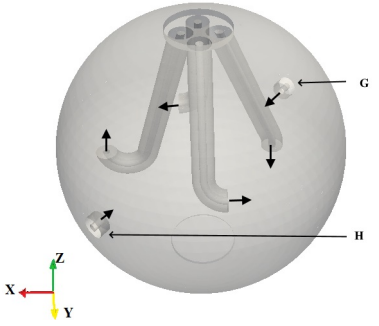

Figure 10.1: Proposed new design of the JSR with six nozzles: two additional nozzles (G and H) pointing to the center (Esmaeelzade *et al.* 2021)

To simulate the proposed JSR with six nozzles, approximately 1.2M cells were distributed within the reactor. Mesh refinement was focused particularly on the nozzle exits and walls to capture fine details of the flow. The detailed simulation setup and the boundary conditions were previously outlined in Section 5.1.

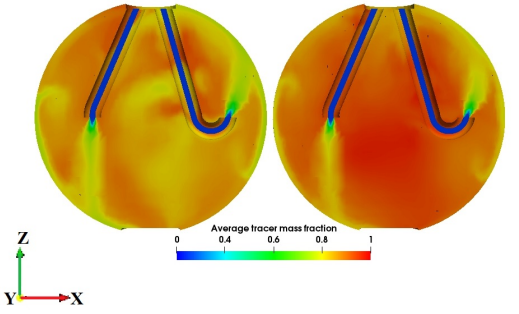

(a)

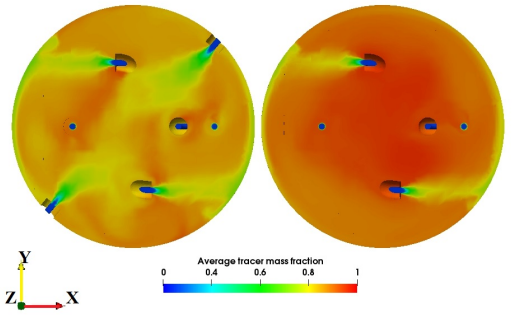

(b)

Figure 10.2: Time-averaged mass fraction of CO_2 in the cross-sections described by the (a) x-z plane, (b) x-y plane, (Left: Six-nozzles JSR, Right: Four-nozzles JSR) (Esmaeelzade *et al.* 2021)

Further, the time averaged CO_2 mass fraction is compared in the case of the six- (the left reactor) and four- (the right reactor) nozzle design over a cross-section on the x-z and x-y planes in Figs. 10.2a and 10.2b, respectively. A comparison of these two reactors reveals that two additional nozzles (nozzles G and H as shown in Fig. 10.1) effectively agitate the areas near the center and space between the inclined nozzles. Indeed, another circulating stream is created by two new applied jets, which influence the fluid contents in the center to flow; thus eliminating the formation of dead zones and the subsequent short circulating of the fluid elements. As a result, a six-nozzle JSR design produces a more homogeneous composition than a four-nozzle design in the same time interval.

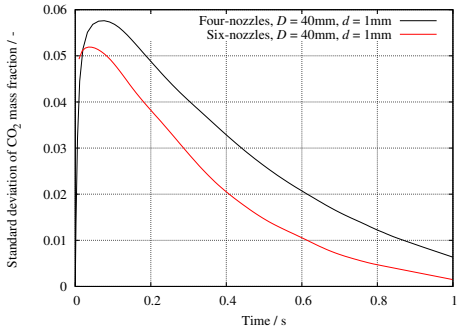

Figure 10.3: Temporal evolution of the standard deviation of the tracer mass fraction for the four- and six-nozzle designs (Esmaeelzade *et al.* 2021)

To quantitatively compare the mixing quality within the two setups of the JSR, the normalized weighted standard deviation of the CO_2 (tracer) mass fraction over time is shown for the cases of the standard four inclined nozzles and the proposed six-nozzle JSR design, as can be seen in Fig. 10.3. The predicted standard deviation of the tracer mass fraction for the six-nozzle design shows lower values over time compared to the four-nozzle case, which represents a more uniform and homogeneous composition.

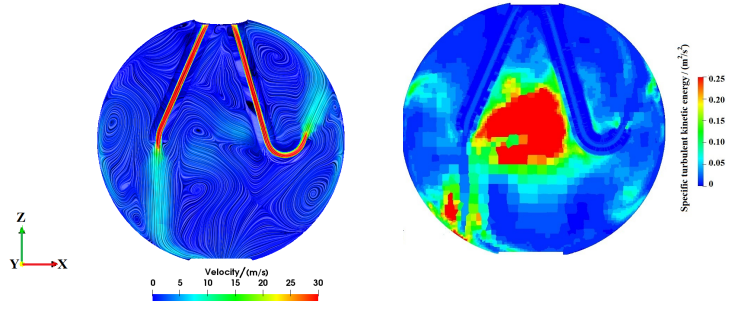

(a) (b)

Figure 10.4: Flow field resulting from the new JSR design consisting of six nozzles in the cross-section described by the x-z plane. (a) Time-averaged velocity vectors field; (b) Turbulent kinetic energy field

The reason for the lower values of the standard deviation of the tracer in the six-nozzle JSR can be explained by capturing the velocity field using the LIC technique and also TKE of the design of the six-nozzle JSR, as illustrated in Fig. 10.4a and 10.4b, respectively. According to Fig. 10.4a, several vortexes are created in the center of the chamber and between four inclined nozzles due to the highly turbulent flow issued by the two added nozzles. It is therefore expected that the mixing process inside the JSR will be intensified by these vortices, resulting in a more homogeneous composition. As can be seen from Fig. 10.4b, the TKE has higher values and the turbulent structures are significantly improved especially in the region close to the center of the JSR compared to the standard JSR with four-nozzle as shown in Fig. 7.6a.

11 SUMMARY AND OUTLOOK

The primary objective of this thesis has been the numerical analysis of the flow field inside a spherical JSR with four inclined nozzles. The results of this research work were divided into two parts. First, a detailed analysis of the flow characteristics within the mixing chamber and through the nozzles was presented using the CFD tools of OpenFOAM in Chapters 6-8. In this part, the LES-simulations of the tracer-decaying process of a non-reacting mixture within a 3-D configuration of the JSR setup were investigated. Subsequently, the mixing performance of a spherical JSR was examined considering different geometrical and thermodynamic conditions. The results showed that the numerically calculated RTD does not follow the residence time distribution for an ideal reactor and that turbulent structures are distributed nonuniform within the studied reactor. Thus, a homogeneous and perfectly mixed composition was not obtained for the simulated JSRs. According to the results of Chapters 6-8, the potential of the center of the JSR was identified as a source of the imperfect mixing within the reactor, due to the creation of the dead spaces.

Next, in order to capture the inhomogeneity inside the JSR, a zero-dimensional theoretical multi-zone model was developed and implemented in HOMREA in the second part. The developed model was applied to the oxidation process of DME in order to identify the source of the inhomogeneity within the JSR. For this purpose, various parameters such as the initial mole fraction of the reactants, the total volume, the wall temperature, and the heat transfer coefficients were distributed differently over five representative zones, as described in Chapter 9. Finally, it was concluded that the multi-zone model considering inhomogeneous distribution of the heat transfer coefficients over representative zones can capture imperfect mixing inside the JSR. Indeed, the developed model predicted the temperature oscillations and the product mole fraction profiles measured by the experimental studies of Moshammer *et al.* (2016) and Stoehr *et al.* (2015).

At the end, in order to improve the mixing quality and eliminate the dead spaces and short circulation of flow inside the standard

JSR with four inclined nozzles, an alternative JSR design with six nozzles (two of the jets pointing to the JSR center) was proposed in Chapter 10.

The main contributions of this work are summarized briefly below.

- Capturing the normalized RTD curve for the studied JSR and comparing it with the ideal reactor shows that the larger deviation at the earlier time and the long tail of the RTD curve at longer times represent the short circulating (bypassing process) and the dead (stagnant) zones within the JSR, respectively (Chapter 6).

- The importance of modeling the flow through the nozzles inside the JSR is emphasized in order to accurately capture the flow field. In fact, the modeling of the top-hat velocity profile at the entrance of the nozzle leads to a developed turbulent velocity profile at the exit of the nozzle.

- The interaction of two circumferential flows expanding towards the spherical walls causes poor mixing in the center of the JSR chamber and in the space between the nozzles (Chapter 7).

- The analysis of the velocity field, the TKE and the $\mathcal{Q}$-criterion shows the potential of the regions coherent to the walls for the shear stress and of the regions slightly away from the walls and the nozzles for the vorticity (Chapter 7).

- Operating the spherical JSR at higher pressure leads to capturing more efficient mixing compared to the case of the ambient pressure (Chapter 8).

- Based on the theoretical multi-zone model, the choice of an appropriate mixing exchange rate between the zones, which represents the intensity of mixing, is essential for modeling the inhomogeneity and accurately estimating the behavior of the real reactor (Chapter 9).

- The developed theoretical multi-zone model considering the inhomogeneous distribution of the heat transfer coefficients represents the imperfect mixing and inhomogeneity within the non-ideal JSR.

- The mixing performance of the common spherical JSR design with four inclined nozzles can be improved by adding two nozzles that direct the flow to the center of the reactor (Chapter 10).

Although this work involved a comprehensive investigation into the simulation of the JSR, some of the ideas and works can be retained for future work. The following are some of the suggestions.

- The CFD simulation of a non-reacting flow is investigated in the current study. However, the addition of a reacting mixture to a 3-D simulated JSR can provide valuable information on the chemical mechanisms and defects of the JSRs.
- The effect of the curvature of the JSR nozzles on the mixing quality can be investigated.
- An experimental setup of the spherical JSR with six nozzles directed towards the center of the JSR can be constructed for further comparison with the numerical analyses presented in this study.
- Capturing the homogeneity within the spherical JSR could be a motivation for future stochastic modeling based on the Probability Density Function (PDF) approaches and also compared to the multi-zone developed in this study.
- The developed multi-zone model for the JSR can be applied to other chemical mechanisms.

Part IV

APPENDIX

A

A.1 CONSIDERING NONUNIFORM DISTRIBUTION OF MOLE FRACTION

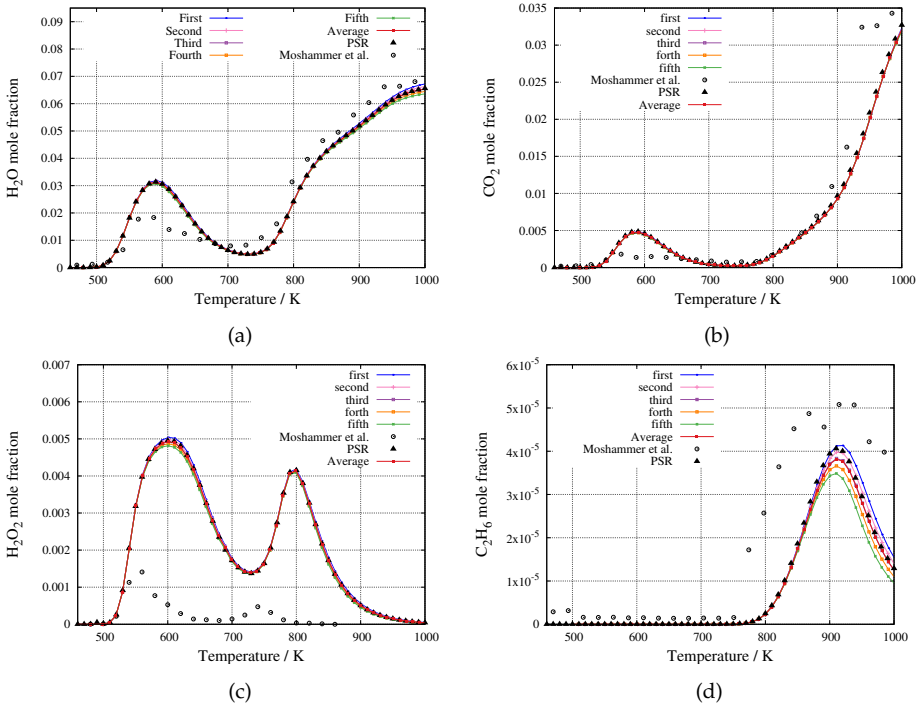

Figure A.1: Mole fraction profiles of the main and intermediate species during the oxidation of DME considering inhomogeneous distribution of reactants mole fractions

A.2 CONSIDERING NONUNIFORM DISTRIBUTION OF THE VOLUME

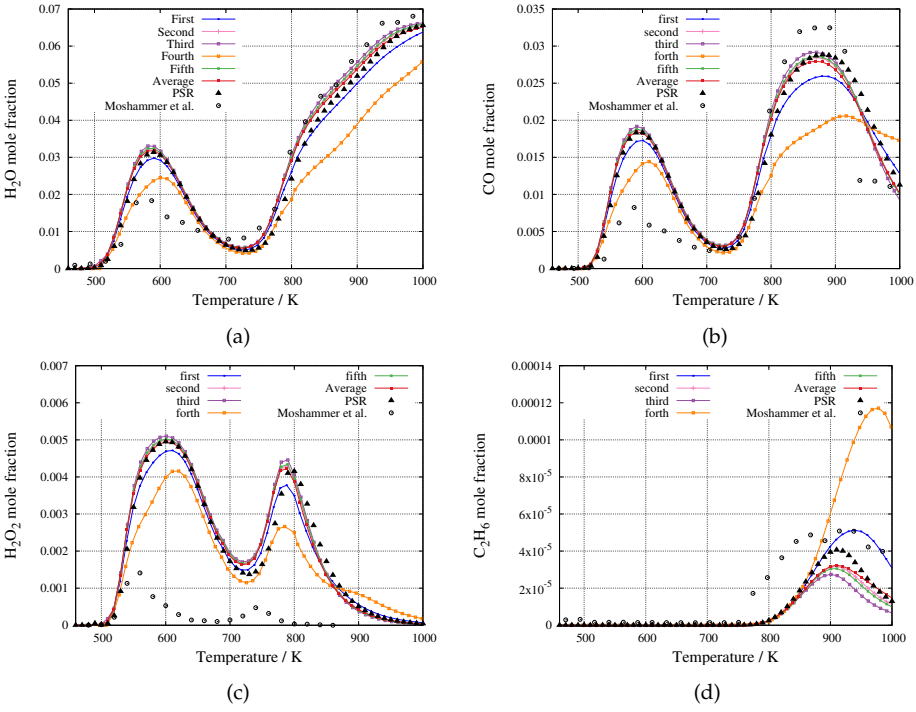

Figure A.2: Mole fraction profiles of the main and intermediate species during the oxidation of DME considering inhomogeneous distribution of the total volume

A.3 CONSIDERING NONUNIFORM DISTRIBUTION OF THE WALL TEMPERATURE

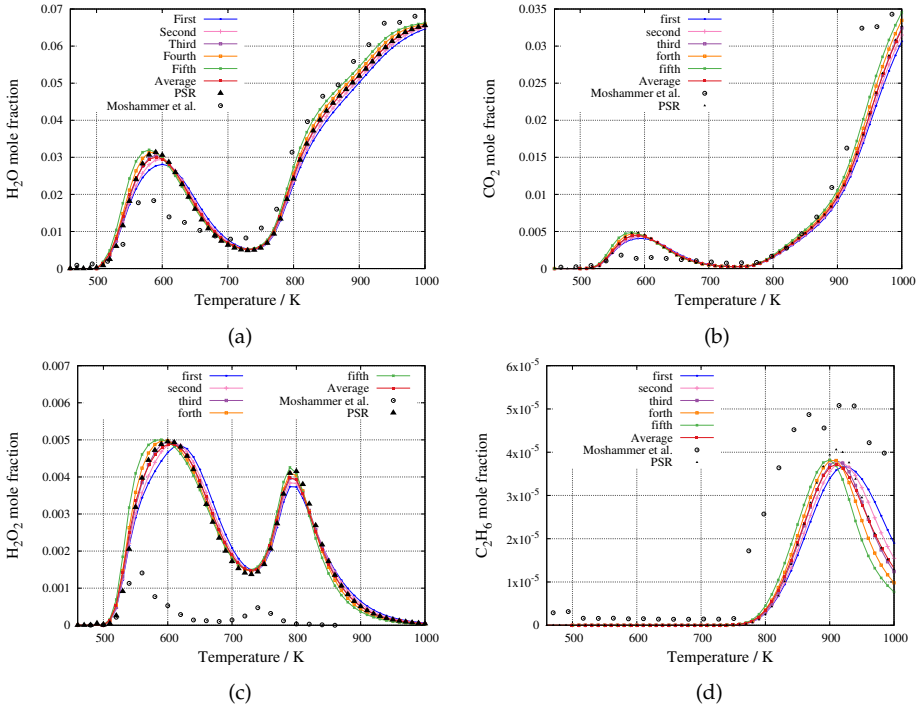

Figure A.3: Mole fraction profiles of the main and intermediate species during the oxidation of DME considering inhomogeneous distribution of the wall temperature

A.4 CONSIDERING NONUNIFORM DISTRIBUTION OF THE HEAT TRANSFER COEFFICIENT

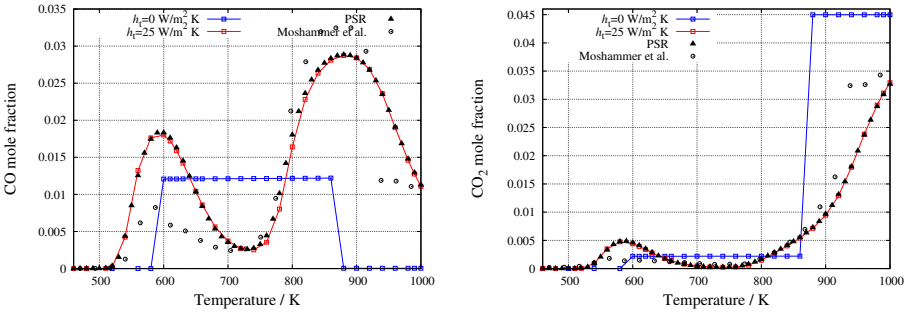

(a) (b)

Figure A.4: Mole fraction profiles of the products species during the oxidation of DME considering the inhomogeneous heat transfer coefficients of zero and 25 $\mathrm{W\,m^{-2}\,K^{-1}}$

BIBLIOGRAPHY

Abdalla, A., Bradley, D., Chin, S., and Choi, L., 1982. Temperature fluctuations in a jet-stirred reactor and modelling implications, *Proc. Combust. Inst.*, 19 (1), 495–502.

Aceves, S., Flowers, D., Westbrook, C.K., Smith, J., Pitz, W., Dibble, R., Christensen, M., and Johansson, B., 2000. A multi-zone model for prediction of HCCI combustion and emissions, *SAE Transact.*, 1, 431–441.

Al-Rafai, W., Tridimas, Y., and Woolley, N., 1990. A study of turbulent flows in pipe bends, *Proc. Inst. Mech. Eng., Part C*, 204 (6), 399–408.

Andreatta, D.A., 1995. *The use of reformed natural gas as a fuel for reciprocating engines*, Ph.D. thesis, University of California, USA.

Andreopoulos, Y. and Honkan, A., 1996. Experimental techniques for highly resolved measurements of rotation, strain and dissipation-rate tensors in turbulent flows, *Meas. Sci. Technol.*, 7 (10), 1462–1476.

Annand, W., 1963. Heat transfer in the cylinders of reciprocating internal combustion engines, *Proc. Inst. Mech. Eng.*, 177 (1), 973–996.

Arcoumanis, C., Bae, C., Crookes, R., and Kinoshita, E., 2008. The potential of di-methyl ether (DME) as an alternative fuel for compression-ignition engines: A review, *Fuel*, 87 (7), 1014–1030.

Ayass, W., 2013. Mixing in jet-stirred reactors with different geometries, Master thesis, King Abdullah University of Science and Technology, Saudi Arabia.

Ayass, W., Nasir, E., Farooq, A., and Sarathy, S., 2016. Mixing-structure relationship in jet-stirred reactors, *Chem. Eng. Res. Des.*, 111, 461–464.

Azay, P. and Côme, G., 1979. Temperature gradients in a continuous flow stirred tank reactor, *Ind. Eng. Chem. Process Des. Dev.*, 18 (4), 754–756.

Battin-Leclerc, F., 2008. Detailed chemical kinetic models for the low-temperature combustion of hydrocarbons with application to gasoline and diesel fuel surrogates, *Prog. Energy Combust. Sci.*, 34 (4), 440–498.

Bertolini, E., Pieringer, P., and Sanz, W., 2021. Effect of different subgrid-scale models and inflow turbulence conditions on the boundary layer transition in a transonic linear turbine cascade, *Int. J. Turbomach. Propuls.*, 6 (3), 35.

Bissoli, M., Frassoldati, A., Cuoci, A., Ranzi, E., Mehl, M., and Faravelli, T., 2016. A new predictive multi-zone model for HCCI engine combustion, *Appl. Energy*, 178, 826–843.

Boite, Y., Suaiden Klein, T., de Andrade Medronho, R., and Wajnberg, E., 2023. Numerical simulation of flow-diverting stent: Comparison between branches in bifurcation brain aneurysm, *Biomech. Model Mechan.*, 22, 1801–1814.

Bose, S., Moin, P., and You, D., 2010. Grid-independent large-eddy simulation using explicit filtering, *Phys. Fluids*, 22 (10), 105103.

Brown, N., Revzan, K., and Frenklach, M., 1998. Detailed kinetic modeling of soot formation in ethylene/air mixtures reacting in a perfectly stirred reactor, *in: Symposium (International) on Combustion, Pittsburgh, USA*, vol. 27, 1573–1580.

Brown, T.L., LeMay, H.E., and Bursten, B.E., 2002. *Chemistry: the central science*, New Jersey : Prentice Hall.

Burke, U., Pitz, W., and Curran, H., 2015a. Experimental and kinetic modeling study of the shock tube ignition of a large oxygenated fuel: Tri-propylene glycol mono-methyl ether, *Combust. Flame*, 162 (7), 2916–2927.

Burke, U., Somers, K., O'Toole, P., Zinner, C., Marquet, N., Bourque, G., Petersen, E., Metcalfe, W., Serinyel, Z., and Curran, H., 2015b. An ignition delay and kinetic modeling study of methane, dimethyl ether, and their mixtures at high pressures, *Combust. Flame*, 162 (2), 315–330.

Cabral, B. and Leedom, L., 1993. Imaging vector fields using line integral convolution, *in: Annual conference on Computer graphics and interactive techniques, Anaheim CA, USA*, 263–270.

Cantwell, B., 1981. Organized motion in turbulent flow, *Annu. Rev. Fluid Mech.*, 13 (1), 457–515.

Cavaliere, A., Ciajolo, A., D'anna, A., Mercogliano, R., and Ragucci, R., 1993. Autoignition of n-heptane and n-tetradecane in engine-like conditions, *Combust. Flame*, 93 (3), 279–286.

Celik, I., Ghia, U., Roache, P., Freitas, C., Coleman, H., and Raad, P., 2008. Procedure for estimation and reporting of uncertainty due to discretization in CFD applications, *J. Fluid Eng-T ASME*, 130 (7), 78001–78004.

Celis, C. and da Silva, L.F., 2015. Lagrangian mixing models for turbulent combustion: Review and prospects, *Flow Turbul. Combust.*, 94 (3), 643–689.

Cengel, Y., 2003. *Heat Transfer: A practical approach*, New York: McGraw-Hill.

Chen, J.Y., 1997. Stochastic modeling of partially stirred reactors, *Combust. Sci. Technol.*, 122 (1-6), 63–94.

Chong, M., Perry, A., and Cantwell, B., 1990. A general classification of three-dimensional flow fields, *Phys. Fluids A*, 2 (5), 765–777.

Cornell, R.E., Barbet, M.C., Lee, J., and Burke, M.P., 2022. NH_3 oxidation by NO_2 in a jet-stirred reactor: The effect of significant uncertainties in H_2NO kinetics, *Appl. Energy Combust. Sci.*, 12, 100095.

Corrigan, T. and Beavers, W., 1968. Dead space interaction in continuous stirred tank reactors, *Chem. Eng. Sci.*, 23 (9), 1003–1006.

Crawford, M., 2014. A computational study of mixing in jet stirred reactors, Master thesis, University of Akron, USA.

Curran, H.J., Dunphy, M.P., Simmie, J.M., Westbrook, C.K., and Pitz, W.J., 1992. Shock tube ignition of ethanol, isobutene and MTBE: Experiments and modeling, *Proc. Combust. Inst.*, 24 (1), 769–776.

Dagaut, P., Cathonnet, M., Rouan, J.P., Foulatier, R., Quilgars, A., Boettner, J.C., Gaillard, F., and James, H., 1986. A jet-stirred reactor for kinetic studies of homogeneous gas-phase reactions at pressures up to ten atmospheres ($\approx$ 1 mpa), *J. Phys. E: Sci. Instrum.*, 19 (3), 207.

Dagaut, P., Dayma, G., and Nicolle, A., 2005. Experimental and detailed chemical kinetic modeling study of the oxidation of hydrogen-enriched natural gas blends, *in: European Combustion Meeting (ECM), Louvain-la-Neuve, Belgium*.

Davani, A. and Ronney, P., 2017. A new jet-stirred reactor for chemical kinetics investigations, *in: National Combustion Meeting, Maryland, USA*.

David, R., Houzelot, J., and Villermaux, J., 1979. A novel and simple jet-stirred reactor for homogeneous and heterogeneous reactions with short residence times, *Chem. Eng. Sci.*, 34 (6), 867–876.

David, R. and Matras, D., 1975. Règies de construction et d'extrapolation des réacteurs auto-agités par jets gazeux, *Can. J. Chem. Eng.*, 53 (3), 297–300.

Davidson, D., Hong, Z., Pilla, G., Farooq, A., Cook, R., and Hanson, R., 2011. Multi-species time-history measurements during n-dodecane oxidation behind reflected shock waves, *Proc. Combust. Inst.*, 33 (1), 151–157.

Davis, M. and Davis, R., 2012. *Fundamentals of chemical reaction engineering*, New York: McGraw-Hill.

De Oliveria, L., De Toni, A.R., Cancino, L.R., Oliveira, A., Oliveira, E., and I., R.M., 2013. Computational fluid dynamics analysis of different geometries for a jet stirred reactor for fuel research, *in: International Congress of Mechanical Engineering, Ribeirao Preto, SP, Brazil*.

Denise, B., Sneeden, R., and Hamon, C., 1982. Hydrocondensation of carbon dioxide: IV, *J. Mol. Catal.*, 17 (2-3), 359–366.

Donovan, M., He, X., Zigler, B., Palmer, T., Wooldridge, M., and Atreya, A., 2004. Demonstration of a free-piston rapid compression facility for the study of high temperature combustion phenomena, *Combust. Flame*, 137 (3), 351–365.

Drost, S., Schießl, R., Werler, M., Sommerer, J., and Maas, U., 2019. Ignition delay times of polyoxymethylene dimethyl ether fuels (OME_2 and OME_3) and air: Measurements in a rapid compression machine, *Fuel*, 258, 116070.

Dryer, F., Haas, F., Santner, J., Farouk, T., and Chaos, M., 2014. Interpreting chemical kinetics from complex reaction–advection–diffusion systems: Modeling of flow reactors and related experiments, *Prog. Energy Combust. Sci.*, 44, 19–39.

Dubreuil, A., Foucher, F., Mouna1, C., Dayma, G., Dagaut, P., *et al.*, 2007. HCCI combustion: Effect of NO in EGR, *Proc. Combust. Inst*, 31 (2), 2879–2886.

Düz, H., 2019. Numerical and experimental study to predict the entrance length in pipe flows, *J. Appl. Fluid Mech.*, 12 (1), 155–164.

Esmaeelzade, G., Moshammer, K., Fernandes, R., Markus, D., and Grosshans, H., 2019. Numerical study of the mixing inside a jet stirred reactor using large eddy simulations, *Flow Turbul. Combust.*, 102 (2), 331–343.

Esmaeelzade, G., Moshammer, K., Markus, D., Maas, U., and Grosshans, H., 2021. Parametrical investigation for the optimization of spherical jet-stirred reactors design using large eddy simulations, *SN Appl. Sci.*, 3 (9), 1–15.

Fellouah, H., Ball, C., and Pollard, A., 2009. Reynolds number effects within the development region of a turbulent round free jet, *Int. J. Heat Mass Transf.*, 52 (17-18), 3943–3954.

Fischer, S., Dryer, F., and Curran, H., 2000. The reaction kinetics of dimethyl ether. I: High-temperature pyrolysis and oxidation in flow reactors, *Int. J. Chem. Kinet.*, 32 (12), 713–740.

Fogler, H., 1999. *Elements of chemical reaction engineering*, New Jersey: Prentice Hall.

Froehlich, J. and Rodi, W., 2000. Introduction to large eddy simulation of turbulent flows, *in: Closure Strategies for Turbulent and Transitional Flows*, Cambridge: Cambridge University Press, 267–298.

Fureby, C., Tabor, G., Weller, H., and Gosman, A., 1997. A comparative study of subgrid scale models in homogeneous isotropic turbulence, *Phys. Fluids*, 9 (5), 1416–1429.

Germano, M., Piomelli, U., Moin, P., and Cabot, W., 1991. A dynamic subgrid-scale eddy viscosity model, *Phys. Fluids*, 3 (7), 1760–1765.

Gil, I. and Mocek, P., 2012. CFD analysis of mixing intensity in jet stirred reactors, *Chem. Process Eng.*, 33 (3), 397–410.

Gisen, D., 2014. Generation of a 3D mesh using snappyHexMesh featuring anisotropic refinement and near-wall layers, *in: Proceedings of the 11th International Conference on Hydroscience & Engineering (ICHE), Hamburg, Germany*, 983–990.

Glarborg, P., Kee, R.J., Grcar, J.F., and Miller, J.A., 1986. *PSR: A FORTRAN Program for Modeling Well-Stirred Reactors*, vol. 46, California: Sandia National Laboratories Livermore.

Glaude, P., Herbinet, O., Bax, S., Biet, J., Warth, V., and Battin-Leclerc, F., 2010. Modeling of the oxidation of methyl esters - Validation for methyl hexanoate, methyl heptanoate, and methyl decanoate in a jet-stirred reactor, *Combust. Flame*, 157 (11), 2035–2050.

Goldsborough, S., Hochgreb, S., Vanhove, G., Wooldridge, M., Curran, H., and Sung, C., 2017. Advances in rapid compression machine studies of low-and intermediate-temperature autoignition phenomena, *Prog. Energy Combust. Sci.*, 63, 1–78.

Grosshans, H. and Papalexandris, M., 2017. Direct numerical simulation of triboelectric charging in particle-laden turbulent channel flows, *J. Fluid Mech.*, 818, 465–491.

Herbinet, O. and Battin-Leclerc, F., 2014. Progress in understanding low-temperature organic compound oxidation using a jet-stirred reactor, *Int. J. Chem. Kinet.*, 46 (10), 619–639.

Herbinet, O. and Dayma, G., 2013. Jet-stirred reactors, *in: Cleaner combustion*, London: Springer, 183–210.

Hinze, J., 1994. *Turbulence*, New York: McGraw-Hill.

Hodzic, E., Esmaeelzade, G., Moshammer, K., Fernandes, R., Markus, D., Geron, M., Early, J., and Grosshans, H., 2018. Analysis of the turbulent flow structure in a jet stirred reactor using proper orthogonal decomposition, *in: Proceedings of the World Congress of the International Measurement Confederation, Belfast, United Kingdom*.

Hohenberg, G.F., 1979. Advanced approaches for heat transfer calculations, *SAE Transact.*, 88, 2788–2806.

Hu, Y., Zheng, X., Zhang, S., Ye, W., Wu, J., Poncin, S., and Li, H.Z., 2021. Investigation of hydrodynamics in high solid anaerobic digestion by particle image velocimetry and computational fluid dynamics: Role of mixing on flow field and dead zone reduction, *Bioresour. Technol.*, 319, 124130.

Hultqvist, A., Engdar, U., Johansson, B., and Klingmann, J., 2001. Reacting boundary layers in a homogeneous charge compression ignition (HCCI) engine, *SAE Transact.*, 1086–1098.

Hussein, H. and Martinuzzi, R., 1996. Energy balance for turbulent flow around a surface mounted cube placed in a channel, *Phys. Fluids*, 8 (3), 764–780.

Iavarone, S., Péquin, A., Chen, Z.X., Doan, N., Swaminathan, N., and Parente, A., 2021. An a priori assessment of the partially stirred reactor (PaSR) model for MILD combustion, *Proc. Combust. Inst.*, 38 (4), 5403–5414.

Innocenti, A., Andreini, A., Bertini, D., Facchini, B., and Motta, M., 2018. Turbulent flow-field effects in a hybrid CFD-CRN model for the prediction of NO_x and CO emissions in aero-engine combustors, *Fuel*, 215, 853–864.

Jawahar, H., Lin, Y., and Savill, M., 2018. Large eddy simulation of airfoil self-noise using OpenFOAM, *Aircr. Eng. Aerosp.*, 90 (1), 126–133.

Jaworski, Z. and Murasiewicz, H., 2010. LES and URANS modelling of turbulent liquid-liquid flow in a static mixer: Turbulent kinetic energy and turbulence dissipation rate, *Chem. Pap.*, 64 (2), 182–192.

Kenney, M., Sarjant, R., and Thring, M., 1956. The viscosity of mixtures of gases at high temperatures, *Br. J. Appl. Phys.*, 7 (9), 324.

Keulegan, G. and Beij, K., 1937. Pressure losses for fluid flow in curved pipes, *J. Res. Natl. Inst. Stan.*, 18, 89–144.

Klimenko, A.Y. and Bilger, R.W., 1999. Conditional moment closure for turbulent combustion, *Prog. Energy Combust. Sci.*, 25 (6), 595–687.

Kodavasal, J., McNenly, M.J., Babajimopoulos, A., Aceves, S.M., Assanis, D.N., Havstad, M.A., and Flowers, D.L., 2013. An accelerated multi-zone model for engine cycle simulation of homogeneous charge compression ignition combustion, *Int. J. Engine Res.*, 14 (5), 416–433.

Kolwzan, K. and Narewski, M., 2012. Alternative fuels for marine applications, *Latv. J. Chem*, 51 (4), 398.

Kraft, M., Maigaard, P., Mauss, F., Christensen, M., and Johansson, B., 2000. Investigation of combustion emissions in a homogeneous charge compression injection engine: Measurements and a new computational model, *Proc. Combust. Inst.*, 28 (1), 1195–1201.

Kresta, S. and Wood, P., 1993. The flow field produced by a pitched blade turbine: Characterization of the turbulence and estimation of the dissipation rate, *Chem. Eng. Sci.*, 48 (10), 1761–1774.

Krisman, A., Tang, J.C., Hawkes, E.R., Lignell, D.O., and Chen, J.H., 2014. A DNS evaluation of mixing models for transported PDF modelling of turbulent nonpremixed flames, *Combust. Flame*, 161 (8), 2085–2106.

Lammersen, T., Stoehr, K., Peters, N., and Abel, D., 2013. Model predictive control of dimethyl ether combustion in a jet stirred reactor under low temperature conditions, *in: American Control Conference, Washington DC, USA*, 1633–1638.

Leonard, A., 1974. Energy cascade in large-eddy simulations of turbulent fluid flows, *Adv. Geophys.*, 18, 237–248.

Lignola, P. and Reverchon, E., 1986. Dynamics of n-heptane and i-octane combustion processes in a jet stirred flow reactor operated under pressure, *Combust. Flame*, 64 (2), 177–183.

Lignola, P. and Reverchon, E., 1988. A jet stirred reactor for combustion studies: design and characterization, *Combust. Sci. Technol.*, 60 (4-6), 319–333.

Lu, T. and Law, C.K., 2006. Linear time reduction of large kinetic mechanisms with directed relation graph: n-Heptane and iso-octane, *Combust. Flame*, 144 (1-2), 24–36.

Maas, U. and Warnatz, J., 1988. Ignition processes in hydrogen-oxygen mixtures, *Combust. Flame*, 74 (1), 53–69.

Magnussen, B., 1981. On the structure of turbulence and a generalized eddy dissipation concept for chemical reaction in turbulent flow, *in: AIAA aerospace sciences meeting, St. Louis, USA*, 42.

Magnussen, B., 2005. The eddy dissipation concept: A bridge between science and technology, *in: Proceedings of the ECCOMAS thematic conference on computational combustion, Libson, Portugal*, 24.

Maigaard, P., Mauss, F., and Kraft, M., 2003. Homogeneous charge compression ignition engine: A simulation study on the effects of inhomogeneities, *J. Eng. Gas Turbines Power*, 125 (2), 466–471.

Makhija, A. and Giri, K., 2021. RANS based numerical simulations of turbulent diffusion flame using OpenFOAM®, *in: Proceedings of CHT-21 ICHMT International Symposium on Advances in Computational Heat Transfer, Rio de Janerio, Brail*.

Marchal, C., Delfau, J., Vovelle, C., Moréac, G., Mouna1, C., Mauss, F., *et al.*, 2009. Modelling of aromatics and soot formation from large fuel molecules, *Proc. Combust. Inst*, 32 (1), 753–759.

Mathieu, J. and Scott, J., 2000. *An Introduction to Turbulent Flow*, Cambridge: Cambridge University Press.

Matras, D. and Villermaux, J., 1973. A continuous reactor perfectly agitated by gaseous jets for the kinetic study of fast chemical reactions, *Chem. Eng. Sci.*, 28 (1), 129–137.

Mi, J., Nathan, G., and Nobes, D., 2001a. Mixing characteristics of axisymmetric free jets from a contoured nozzle, an orifice plate and a pipe, *J. Fluids Eng.*, 123 (4), 878–883.

Mi, J., Nobes, D.S., and Nathan, G.J., 2001b. Influence of jet exit conditions on the passive scalar field of an axisymmetric free jet, *J. Fluid Mech.*, 432, 91–125.

Mittal, G. and Sung, C., 2006. Aerodynamics inside a rapid compression machine, *Combust. Flame*, 145 (1-2), 160–180.

Moka, S., Pande, M., Rani, M., Gakhar, R., Sharma, M., Rani, J., Bhaskarwar, A., *et al.*, 2014. Alternative fuels: an overview of current trends and scope for future, *Renew. Sust. Energ. Rev.*, 32, 697–712.

Morar, D., 2014. *Subgrid-scale heat flux modeling for large eddy simulation of turbulent mixed convection*, Ph.D. thesis, Karlsruher Institut für Technologie, Germany.

Moshammer, K., Jasper, A., Popolan-Vaida, D., Lucassen, A., Diévart, P., Selim, H., Eskola, A., Taatjes, C., Leone, S., Sarathy, S., Ju, Y., Dagaut, P., Kohse-Hoeinghaus, K., and Hansen, N., 2015. Detection

and identification of the Keto-Hydroperoxide ($HOOCH_2OCHO$) and other intermediates during low-temperature oxidation of dimethyl ether, *J. Phys. Chem. A*, 119 (28), 7361–7374.

Moshammer, K., Jasper, A., Popolan-Vaida, D., Wang, Z., Bhavani S, V.S., Ruwe, L., Taatjes, C.A., Dagaut, P., and Hansen, N., 2016. Quantification of the Keto-Hydroperoxide ($HOOCH_2OCHO$) and other elusive intermediates during low-temperature oxidation of dimethyl ether, *J. Phys. Chem. A*, 120 (40), 7890–7901.

Mueller, M., Kim, T., Yetter, R., and Dryer, F., 1999. Flow reactor studies and kinetic modeling of the H_2/O_2 reaction, *Int. J. Chem. Kinet.*, 31 (2), 113–125.

Nenniger, J., Kridiotis, A., Chomiak, J., Longwell, J., and Sarofim, A., 1985. Characterization of a toroidal well stirred reactor, *in: Symposium (International) on Combustion, Michigan, USA*, vol. 20, 473–479.

Novosselov, I., Malte, P., Yuan, S., Srinivasan, R., and Lee, J., 2006. Chemical reactor network application to emissions prediction for industial DLE gas turbine, *in: ASME Turbo Expo: Power for Land, Sea, and Air, Barcelona, Spain*, 221–235.

OpenFOAM, 2013. http://www.openfoam.com.

Patel, H., Dhib, R., and Ein-Mozaffari, F., 2010. Computational fluid dynamics study of a styrene polymerization reactor, *Chem. Eng. Technol.*, 33 (2), 258–266.

Pauling, L., 1970. *General chemistry*, San Francisco: Freeman.

Peters, N., 2000. *Turbulent combustion*, Cambridge: Cambridge university press.

Pierce, C., 2001. *Progress-variable approach for large-eddy simulation of turbulent combustion*, Ph.D. thesis, Stanford university, USA.

Pitsch, H., 2000. Unsteady flamelet modeling of differential diffusion in turbulent jet diffusion flames, *Combust. Flame*, 123 (3), 358–374.

Pitsch, H., Chen, M., and Peters, N., 1998. Unsteady flamelet modeling of turbulent hydrogen/air diffusion flames, *Proc. Combust. Inst.*, 27, 1057–1064.

Poinsot, T. and Veynante, D., 2005. *Theoretical and numerical combustion*, Philadelphia, PA: RT Edwards, Inc.

Pope, S., 2000. *Turbulent Flows*, Cambridge: Cambridge University Press.

Pope, S.B., 1985. PDF methods for turbulent reactive flows, *Prog. Energy Combust. Sci.*, 11 (2), 119–192.

Ren, Z. and Pope, S.B., 2004. An investigation of the performance of turbulent mixing models, *Combust. Flame*, 136 (1-2), 208–216.

Revstedt, J., Fuchs, L., and Tragardh, C., 1998. Large eddy simulations of the turbulent flow in a stirred reactor, *Chem. Eng. Sci.*, 53 (24), 4041–4053.

Rezaeiravesh, S. and Liefvendahl, M., 2018. Effect of grid resolution on large eddy simulation of wall-bounded turbulence, *Phys. Fluids*, 30 (5).

Ribes, A. and Caremoli, C., 2007. Salome platform component model for numerical simulation, *in: Proceedings of the international computer software and applications conference, Beijing, China*, vol. 2, 553–564.

Richardson, L., 1911. IX. The approximate arithmetical solution by finite differences of physical problems involving differential equations, with an application to the stresses in a masonry dam, *Philos. Trans. Royal Soc.*, 307–357.

Roache, P., 1997. Quantification of uncertainty in computational fluid dynamics, *Annu. Rev. Fluid Mech.*, 29 (1), 123–160.

Roache, P.J., 1998. *Verification and Validation in Computational Science and Engineering*, Albuquerque: Hermosa Publishers.

Rota, R., Bonini, F., Servida, A., Morbidelli, M., and Carra, S., 1994. Validation and updating of detailed kinetic mechanisms: The case of ethane oxidation, *Ind. Eng. Chem. Res.*, 33 (11), 2540–2553.

Rotavera, B., Dievart, P., Togbe, C., Dagaut, P., and Petersen, E., 2011. Oxidation kinetics of *n*-nonane: Measurements and modeling of ignition delay times and product concentrations, *Proc. Combust. Inst.*, 33 (1), 175–183.

Rousso, A.C., Hansen, N., Jasper, A.W., and Ju, Y., 2018. Low-temperature oxidation of ethylene by ozone in a jet-stirred reactor, *J. Phys. Chem. A*, 122 (43), 8674–8685.

Sabel'nikov, V., Gorokhovski, M., and Baricault, N., 2006. The extended IEM mixing model in the framework of the composition PDF approach: Applications to diesel spray combustion, *Combust. Theory Model.*, 10 (1), 155–169.

Satheesh Kumar, A., Singh, A., and Thiagarajan, K.B., 2020. Simulation of backward facing step flow using OpenFOAM®, AIP Conf., vol. 2204, 030002.

Sbrizzai, F., Lavezzo, V., Verzicco, R., Campolo, M., and Soldati, A., 2006. Direct numerical simulation of turbulent particle dispersion in an unbaffled stirred-tank reactor, *Chem. Eng. Sci.*, 61 (9), 2843–2851.

Sheng, J., Meng, H., and Fox, R., 2000. A large eddy PIV method for turbulence dissipation rate estimation, *Chem. Eng. Sci.*, 55 (20), 4423–4434.

Smagorinsky, J., 1963. General circulation experiments with the primitive equations: I. the basic equations, *Mon. Weather Rev.*, 91 (3), 99–164.

Stoehr, K.D., Peters, N., and Beeckmann, J., 2015. Low temperature oscillations of DME combustion in a jet-stirred reactor, *Proc. Combust. Inst.*, 35 (3), 3601–3607.

Stull, D.R. and Prophet, H., 1971. *JANAF Thermochemical Tables*, Waschington DC: U.S. Department of Commerce.

Sturgess, G. and Shouse, D., 1996. A hybrid model for calculating lean blowouts in practical combustors, *in: Proceedings of the Joint Propulsion Conference and Exhibit, Buena Vista, FL, USA*, 3125.

Subramaniam, S. and Pope, S.B., 1998. A mixing model for turbulent reactive flows based on euclidean minimum spanning trees, *Combust. Flame*, 115 (4), 487–514.

Sutherland, W., 1893. The viscosity of gases and molecular force, *Lond. Edinb. Dublin philos. mag. j. sci.*, 36 (223), 507–531.

Tang, R., Xu, Q., Pan, J., Gao, J., Wang, Z., Wei, H., and Shu, G., 2022. An experimental and modeling study of ammonia oxidation in a jet stirred reactor, *Combust. Flame*, 240, 112007.

Tranter, R.S., Brezinsky, K., and Fulle, D., 2001. Design of a high-pressure single pulse shock tube for chemical kinetic investigations, *Rev. Sci. Instrum.*, 72 (7), 3046–3054.

Van Balen, W., Uijttewaal, W., and Blanckaert, K., 2010. Large-eddy simulation of a curved open-channel flow over topography, *Phys. Fluids*, 22 (7), 075108.

Venier, C., Pairetti, C., Damian, S., and Nigro, N., 2017. On the stability analysis of the PISO algorithm on collocated grids, *Comput. Fluids*, 147, 25–40.

Vermeersch, M., Held, T., Stein, Y., and Dryer, F., 1991. Autoignition chemistry studies of n-butane in a variable pressure flow reactor, *SAE Transact.*, 645–661.

Verzicco, R., Fatica, M., Iaccarino, G., and Orlandi, P., 2004. Flow in an impeller-stirred tank using an immersed-boundary method, *AIChE journal*, 50 (6), 1109–1118.

Viskanta, R., 1993. Heat transfer to impinging isothermal gas and flame jets, *Exp. Therm. Fluid Sci.*, 6 (2), 111–134.

Wada, T., Mellado, J., and Peters, N., 2009. Linear stability analysis of one-step model with diluted lean CH_4/air oscillations at low temperatures, *in: Conference on Energy for a Clean Environment, Losbon, Portugal*.

Wagnon, S.W., Thion, S., Nilsson, E.J., Mehl, M., Serinyel, Z., Zhang, K., Dagaut, P., Konnov, A.A., Dayma, G., and Pitz, W.J., 2018. Experimental and modeling studies of a biofuel surrogate compound: Laminar burning velocities and jet-stirred reactor measurements of anisole, *Combust. Flame*, 189, 325–336.

Wang, G., Yang, F., Wu, J., Ma, Y., Peng, C., Liu, T., and Wang, L., 2021. Estimation of the dissipation rate of turbulent kinetic energy: A review, *Chem. Eng. Sci.*, 229, 116133.

Warnatz, J., Maas, U., and Dibble, R., 2006. *Combustion*, Berlin: Springer.

Weller, H., Tabor, G., Jasak, H., and Fureby, C., 1998. A tensorial approach to computational continuum mechanics using object-oriented techniques, *Comput. Phys.*, 12 (6), 620–631.

Werler, M., Schießl, R., and Maas, U., 2017. A rapid compression expansion machine (RCEM) for measuring species histories, *in: Proceedings of the International Colloquium on the Dynamics of Explosions and Reactive Systems, Boston, USA*.

White, F.M., 1990. *Fluid Mechanics*, New York: McGraw-Hill.

Wilcox, D., 1998. *Turbulence Modeling for CFD*, vol. 2, California: DCW industries La Canada.

Wilk, R., Cernansky, N., Pitz, W., and Westbrook, C., 1989. Propene oxidation at low and intermediate temperatures: A detailed chemical kinetic study, *Combust. Flame*, 77 (2), 145–170.

Wolf, D. and Resnick, W., 1963. Residence time distribution in real systems, *Ind. Eng. Chem. Fundamen.*, 2, 287–293.

Woschni, G., 1967. A universally applicable equation for the instantaneous heat transfer coefficient in the internal combustion engine, 3065–3083.

Zhang, H., Zhao, M., and Huang, Z., 2020. Large eddy simulation of turbulent supersonic hydrogen flames with OpenFOAM, *Fuel*, 282, 118812.

Zhang, T., Zhao, H., and Ju, Y., 2018. Numerical studies of novel inwardly off-center shearing jet-stirred reactor, *AIAA journal*, 56 (9), 3388–3392.

Zhao, M., Chen, Z., Zhang, H., and Swaminathan, N., 2021. Large eddy simulation of a supersonic lifted hydrogen flame with perfectly stirred reactor model, *Combust. Flame*, 230, 111441.

Zuckerman, N. and Lior, N., 2006. Jet impingement heat transfer: Physics, correlations, and numerical modeling, *Adv. Heat Transf.*, 39, 565–631.

LIST OF PUBLICATIONS

Reviewed journal papers

- Esmaeelzade, G., Moshammer, K., Markus, D., Maas, U., and Grosshans, H., 2021. Parametrical investigation for the optimization of spherical jet-stirred reactors design using large eddy simulations, *SN Appl. Sci.*, 3 (9), 1-15.
- Esmaeelzade, G., Moshammer, K., Fernandes, R., Markus, D., and Grosshans, H., 2019. Numerical study of the mixing inside a jet stirred reactor using large eddy simulations, *Flow Turbul. Combust.*, 102 (2), 331-343.

Conference presentations

- Esmaeelzade, G., Moshammer, K., Markus, D., Maas, U., and Grosshans, H., 2018. Parametric study of the turbulent flow inside a spherical jet stirred reactor , *71^{st} Annual American Physical Society (APS), Annual Meeting of the Division of Fluid Dynamics (DFD Meeting), Atlanta, USA*.
- Esmaeelzade, G., Moshammer, K., Fernandes, R., Markus, D., Maas U., and Grosshans, H., 2018. Optimization of new fuel characterization in a jet stirred reactor, *Kraftstoffe für die Mobilität von morgen, Braunschweig, Germany*.
- Hodzic, E., Esmaeelzade, G., Moshammer, K., Fernandes, R., Markus, D., Geron, M., Early, J., and Grosshans, H., 2018. Analysis of the turbulent flow structure in a jet stirred reactor using proper orthogonal decomposition, *XXII World Congress of the International Measurement Confederation (IMEKO), Belfast, UK.*
- Esmaeelzade, G., Moshammer, K., Fernandes, R., Markus, D., and Grosshans, H., 2017. Numerical study of the mixing inside a jet stirred reactor using large eddy simulations, *The 6^{th} International Conference on Jets, Wakes and Separated Flows (ICJWSF), Cincinnati, USA*.
- Esmaeelzade, G., Moshammer, K., Fernandes, R., Markus, D., and Grosshans, H., 2017. Numerical simulations of jet stirred reactors, *28^{te} Deutscher Flammentag, Darmstadt, Germany*.